NOAA Technical Memorandum ERL PMEL-63

UNPOLARIZED IRRADIANCE REFLECTANCES AND GLITTER PATTERNS OF RANDOM CAPILLARY WAVES ON LAKES AND SEAS, BY MONTE CARLO SIMULATION

Rudolph W. Preisendorfer
Curtis D. Mobley

Pacific Marine Environmental Laboratory
Seattle, Washington
September 1985

UNITED STATES
DEPARTMENT OF COMMERCE

Malcolm Baldrige,
Secretary

NATIONAL OCEANIC AND
ATMOSPHERIC ADMINISTRATION

Environmental Research
Laboratories

Vernon E. Derr,
Director

NOTICE

Mention of a commercial company or product does not constitute an endorsement by NOAA/ERL. Use of information from this publication concerning proprietary products or the tests of such products for publicity or advertising purposes is not authorized.

CONTENTS

UNPOLARIZED IRRADIANCE REFLECTANCES AND GLITTER PATTERNS OF RANDOM CAPILLARY WAVES ON LAKES AND SEAS, BY MONTE CARLO SIMULATION

Rudolph W. Preisendorfer
Curtis D. Mobley

Pacific Marine Environmental Laboratory, NOAA
7600 Sand Point Way N.E., Seattle, WA 98115

ABSTRACT. The downward irradiance reflectance r_- and the upward irradiance reflectance r_+ of a random air-water surface, formed by capillary waves, are computed as a function of lighting conditions and wind speed by Monte Carlo means for incident unpolarized radiant flux. The possibility of multiple scattering of light rays and of ray-shielding of waves by other waves is included in the calculations. The effects on r_+ of multiple scattering and wave shielding are found to be important for higher wind speeds ($\geq$10 m/s) and near horizontal light ray angles ($\geq$70°) of incidence. A simple analytic first-order model of irradiance reflectance, which assumes a binormal distribution of water facet slopes, is tested against the relatively exact Monte Carlo results. Regions are defined in wind-speed and incident-angle space over which the first-order model is acceptable. Plots of the Monte Carlo r_+ are drawn as functions of wind speed and angle of incidence of light rays. r_+ are also found for various continuous radiance distributions simulating overcast skies and upwelling submarine light fields just below the air-water surface. Simulated glitter patterns are displayed as functions of wind speed and angle of incidence of light rays for both reflected and transmitted rays, and for light sources located both above and below the air-water surface. Extensions of the present Monte Carlo procedure to include gravity waves as well as capillary waves are outlined.

1. *Introduction*

In this study we develop a Monte Carlo procedure for estimating the unpolarized irradiance reflectances and glitter patterns of a wind-roughened sea surface as a function of environmental lighting conditions and wind speed, given the statistical properties of the surface. The procedure includes the effects of multiple scattering of light rays and their shielding by wave facets. Since the optical properties of the sea surface are determined primarily by capillary waves, even in the presence of gravity waves, our attention is directed mainly at the proper treatment of the capillary wave

case. However, for completeness and possible future use, a model also is developed which allows an exact calculation of the optical properties of a wind-roughened surface which has the form of a spatially stationary process over the full capillary-gravity range of water waves.

A. Some Initial Observations

To introduce the ideas below, we make the following observations.

(i) The air-water surface as a wind-driven radiometric valve

The amount of sunlight and skylight penetrating the surface of the sea generally increases as the surface becomes increasingly crinkled by gusts of wind. Moreover, this wind-induced increase of transmission is greater for rays of light coming in from near the horizon than for those arriving from near the zenith. These facts are made plausible by inspecting a plot of the Fresnel reflectance curve of a flat air-water surface as a function of the incidence angle for unpolarized light in the visible portion of the spectrum. For a narrow beam of unpolarized light, incident from the zenith on a flat air-water surface, nearly 98 percent of the beam's radiant flux penetrates into the sea below, whereas the beam incident at 80 degrees from the zenith has only about 65 percent of its flux transmitted into the depths below. As a fresh breeze plays over the flat surface and crinkles it with capillary waves, the rays from the zenith now encounter tipped wave facets which transmit a slightly smaller amount of light; however, these same water facets tipped toward the near-horizontal incident rays allow a relatively greater light transmission. The net effect as we shall see below, according to Fresnel's law and the statistical form of the surface, is a greater overall transmission of radiant flux from sun and sky into the ruffled sea, relative to the flat, calm surface.

The surface of the sea thus acts as a wind-driven radiometric valve which allows greater or lesser amounts of radiant energy from the sky to penetrate the sea's upper layers, in accordance with wind speed and lighting conditions over the surface. The net effect of increased light transmission from the sky and sun is to warm the near-surface water, to drive photosynthesis, and eventually to help power the basic elements of both the climate and life of planet Earth (cf., e.g., Duntley, 1963).

(ii) Reflectances as initial conditions in hydrologic optics

A mathematical means by which the photosynthetic and climatic matters in (i) can be explored is the set of solutions of the irradiance differential equations for light in lakes and seas. As shown in Preisendorfer and Mobley (1984), for example, the light field in an optically deep hydrosol, such as a sea, is determinable once the downward reflectance r_- and upward reflectance r_+ of the random sea surface are known along with the depth dependence of the sea's optical properties. In this work we show how to obtain $r_\pm$ for a randomly capillaried sea or lake surface with given wind speed and lighting conditions over it. The quantities $r_\pm$ may then serve as initial conditions in the solution of the irradiance equations by properly accounting for the optical properties of the wind-roughened air-water surface. From the depth-variation of the irradiance field, for example, the potential heating of the upper water layers may be determined using the wavelength-dependent volume absorption function in those layers.

(iii) A first-order analytic ray tracing theory

The problem of estimating the reflectance and transmittance of a wind-roughened sea surface using analytic methods is relatively simple when the wind speed is small so that the air-water surface is only mildly rippled. As we shall see below, a simple first-order (single-scatter) unpolarized ray tracing theory adequately describes the glitter pattern and hence reflectance properties of the sea surface for sufficiently low wind speeds and for light rays incident on the surface from sufficiently near the zenith (e.g. for winds of less than 5 m/s when the angle of incidence is within 60° of the zenith).

(iv) Effects of multiple scattering and shielding of rays

When the wind speeds become too great or when rays of light are incident on the water from nearly horizontal directions, the first-order ray-tracing theory is no longer statistically acceptable because the rays are more likely to undergo multiple scattering among the wave facets. There is also a shielding effect of one wave facet blocking rays from another, which the first-order theory does not handle. We find that the effect of multiple scattering of light rays is to slightly decrease the net penetration of sunlight and skylight into the sea, since there are repeated opportunities for the sea surface to reflect the (usually near grazing) radiant flux of a multiply-reflected incident ray back into the sky above. On the other hand, the shielding action of a facet tends on average to increase the amount of light penetrating the surface because the intercepting facets on average tilt their normals toward the line of approach of the incoming ray.

The net effect of multiple scattering and shielding (relative to single-scattering estimates) is small and amounts, e.g., to about a 2 or 3 percent increase in the sea surface radiance reflectance for wind speeds around 10 m/s

and individual angles of ray incidence around 80 degrees from the zenith; for these conditions the reflectance is of order 0.2. The practical effect of this on solar irradiance estimates is relatively small. For example, the solar irradiance over the visible spectrum (400-700 nanometers) at sea level in moist air for the sun near the horizon at 80° from the zenith on an otherwise clear day amounts to about 75 watt/m^2. Of this, about 0.2 × 75 or 1.5 watt/m^2 are reflected. Hence inclusion of multiply-scattered radiant flux in the sun and sky reflected flux estimates will in this example increase the estimates (relative to single-scatter estimates) at most on the order of 0.05 watt/m^2 at each point of the sea over its sunlit expanse at low sun altitudes (as in the polar regions of the earth). This increase is small relative to our estimates of the decrease of downward reflectance of the sea when the wind speed ranges from 0 to 20 m/s. Over this wind speed range the average surface reflectance for sun rays incident at 80 degrees from the zenith drops from about 0.35 at 0 m/s to 0.17 at 20 m/s, i.e., by about a factor of 2.

(v) Alongwind and crosswind effects on transmittance

There is another small but calculable effect on the transfer of light downward past the wind-blown sea surface that on average is also on the order of magnitude of the multiple-scatter and shielding effects. Experiments show (Preisendorfer, 1976, vol. VI, pp. 145-151) that the normals to the capillary wave facets in the alongwind vertical plane tend on average to be tipped away from the vertical at greater angles than those in the crosswind vertical plane. Hence light rays incident, at a fixed zenith angle, on the rippled sea surface in the alongwind plane on average undergo a greater transmission into the sea compared to those incident in the crosswind plane. The difference in

r_{-} for these two modes of incidence is on the order of 5 percent for wind speeds around 10 m/s and angles of incidence around 80 degrees from the zenith.

B. Historical Notes

An early important investigation of the optical properties of the sea surface is reported in Hulburt (1934). The modern experimental study of optical effects of water waves begins in the work of Duntley (1950) where direct *in situ* electronic measurements of the capillary water-wave slopes were made using two pairs of parallel, vertical, immersed wires. One pair formed a plane in the alongwind direction and the other a plane in the crosswind direction. (See Preisendorfer, 1976, vol. VI, p. 138. Henceforth, bibliographic references to this work in the present article will be abbreviated as, e.g., "*H.O.* vol. VI, p. 138".) Initial analytical consequences of Duntley's research for radiative transfer across a random air-water surface are drawn in Duntley and Preisendorfer (1952). In particular, it was found that the wave slopes ζ_u and ζ_c in the alongwind and crosswind directions are normally distributed, independent variates. The wave-slope wind-speed laws deduced from these studies, showing variance of the alongwind and crosswind wave slopes proportional to wind speed--a main building block in the present article--are recorded in Duntley (1954). An alternate optical approach to water-surface geometry may be found in Schooley (1954). About this time the researches of Cox and Munk (1954a,b; 1955) were completed in which the inverse problem was solved: from photographs of remotely observed sun glitter patterns, deduce the statistical properties of the sea surface. To effect this solution, Cox and Munk used an ingenious geometric analysis of the glitter pattern photographs, completing a project which, in Hulburt's

(1934) view, was regarded as a difficult task (cf. *H.O.* vol. VI, p. 138). The main result again showed that (ζ_u,ζ_c) is a pair of independent, normally distributed variables whose variances increase linearly with wind speed.

In an important sense the experimental works of Duntley and of Cox and Munk are dual and complementary: Duntley in effect placed his wave slope meter at a fixed point in the sea and made long-time observations of the alongwind and crosswind wave slopes there; the Cox and Munk aerial photographs were made at a fixed instant in time and cover a wide spatial expanse of sea. When comparing the wave-slope wind-speed laws deduced by Cox and Munk (1954a) and by Duntley (1954), we see that ergodic equivalence reasonably holds for these dual forms of sea surface statistics (cf. *H.O.* vol. VI, pp. 148-151). That is, for the conditions of their experiments, time-averaged wave slope statistics at a point and space-averaged wave slope statistics at an instant are sensibly equal. This provides the basis for the stationary random surface approaches to the sea surface reflectance problem followed in the present study.

Another important empirical law needed for a thorough study of the reflectance problem of wind-roughened seas was implicitly found by Neumann (1952) at about the same time Duntley, and Cox and Munk were doing their experiments. This is the wave-elevation wind-speed law showing the variance of gravity-wave elevation as being proportional to the fifth power of wind speed. Neumann's work was generally concurrent with and inspired by the researches of Pierson (1955) and Pierson and Marks (1952), who contributed to our modern representations of the random sea surface by using novel stochastic integration techniques. For a derivation of the Neumann spectrum, the wave-elevation wind-speed law, and the relation of the Neumann spectrum to subsequent water wave spectra, see *H.O.* vol. VI, pp. 181-194. In Appendixes

A, B, C below we use the Neumann spectrum and its modern generalization to lay the groundwork for an exact Monte Carlo procedure to determine the reflectance and transmittance of a statistically stationary random wind-aroused sea surface consisting of superpositions of wave trains ranging from capillary ripples to long gravity swells.

A recent Monte Carlo study of sun glitter patterns, and references to earlier glitter studies by the same authors and their colleagues, may be found in Guinn *et al.* (1979). The capillary slope statistics of Duntley and of Cox and Munk are used in these calculations. We shall build on this important series of studies by looking specifically at the glitter and reflectance problem using a capillary-wave model that incorporates multiple scattering of light rays and the shielding of wave facets, as discussed in paragraph A above. We note in passing that some analytical attempts at solving the reflectance problem for wind-roughened seas have been made (cf. *H.O.* vol. VI, footnote 8, p. xii; *H.O.* vol. VI, secs. 12.10-12.14; and Preisendorfer, 1971).

C. Overview of Study

The present computations leading to the desired optical properties of the wind-roughened sea surface fall into four main stages:

(i) construction of a realization of the random air-water surface,

(ii) tracing incident parent light rays over, under and through the realized surface toward their ultimate destinations,

(iii) assigning radiant flux content to each processed daughter ray, and

(iv) stacking daughter rays (that proliferate owing to multiple scattering of the parent ray) to await further processing, as in (ii) and (iii).

The final step in the procedure is to accumulate the assigned ray fluxes of the daughter rays to obtain the associated reflectance and transmittance properties of the random surface itself.

Figure 1 shows a perspective view of part of the water surface and a multiply scattered ray. A finite region of the mean water surface is resolved by a hexagonal grid of triangles. At each triangle vertex the sea surface elevation is defined, so that the waves are represented by a set of triangular facets. These facets are contained in the hexagonal domain (the cylindrical region of space) defined by the hexagonal grid. Four such facets are shown in Fig. 1. After a particular surface realization has been generated in stage (i), a light ray of unit radiant flux is aimed toward the surface from any chosen direction. Figure 1 shows such a ray entering the hexagonal domain at point A. Every such initial ray eventually strikes a surface wave facet, as at B. In general, each encounter of a ray with a wave facet generates both a reflected and a refracted daughter ray. The directions and radiant flux contents of these daughter rays are determined by Snell's law and Fresnel's formula, respectively. The daughter rays may undergo further encounters with other wave facets. As illustrated in Fig. 1, the first refracted ray at B, heading downward through the water, leaves the hexagonal domain at D without further scattering. The first reflected ray at B, however, intercepts another facet at C, generating two more rays. The reflected ray starting from C leaves the domain at E. The refracted ray starting from C encounters yet another facet at F and undergoes a total internal reflection before leaving the domain at G. Thus the initial ray finally results in one reflected and two refracted rays emerging from the hexagonal domain. The fluxes at the points of emergence contribute to the appropriate reflectance and transmittance calculations.

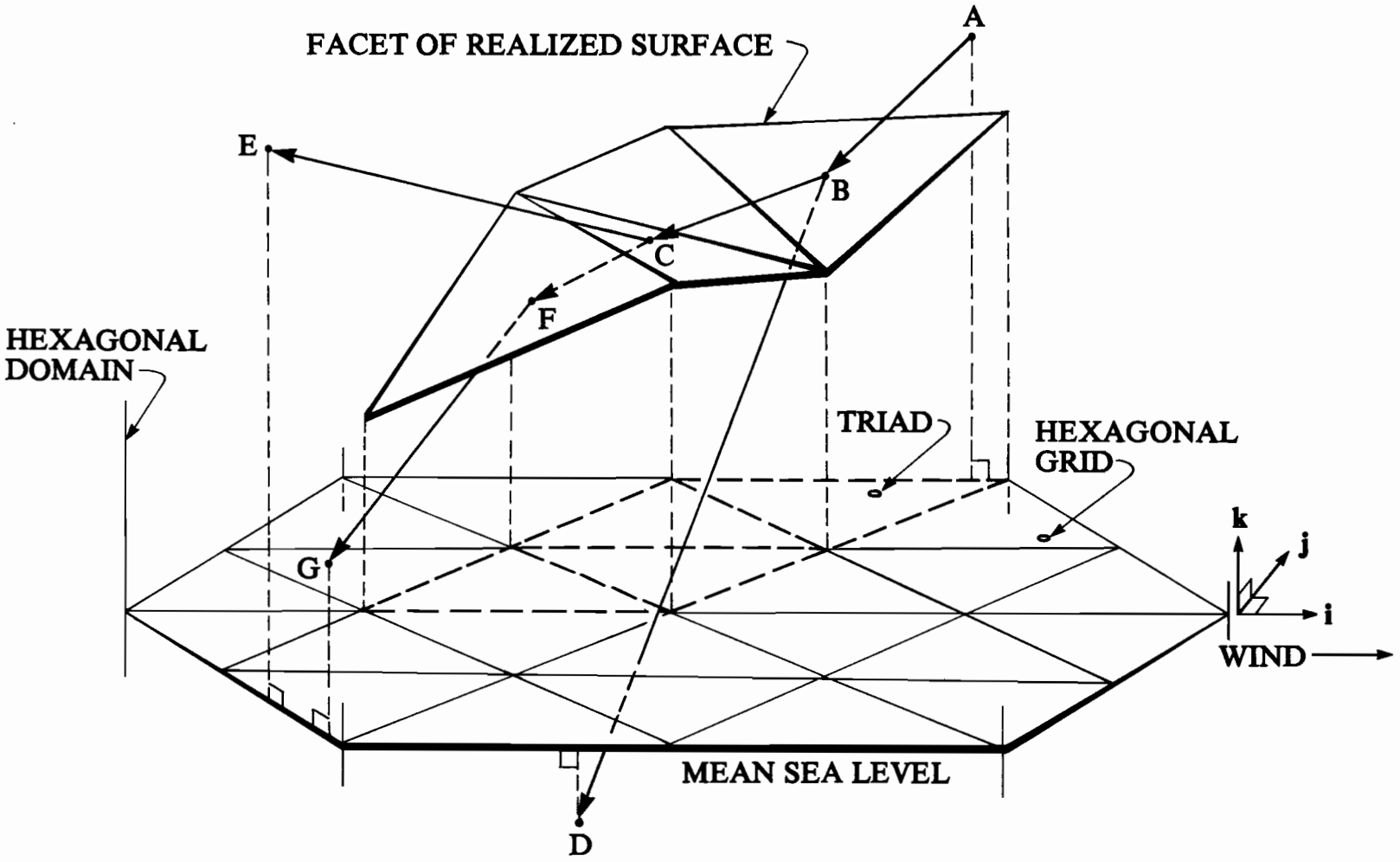

Figure 1.--Illustration of the hexagonal domain with a particular surface realization and ray tracing. Observe the orientation of the horizontal triangular facets (triads) relative to the downwind direction. Details of a triad are shown in Fig. 3.

Figure 2 gives an overview of the computational process in the form of a flow diagram of eleven steps. In step 1 of the diagram the computer run is initialized by choosing the wind speed and direction, size of the hexagonal grid, lighting conditions, and the like. In step 2 a realization of the random surface is constructed over the hexagonal grid. In step 3 an initial ray incident along the desired direction $\underset{\sim}{\xi}'$ is specified. This *parent ray* may approach the surface from the air side, as in Fig. 1, or from the water side. The parent ray $\underset{\sim}{\xi}'$ is assigned a radiant flux $P' = 1$, and the point $\underset{\sim}{p}'$ where the ray enters the hexagonal domain (e.g. point A of Fig. 1) is determined. The information $(\underset{\sim}{\xi}', \underset{\sim}{p}', P')$, which fully determines a ray, is then stored in an array S, called the *stack*. (S in practice has dimensions of 10×7. The 7-dimension part of S holds the components of the vectors $\underset{\sim}{\xi}'$ and $\underset{\sim}{p}'$, and the scalar P'. The 10-dimension part of S allows for up to ten rays to be queued at any one time. Never in our experience with the model were as many as ten rays in the stack simultaneously.) In step 4 we pull the next available ray triple $(\underset{\sim}{\xi}, \underset{\sim}{p}, P)$ from the stack and trace the ray to completion in step 5. That is, in step 5, we prolong the ray from $\underset{\sim}{p}$ along direction $\underset{\sim}{\xi}$ until either the surface is encountered or the ray leaves the hexagonal domain. If, in executing step 5, the surface is encountered, the point $\underset{\sim}{p}_i$ of interception of the ray and the surface is determined (e.g. point B in Fig. 1) and *daughter rays* (e.g., BC, BD in Fig. 1) are produced. In step 6, one daughter ray is always generated (at $\underset{\sim}{p}_i$) along the reflected direction, $\underset{\sim}{\xi}_r$. In step 7, one daughter ray will be generated along $\underset{\sim}{\xi}_t$ if and only if the ray is not totally internally reflected at $\underset{\sim}{p}_i$. (For example, at point F in Fig. 1, total internal reflection takes place and there is no transmitted daughter ray.) In either of steps 6 or 7, the direction $\underset{\sim}{\xi}$ of the parent ray (which of course may be a daughter ray from a previous ray-surface

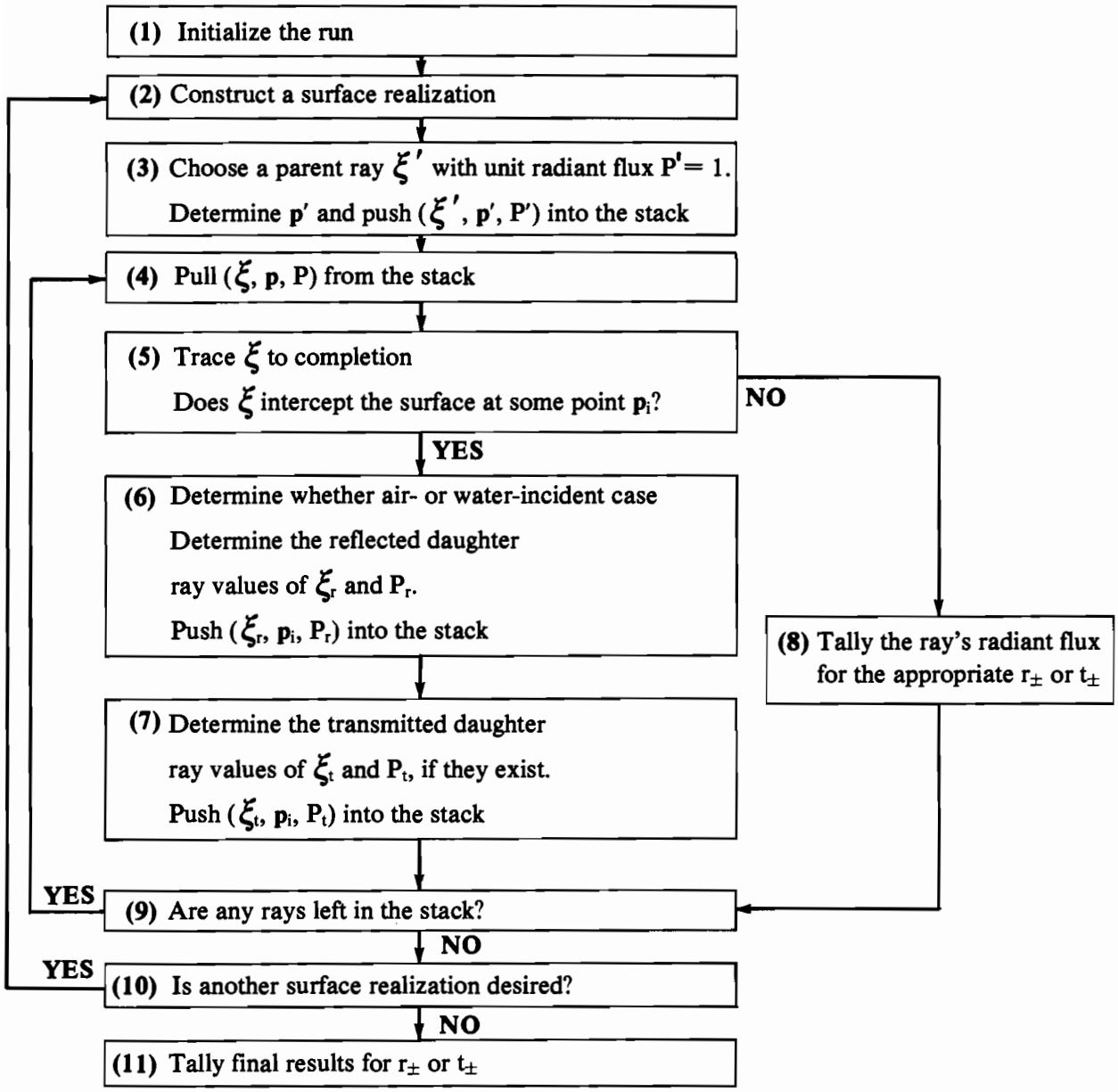

Figure 2.--Ray tracing flow diagram.

interception), the normal $\underset{\sim}{n}$ to the intercepted wave facet, and the daughter ray direction $\underset{\sim}{\xi}_r$ determine an associated Fresnel factor for reflectance. This factor is multiplied into the current radiant flux P of the parent ray to obtain the flux content P_r of the reflected daughter ray. The flux content of the transmitted ray is then $P_t = P - P_r$. The daughter ray triples are pushed into the stack for further processing. On the other hand, step 5 may fail to produce a point of interception $\underset{\sim}{p}_i$ (as at D, G, E of Fig. 1) in which case the ray has finished its interactions with the surface in the hexagonal domain and its radiant flux content is added (in step 8) to an accumulating sum for r_+ or r_- as the case may be.

In practice an initial parent ray may go on to encounter the air-water surface a large number (~10) of times so that, at some stage in the running calculation, several of its daughter ray triples may be simultaneously in the stack awaiting further processing of the kind in step 5 (during which they in turn can generate more daughter ray triples). The pushing activity of steps 3, 6 and 7 places each ray triple in the stack as soon as the ray is generated. The stack is systematically serviced by the pulling activity of step 4 via step 9. The stack is crucial to the ray tracing algorithm, since it allows the "tree" of multiply scattered rays to grow without restrictions on the number of ray-surface interactions or upon the order in which daughter rays are traced to completion. When the stack of waiting ray triples is depleted, we check in step 10 to see if another surface realization is needed. If so, we return to step 2 of the ray tracing flow diagram and begin anew; otherwise the final results are computed in step 11.

In the work below we routinely use 2000 or more surface realizations for each fixed initial incident direction $\underset{\sim}{\xi}'$. If the initial parent ray is air-incident, then the calculation results in the downward reflectance r_-. If the

initial parent ray is water-incident, we obtain r_+. In this way, using ample numbers of realized surfaces, we can build up the statistics r_+ and r_- with controllably small variances about their "true" values. Transmittances $t_\pm$ are obtained from the final $r_\pm$ values via $t_\pm = 1 - r_\pm$.

The next four sections give the details of the calculations outlined above. Section 2 discusses the hexagonal grid and the construction of the surface realizations. Sections 3 and 4 present the ray-tracing and reflectance calculations, respectively. The stack is briefly discussed in section 5, and section 6 discusses the characteristics of the computer code. The first major results of the model are shown in section 7, which presents model-generated glitter patterns for both reflected and transmitted rays starting from both above and below the water surface. Glitter patterns of reflected rays are compared with a first-order theory of glitter patterns. Computed irradiance reflectances, the main results of this study, are graphically summarized in section 8. A variety of point and continuous lighting conditions for both sky and submarine light sources is studied. Finally, section 9 presents an algorithm for extending the present capillary-wave model to stationary random air-water surfaces with known wind-induced power spectra.

Acknowledgments. Support of the work by one of us (C.D.M.) was provided in part by Equatorial Pacific Ocean Climate Study Council and the National Climate Program Office. Ryan Whitney provided word processing and editorial assistance. Joy Register and Gini Curl helped prepare the diagrams.

2. *Constructing Capillary Wave Surfaces*

A. Wave-slope wind-speed Laws

As noted in the introduction, the statistics of the capillary wave structure of the sea surface reside in the wave-slope wind-speed laws. We will use these statistics to construct realizations of the capillary wave surfaces. Let σ_u^2 and σ_c^2 respectively be the (dimensionless) upwind and crosswind variances of the independent, normally distributed capillary wave slopes ζ_u and ζ_c at a point. Then (*H.O.* vol. VI, p. 145) the general forms linking these variances and the wind speed U are

$$\sigma_u^2 = a_u U^p \quad \text{and} \quad \sigma_c^2 = a_c U^p \,. \tag{2.1}$$

For the case p = 1,

$$a_u = 3.16 \times 10^{-3} \text{ s/m} \quad \text{and} \quad a_c = 1.92 \times 10^{-3} \text{ s/m}, \tag{2.1}'$$

where U is in m/s as measured at an anemometer height of 12.5 m above mean sea level. In practice, for (2.1) we have p = 1; but we momentarily retain the general exponent p and general a_c, a_u to establish the required scaling rules (cf. (2.12)) for the sea surface coordinate grid.

Let σ_ζ^2 (in m^2) be the variance of the normally distributed capillary wave elevation ζ at a point. The wave-elevation wind-speed law for capillary waves is assumed to be generally of the form

$$\sigma_\zeta^2 = a_\zeta U^q \,, \tag{2.2}$$

where a_ζ is a constant and the exponent q of wind speed U is left unspecified for the moment. For gravity waves, the Neumann spectrum gives q = 5 and $a_\zeta = 3.2 \times 10^{-6}\ s^5\ m^{-3}$ (cf. *H.O.* vol. VI, p. 188). For capillary waves, a_ζ and q are unknown. It turns out, however, that the present random capillary wave surfaces can be modeled without having to know a_ζ and q explicitly, as will be demonstrated below.

B. Hexagonal Grid

To construct a realization of a random capillary surface, first set up a wind-oriented *hexagonal grid* system in the horizontal plane of the mean water surface, as sketched in Fig. 1. Thus a finite hexagonal region of the laterally infinite horizontal mean sea surface is partitioned into a set of triangles or *triads*. At each vertex (or *node*) of each triad we erect a directed vertical line segment either upward or downward. The three endpoints of these segments define in space a plane *facet* of the water surface. Four such facets are shown in Fig. 1. The *hexagonal domain* is the enclosed cylindrical region of space above and below the hexagonal grid. This region is formed by a vertical line tracing the perimeter of the hexagonal grid, so that the boundary of this domain is the set of all vertical lines through the perimeter of the hexagon. A wind-oriented cartesian coordinate system is chosen with $\underset{\sim}{i}$ downwind, $\underset{\sim}{k}$ perpendicular to the mean sea level and positive upward, and $\underset{\sim}{j} = \underset{\sim}{k} \times \underset{\sim}{i}$ in the crosswind direction. A detail of a triad is shown in Fig. 3. The base, or alongwind dimension, of the triad is δ (always parallel to the wind) and the crosswind dimension is ε. The units of δ and ε are in meters. A particular set of realized facets over the hexagonal grid constitutes a *realization* of a random surface. The set of all realized

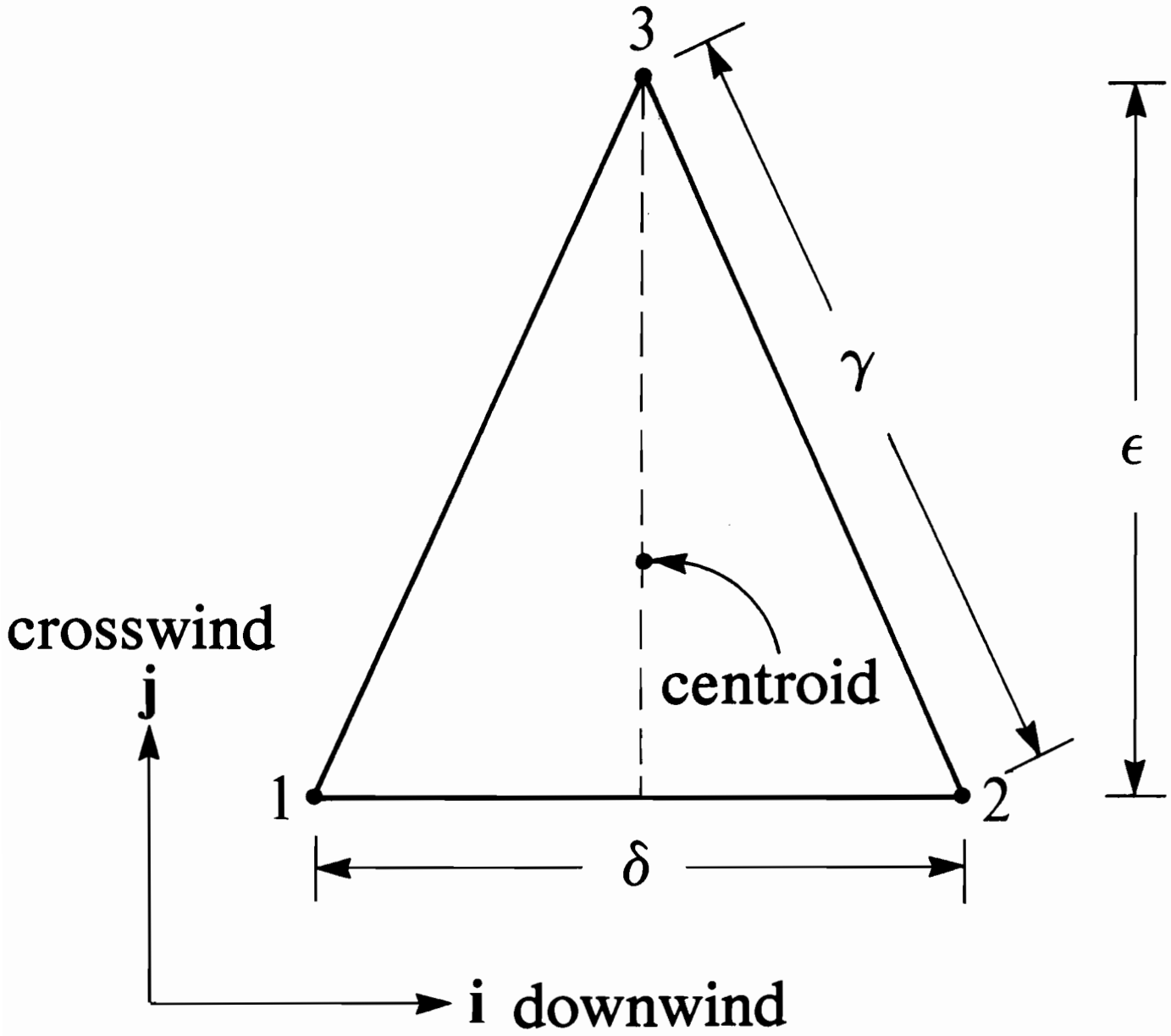

Figure 3.--A typical triad. Its placement in the hexagonal grid is shown in Figs. 1 and 5.

surfaces (on the order of 2000 per experiment in this study) constitutes a *random surface*.

C. Realized Surface

Experiment and theory indicate that the capillary wave elevations are normally distributed about the mean water surface (*H.O.* vol. VI, pp. 194-197). To construct random wave facets above or below points 1, 2, 3 in Fig. 3 we repeatedly make three independent draws from $N(0,\sigma^2)$, the normal population with zero mean and variance σ^2 (in meters^2), resulting in an ensemble of triples of elevations z_1, z_2, z_3, (in meters) respectively. The *upwind* and *crosswind* slopes ζ_u and ζ_c of the random facet are then the normally distributed random variables given by

$$\zeta_u = (z_2 - z_1)/\delta \tag{2.3}$$
$$\zeta_c = (z_3 - \tfrac{1}{2}(z_1 + z_2))/\varepsilon \ .$$

If "E" denotes the ensemble average over the ensembles of z_1, z_2, z_3 values, then clearly

$$E\{z_j\} = 0 \quad , \quad j = 1,2,3 \ ; \text{ and so } \quad E\{\zeta_u\} = E\{\zeta_c\} = 0 \ . \tag{2.4}$$

Moreover, one readily verifies from (2.3) that the variances of ζ_u and ζ_c (i.e., the σ_u^2 and σ_c^2 of (2.1)) are given, in terms of triad geometry, by

$$\sigma_u^2 \equiv E\{\zeta_u^2\} = 2\sigma^2/\delta^2 \tag{2.5}$$
$$\sigma_c^2 \equiv E\{\zeta_c^2\} = 3\sigma^2/2\varepsilon^2$$

and that these normally distributed slopes are uncorrelated (and hence independent):

$$E\{\zeta_u \zeta_c\} = 0 \ . \tag{2.6}$$

We define the *elevation* of a facet as

$$\zeta = (z_1 + z_2 + z_3)/3 \ . \tag{2.7}$$

Thus ζ is the vertical displacement (in meters) of the facet's centroid above or below the plane of the hexagonal grid. This ζ is a normally distributed random variable of zero mean and variance

$$\sigma_\zeta^2 \equiv E\{\zeta^2\} = \sigma^2/3 \ . \tag{2.8}$$

D. Fixing Scales

We may now determine δ, ε, and the vertical scale σ of the random capillary sea surface as functions of the wind speed U. From the pair (2.5), (2.1) we have

$$\begin{aligned} \delta^2 &= (6a_\zeta/a_u)U^{q-p} \\ \varepsilon^2 &= (9a_\zeta/2a_c)U^{q-p} \ . \end{aligned} \tag{2.9}$$

From this we see that

$$\varepsilon^2/\delta^2 = 3a_u/4a_c \ , \tag{2.10}$$

and hence the shape of a triad is independent of wind speed. Moreover, by (2.8), (2.2) and (2.9),

$$\sigma^2/\delta^2 = (a_u/2)U^p \qquad (2.11)$$
$$\sigma^2/\varepsilon^2 = (2a_c/3)U^p \ .$$

Thus the ratio of the vertical scale to either of the horizontal scales of the capillary surface, as a function of U, depends only on U^p. We now set $p = 1$. Since the shape of a triad is independent of the physical units of δ and ε, from (2.10) we see that we can set $\delta = 1$ (a dimensionless unit) and solve for ε, while (say) from the first equation of (2.11) we can solve for σ. The final results defining the random capillary wave surface therefore are

$$\delta = 1$$
$$\varepsilon = [3a_u/4a_c]^{\frac{1}{2}} \qquad (\delta,\varepsilon,\sigma \text{ dimensionless}) \qquad (2.12)$$
$$\sigma = [(a_u/2)U]^{\frac{1}{2}} \ .$$

Since we have returned to the currently accepted value of $p = 1$, a_u and a_c in (2.12) are as given in (2.1)'. Observe that in the transition to (2.11), the dependence of the triad geometry on q (recall 2.2) has been removed by scaling. Thus a random surface built over the hexagonal grid of Fig. 1 in the manner described above, using triad geometry defined by (2.12), will obey the classic wave-slope wind-speed law of capillary waves. Moreover, the dimensionless horizontal (δ,ε) and vertical (σ) scales of such a surface, for each fixed choice of U, will permit the correct modeling of wave shielding and multiple scattering of light rays. Implicit here is the assumption that

in real life, as in the model, the various numerical attributes (elevation, slope, etc.) of the wave facets in non-adjacent triads are independent random variables. At present the spatial autocorrelation property of a random capillary surface is not known. The present model can be modified when such additional information is available (cf. Appendixes A,B,C).

3. *Ray Tracing*

We now turn our attention to the details of the ray-tracing algorithm. The mathematics involved is no more complicated than determining where a straight line intersects a plane, but the actual application of this procedure to the irregular geometry of the set of wave facets comprising a realization of the random surface requires some attention to detail. After initial comments on notation, we show how to track a ray across the hexagonal grid, identifying those wave facets above or below the grid which are candidates for an intersection with the ray. We then show how to determine whether or not the ray actually intersects a candidate wave facet.

We have already defined a wind-based coordinate system for the hexagonal domain (see Figs. 1, 3). We shall do all our ray tracings in the wind-based system. An arbitrary vector $\underset{\sim}{u}$ in space within the hexagonal domain is represented as

$$\underset{\sim}{u} = u_1\underset{\sim}{i} + u_2\underset{\sim}{j} + u_3\underset{\sim}{k} = (u_1,u_2,u_3)$$

in this coordinate system. We shall make frequent use of unit vectors (those satisfying $\underset{\sim}{u}\cdot\underset{\sim}{u} = u_1^2 + u_2^2 + u_3^2 = 1$) for specifying *directions* of rays, surface normals, and the like. Unit vectors, $\underset{\sim}{u}$, are also conveniently defined in terms of a *zenith angle* $\theta \equiv \arctan(\underset{\sim}{u}\cdot\underset{\sim}{k}) = \arctan(u_3)$ and an *azimuth angle* $\phi \equiv \arctan(u_2/u_1)$, namely

$$\underset{\sim}{u} = (\sin\theta\cos\phi,\ \sin\theta\sin\phi,\ \cos\theta)\ , \quad 0° \le \theta \le 180°,\ 0° \le \phi < 360°,$$

as is shown in Fig. 4. Note that a unit vector $\underset{\sim}{u}_h$ formed from the projection of $\underset{\sim}{u}$ onto the horizontal $\underset{\sim}{i}$-$\underset{\sim}{j}$ plane has components

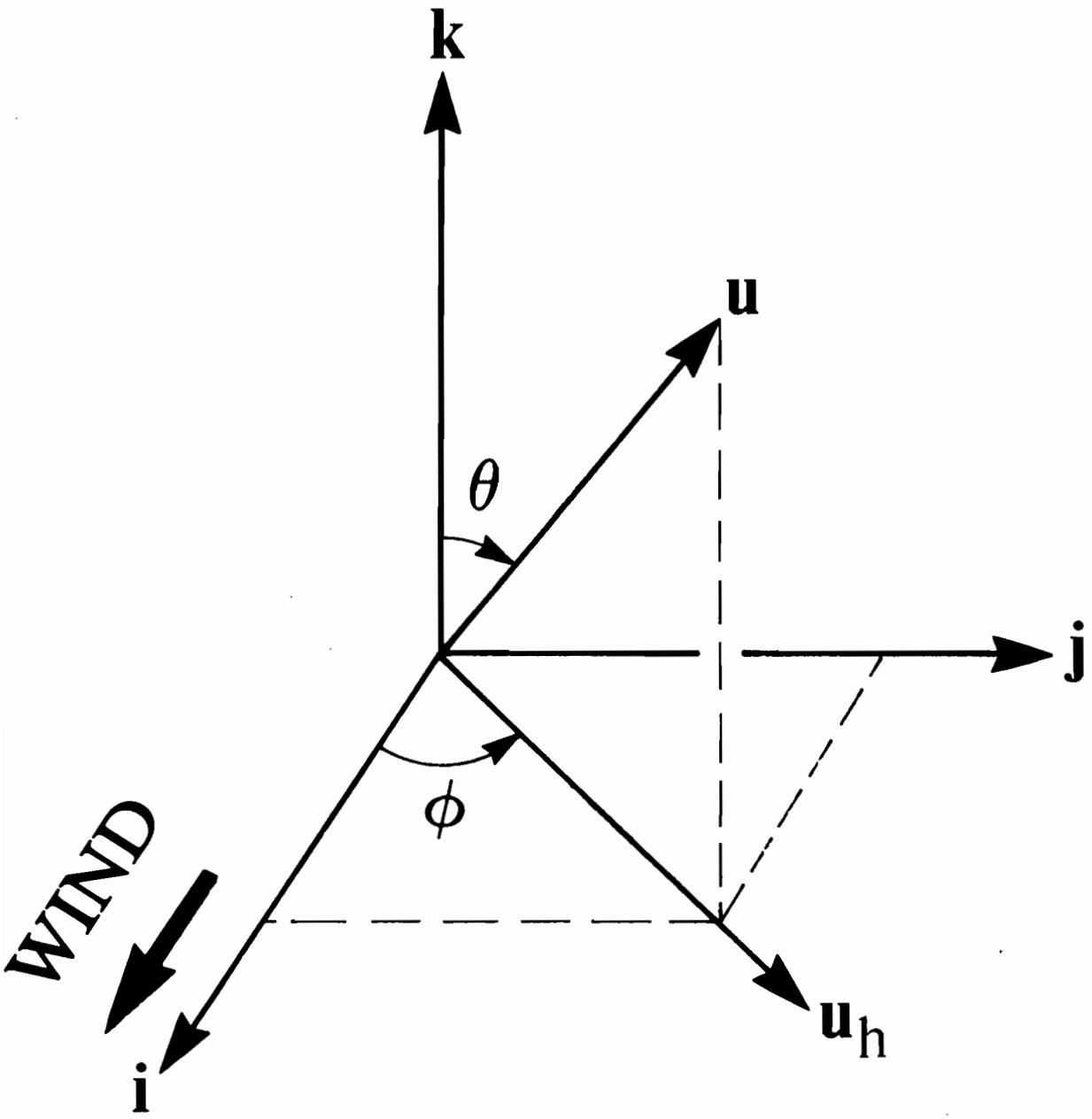

Figure 4.--Vectors represented in the wind-based coordinate system.

$$\underset{\sim}{u}_h = (\cos\phi,\ \sin\phi,\ 0)\ .$$

In subsequent work we use unit vectors $\underset{\sim}{\xi} = (\xi_1,\xi_2,\xi_3) = (\sin\theta\ \cos\phi,\ \sin\theta\ \sin\phi,\ \cos\theta)$ for ray directions. These $\underset{\sim}{\xi}$ are the directions *in which the photons are traveling*. All computations are performed using this convention for ray directions. However, it is often convenient to refer also to the directional location *from which the photons are coming*, e.g., to say "the sun is located at (θ_s,ϕ_s)." Clearly, if the light source is located at (θ_s,ϕ_s), then the associated rays with photons travelling from the source have angles $\theta = 180° - \theta_s$ and $\phi = 180° + \phi_s$ (modulo 360°). Although the context of the usage should prevent confusion between angles specifying source locations and those specifying ray directions, a subscript s on θ and ϕ will explicitly identify angles defining a light source location. Note that for a light source in the "sky," we have $0 \le \theta_s \le 90°$. The associated ray $\underset{\sim}{\xi}$ carrying the photons therefore has $90° \le \theta \le 180°$, so that $\xi_3 = \cos\theta$ is negative, i.e. the ray is heading "downward." ("Upward" is defined as the direction of $\underset{\sim}{k}$ in Fig. 4).

Figure 5 illustrates a hexagonal grid of order n = 2, meaning that there are two "layers" of triads encircling the origin, or equivalently, that the boundary of the hexagon has two triad sides on an edge. The lines forming the sides of the triads have unit vector directions given by

$$\underset{\sim}{r}_1 = (r_{11},r_{21},0) = r_{11}\underset{\sim}{i} + r_{21}\underset{\sim}{j}$$

where $r_{11} = \delta/2\gamma$ and $r_{21} = \varepsilon/\gamma$, and by

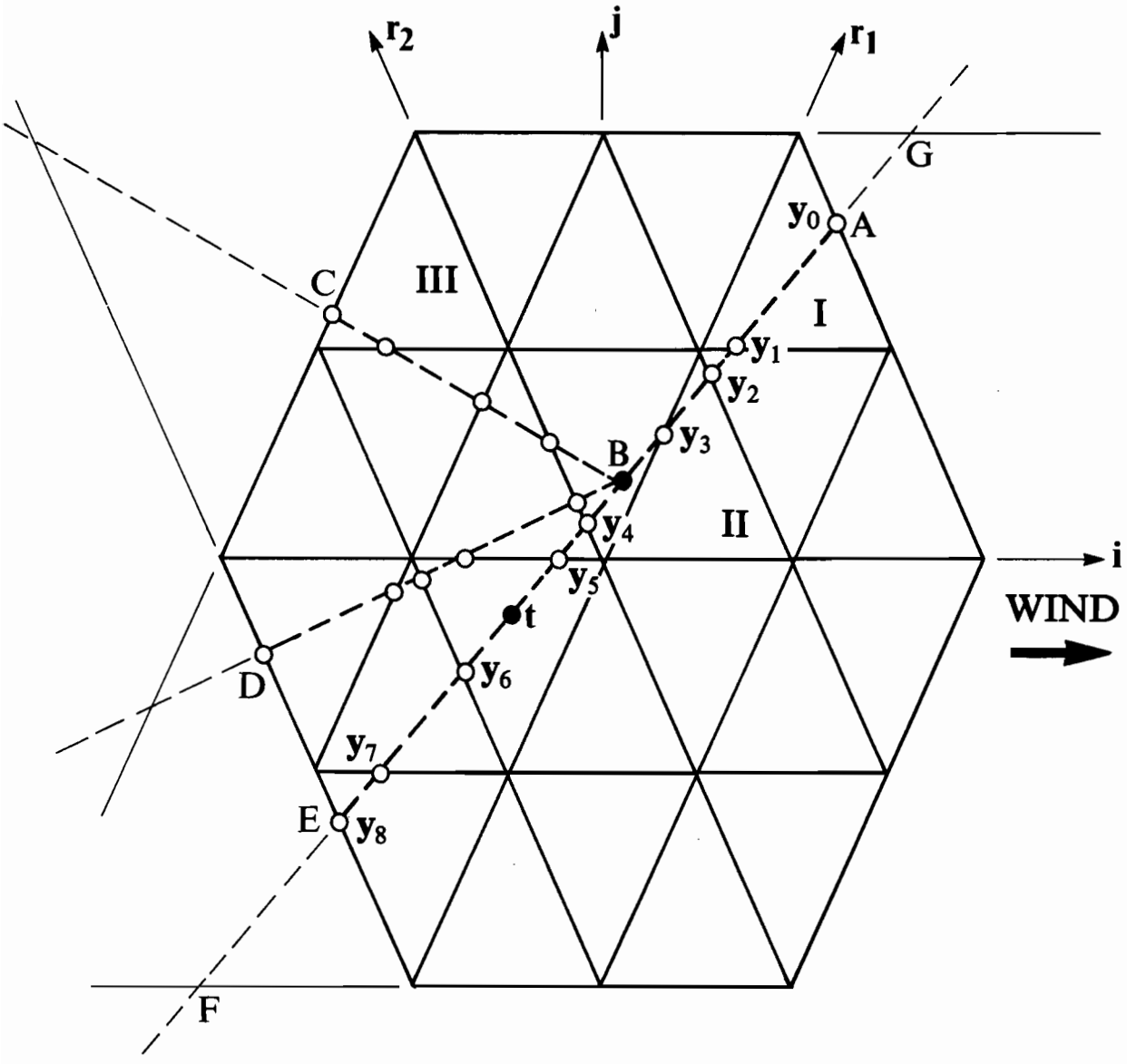

Figure 5.--Wind-based hexagonal grid for the case of order n = 2. Some tracks of rays (e.g. AE, BC, BD) are shown along with triad intercept points y_j.

$$\underset{\sim}{r}_2 = (r_{12}, r_{22}, 0) = r_{12}\underset{\sim}{i} + r_{22}\underset{\sim}{j}$$

where $r_{12} = -\delta/2\gamma = -r_{11}$ and $r_{22} = \varepsilon/\gamma = r_{21}$, and $\gamma = [(\delta/2)^2 + \varepsilon^2]^{\frac{1}{2}}$. Note that

$$\hat{\underset{\sim}{r}}_k \equiv (-r_{2k}, r_{1k}, 0) \quad , \quad k = 1 \text{ or } 2 \tag{3.1}$$

is a vector orthogonal to $\underset{\sim}{r}_k$, i.e., $\underset{\sim}{r}_k \cdot \hat{\underset{\sim}{r}}_k = 0$, k = 1 or 2.

A hexagonal grid of order n has $3n(n + 1) + 1$ triad nodes (the vertices of the triangles), where the elevations of the facet vertices are defined. These nodes are located at $\pm b\delta\underset{\sim}{i} + c\varepsilon\underset{\sim}{j}$ when c is even, for b = 0,1,...,n - c/2; and at $\pm(b + \frac{1}{2})\delta\underset{\sim}{i} + c\varepsilon\underset{\sim}{j}$ when c is odd, for b = 0,1,...,n - (c + 1)/2, where in either the even or odd case we have c = 0,±1,±2,...,±n.

The lines forming the sides of the triads are specified in terms of $\underset{\sim}{i}$, $\underset{\sim}{r}_1$ and $\underset{\sim}{r}_2$ as follows. The "i family" of horizontal lines in Fig. 5 is a family of lines, each of which is a set of points of the form

$$\{\lambda_0\underset{\sim}{i} + c\varepsilon\underset{\sim}{j}: \ \lambda_0 \text{ real}\} \ .$$

That is, the line is generated as λ_0 ranges over the set of real numbers for some fixed c = 0,±1,...,±n. Thus for example, c = 0 is for the horizontal line through the origin; c = n is for the line forming the top boundary of the hexagon; and c = -n is for the line along the lower boundary. The general member of the "r_1 family" of lines is given by

$$\{\lambda_1\underset{\sim}{r}_1 + 2c\varepsilon\underset{\sim}{j}: \ \lambda_1 \text{ real}\} \ ,$$

and the "r_2 family" of lines has members of the form

$$\{\lambda_2 \underset{\sim}{r}_2 + 2c\varepsilon \underset{\sim}{j}: \quad \lambda_2 \text{ real}\}$$

for some fixed $c = 0, \pm 1, \ldots, \pm n$ as before.

A ray *track* is the projection of a ray (in 3-space) onto the two-dimensional hexagonal grid. Thus a ray track is a line segment lying in the hexagonal grid. The dashed lines in Fig. 5 show several ray tracks. Track AE represents a ray whose projection enters the hexagonal grid at A. The ray is traveling in space toward a target point in the grid at $\underset{\sim}{t} = (-\delta/2, -\varepsilon/3, 0)$. If the ray never intersects the wave surface, the track leaves the hexagon at E. If the ray intersects the wave surface at a point below or above point B in the hexagonal grid before reaching $\underset{\sim}{t}$, the ray can generate reflected and refracted daughter rays which have grid tracks BC and BD. The points where a track crosses the sides of the triads are called *triad intercept points* (TIPs). These points are $\underset{\sim}{y}_0, \underset{\sim}{y}_1, \ldots, \underset{\sim}{y}_8$ for track AE in Fig. 5. If a ray track crosses a triad, there are usually two triad intercept points, and we can characterize the crossing by specifying which sides of the triad have the TIPs. Thus triad I in Fig. 5 is said to be of type "ir_2," because one triad intercept point, $\underset{\sim}{y}_1$, lies on a side which is a member of the i family of lines, and the other TIP, $\underset{\sim}{y}_0$, lies on a line which is a member of the r_2 family. Triad II is said to be of type "r_1r_2," and triad III is an example of type "ir_1."

In analyzing the interactions between a ray and the wave facets, two problems must be solved. First, in the case of an incoming ray, we must determine where the ray first enters the hexagonal domain (e.g. point A in Fig. 1), or in the case of a daughter ray, we must determine where the ray

leaves the hexagonal domain (e.g. points D, E and G in Fig. 1). Second, we must determine where, if anywhere, the ray intercepts a wave facet (e.g. points C and F of Fig. 1). We now give the details of these calculations, using the concepts just introduced.

A. Determination of the initial ray point

The present ray tracing algorithm is based on the fact that a ray is defined by an initial point $\underset{\sim}{p}$ and a direction $\underset{\sim}{\xi}$. An initial point $\underset{\sim}{p} = (p_1, p_2, p_3)$ can be either on the boundary of the hexagonal domain (the case of an incoming ray, as at A in Fig. 1) or in the interior of the domain (the case of a daughter ray emanating from the water surface, as at B in Fig. 1). In the case of initializing a new ray, it is convenient to select a *target point* $\underset{\sim}{t}$ generally near the center of the hexagonal grid toward which the ray $\underset{\sim}{\xi}'$ is directed. Therefore, for a given initial direction $\underset{\sim}{\xi}'$, to apply the ray tracing algorithm, before beginning the ray tracing computations, we must locate the initial point $\underset{\sim}{p}'$ where the incoming ray $\underset{\sim}{\xi}'$ enters the hexagonal domain on its way to $\underset{\sim}{t}$.

In general we use a prime to distinguish an "incoming" ray, e.g. at $\underset{\sim}{p}'$ along $\underset{\sim}{\xi}'$. The absence of a prime indicates a reflected or transmitted daughter ray, e.g. $\underset{\sim}{\xi}$. If a distinction is not required, the prime is dropped.

Consider now an incoming light ray traveling at $\underset{\sim}{p}'$ in a direction $\underset{\sim}{\xi}'$ toward a target point $\underset{\sim}{t}$, as shown in Fig. 6. The track of the ray $\underset{\sim}{\xi}'$ is the straight line containing points of the form $\underset{\sim}{t} + s\underset{\sim}{\xi}'_h$, where $\underset{\sim}{\xi}'_h \equiv (\cos\phi, \sin\phi, 0)$ is a unit vector determined from the projection of $\underset{\sim}{\xi}'$ onto the hexagonal grid, and s is a real number, representing distance traveled in the grid away from point $\underset{\sim}{p}'_h$, the projection of $\underset{\sim}{p}'$. As s varies, the point moves along the

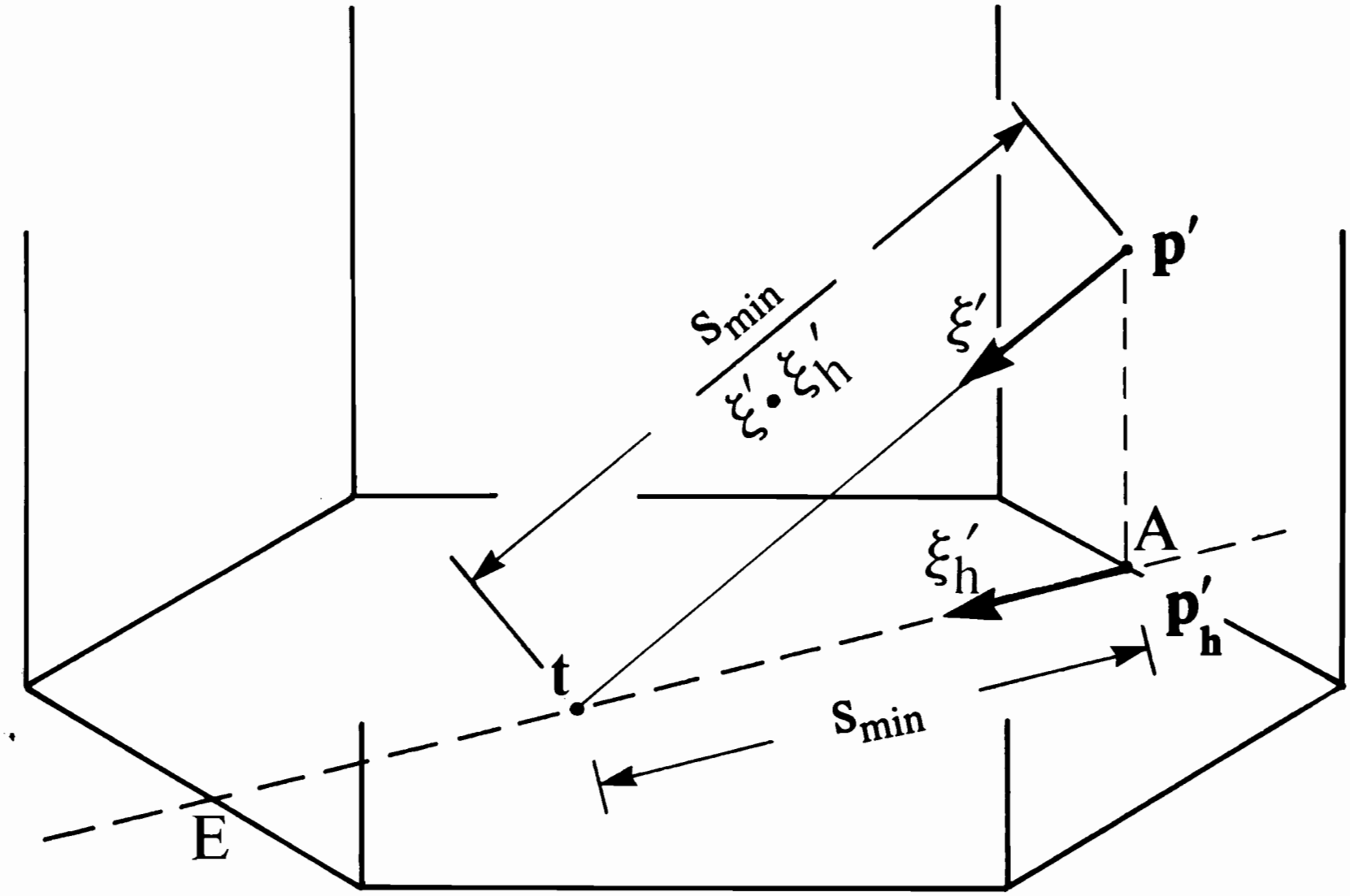

Figure 6.--Geometry for determination of the initial point $\underset{\sim}{p}'$ of an incoming ray $\underset{\sim}{\xi}'$. $\underset{\sim}{p}_h$ is the projection of $\underset{\sim}{p}$ on the hexagonal grid. $\underset{\sim}{t}$ is the target point. The hexagonal domain is the cylindrical region in space formed by a vertical line tracing the perimeter of the hexagonal grid.

track. This track is illustrated as the infinite extension of the dashed line segment AE in Figs. 5 and 6.

Note from Fig. 5 that the track first enters the hexagonal grid at A, where the track crosses a boundary line of the r_2 family. The track has previously crossed an i family boundary line at point G, and the r_1 family boundary line was first crossed at a point beyond the figure. The track also crosses an i family boundary line at point F, an r_2 family boundary line at E, and an r_1 family boundary line at a point not shown.

In general a track $\{\underset{\sim}{t} + s\underset{\sim}{\xi}_h:\ s \text{ real}\}$ intersects the i family of lines in a set of points whose distances s from $\underset{\sim}{t}$ can be found by setting

$$\underset{\sim}{t} + s\underset{\sim}{\xi}_h = \lambda_0 \underset{\sim}{i} + c\varepsilon \underset{\sim}{j}$$

and solving for s. Taking the dot product with $\underset{\sim}{j}$ gives

$$\underset{\sim}{t}\cdot\underset{\sim}{j} + s\underset{\sim}{\xi}_h\cdot\underset{\sim}{j} = c\varepsilon \ ,$$

so that the s values are given by

$$s_0(c,\underset{\sim}{t},\underset{\sim}{\xi}_h) \equiv (c\varepsilon - \underset{\sim}{t}\cdot\underset{\sim}{j})/\underset{\sim}{\xi}_h\cdot\underset{\sim}{j} \tag{3.2}$$

with $c = 0,\pm1,\ldots,\pm n$ and $\underset{\sim}{\xi}_h\cdot\underset{\sim}{j} \neq 0$. Likewise the intersections of the track with the r_1 and r_2 families of lines are found by setting

$$\underset{\sim}{t} + s\underset{\sim}{\xi}_h = \lambda_k \underset{\sim}{r}_k + 2c\varepsilon \underset{\sim}{j} \ , \quad k = 1,2$$

and taking the dot product with $\hat{\underset{\sim}{r}}_k$ of Eq. (3.1) to get

$$s_k(c,\underset{\sim}{t},\xi_h) \equiv (2c\varepsilon \underset{\sim}{j}\cdot\hat{\underset{\sim}{r}}_k - \underset{\sim}{t}\cdot\hat{\underset{\sim}{r}}_k)/\underset{\sim}{\xi}_h\cdot\hat{\underset{\sim}{r}}_k \tag{3.3}$$

for $k = 1,2$, $c = 0,\pm1,\ldots,\pm n$, and $\underset{\sim}{\xi}_h\cdot\tilde{\underset{\sim}{r}}_k \neq 0$. The s_k are the distances from $\underset{\sim}{t}$ at which the track crosses the r_k families of lines. By convention, s_k is measured positive from $\underset{\sim}{t}$ along $-\underset{\sim}{\xi}_h$.

If a ray is started from $\underset{\sim}{t}$ in a direction $-\underset{\sim}{\xi}_h'$, then its track crosses the boundary lines of the r_k family ($k = 1,2$) or i family ($k = 0$) at $s_k(\pm n,\underset{\sim}{t},-\underset{\sim}{\xi}_h')$. In the example of Fig. 5, such a track proceeds from $\underset{\sim}{t}$ towards A (i.e. in the $-\underset{\sim}{\xi}_h'$ direction), building up positive s values until the r_2 boundary line is crossed at point A a distance $s_2(n,\underset{\sim}{t},-\underset{\sim}{\xi}_h')$ from $\underset{\sim}{t}$. The i boundary line is then crossed at point G a greater distance $s_0(n,\underset{\sim}{t},-\underset{\sim}{\xi}_h')$, and finally the r_1 boundary line is crossed at some still greater distance $s_1(n,\underset{\sim}{t},-\underset{\sim}{\xi}_h')$ from $\underset{\sim}{t}$. In this example, we decide that the distance from $\underset{\sim}{t}$ to the hexagonal grid boundary is the positive number $s_2(n,\underset{\sim}{t},-\underset{\sim}{\xi}_h')$. We do not choose points at E and F of Fig. 5 to define the distance because they have negative values $s_2(-n,\underset{\sim}{t},-\underset{\sim}{\xi}_h')$ and $s_0(-n,\underset{\sim}{t},-\underset{\sim}{\xi}_h')$, respectively, measured from $\underset{\sim}{t}$. In general, the six values $s_k(\pm n,\underset{\sim}{t},-\underset{\sim}{\xi}_h')$, $k = 0,1,2$ define points at which a track from $\underset{\sim}{t}$ crosses the hexagonal grid boundary lines. Following the idea in the example just cited, we define the distance from $\underset{\sim}{t}$ to the boundary of the hexagonal grid as

$$s_{min}(\underset{\sim}{t},-\underset{\sim}{\xi}_h') \equiv$$
minimum of the positive values of $\{s_k(\pm n,\underset{\sim}{t},-\underset{\sim}{\xi}_h'):\ k = 0,1,2\}$.

Then the initial point $\underset{\sim}{p}'$ at which the ray $\underset{\sim}{\xi}'$ enters the hexagonal domain on its way to $\underset{\sim}{t}$ is given by

$$\underset{\sim}{p}' = \underset{\sim}{t} - \left[\frac{s_{min}(\underset{\sim}{t},-\underset{\sim}{\xi}_h')}{\underset{\sim}{\xi}'\cdot\underset{\sim}{\xi}_h'}\right]\underset{\sim}{\xi}' \ , \qquad \underset{\sim}{\xi}'\cdot\underset{\sim}{\xi}_h' \neq 0 \ , \tag{3.4}$$

as can be seen geometrically from Fig. 6. Using the initial point $\underset{\sim}{p}'$ from (3.4) and the direction $\underset{\sim}{\xi}'$, we can now proceed with the ray-tracing calculations.

B. Determination of the triad intercept points

Let $\underset{\sim}{p} = (p_1,p_2,p_3)$ be any point in the hexagonal domain or on its boundary, and let $\underset{\sim}{\xi}$ be an arbitrary direction at $\underset{\sim}{p}$. In the following development, it is assumed that $\underset{\sim}{p}$ and $\underset{\sim}{\xi}$ are held fixed. The projection of $\underset{\sim}{p}$ onto the hexagonal grid is $\underset{\sim}{p}_h = (p_1,p_2,0)$, and $\underset{\sim}{\xi}_h$ is the unit vector determined as before from the projection of $\underset{\sim}{\xi}$. Then $\underset{\sim}{p}_h + s\,\underset{\sim}{\xi}_h$, as s varies over all real values, generates the track of the ray. The distances from $\underset{\sim}{p}_h$ to the intercepts of the track with the families of lines defining the triads are then given by equations analogous to (3.2) and (3.3). For the i family we have

$$s_0(c,\underset{\sim}{p}_h,\underset{\sim}{\xi}_h) \equiv (c\varepsilon - \underset{\sim}{p}_h\cdot\underset{\sim}{j})/\underset{\sim}{\xi}_h\cdot\underset{\sim}{j} \ ,$$

and for the r_k families we have (3.5)

$$s_k(c,\underset{\sim}{p}_h,\underset{\sim}{\xi}_h) \equiv (2c\varepsilon\underset{\sim}{j}\cdot\hat{\underset{\sim}{r}}_k - \underset{\sim}{p}_h\cdot\hat{\underset{\sim}{r}}_k)/\underset{\sim}{\xi}_h\cdot\hat{\underset{\sim}{r}}_k \ , \qquad k = 1,2$$

where $c = 0,\pm1,\ldots,\pm n$. Following the pattern of definition of $s_{min}(\underset{\sim}{t},-\underset{\sim}{\xi}_h')$, the distance from $\underset{\sim}{p}_h$ to the boundary of the hexagon is now defined as

$$s_{min}(\underset{\sim}{p}_h,\underset{\sim}{\xi}_h) =$$
$$\text{minimum of the positive values of } \{s_k(\pm n,\underset{\sim}{p}_h,\underset{\sim}{\xi}_h): \ k = 0,1,2\} \tag{3.6}$$

Eq. (3.5) for $s_k(c,\underset{\sim}{p}_h,\underset{\sim}{\xi}_h)$, k = 0,1,2, defines the distances (positive along $\underset{\sim}{\xi}_h$) from $\underset{\sim}{p}_h$ to all possible intersections of the track with the lines which define the triad boundaries. However, only those $s_k(c,\underset{\sim}{p}_h,\underset{\sim}{\xi}_h)$ values between 0 and $s_{min}(\underset{\sim}{p}_h,\underset{\sim}{\xi}_h)$ are within the hexagon. For track AE of Fig. 5, the TIP (triad intercept point) $\underset{\sim}{y}_0$ is at a distance $s_2(2,\underset{\sim}{p}_h,\underset{\sim}{\xi}_h) = 0$ from A (i.e. the first TIP is $\underset{\sim}{y}_0 = \underset{\sim}{p}_h$). TIP $\underset{\sim}{y}_1$ is at a distance $s_0(1, \underset{\sim}{p}_h,\underset{\sim}{\xi}_h)$ from A, and so on until $\underset{\sim}{y}_8$ at E is reached at a distance $s_{min}(\underset{\sim}{p}_h,\underset{\sim}{\xi}_h) = s_2(-2,\underset{\sim}{p},\underset{\sim}{\xi}_h)$ from A. Note that as we proceed from $\underset{\sim}{p}_h$ to the boundary of the hexagon, the $s_k(c,\underset{\sim}{p}_h,\underset{\sim}{\xi}_h)$ values can occur in any order of k = 0, 1, or 2 in the encountered sequence of triad intercept points $\underset{\sim}{y}_j$, j = 0,1,2,...,m. Thus in Fig. 5, $\underset{\sim}{y}_0$ is associated with an s-value from the k = 2 family, $\underset{\sim}{y}_1$ with k = 0, $\underset{\sim}{y}_2$ with k = 2, $\underset{\sim}{y}_3$ with k = 1, and so on. It will be necessary to know which "k family" of distances $s_k(c,\underset{\sim}{p}_h,\underset{\sim}{\xi}_h)$ is associated with each TIP $\underset{\sim}{y}_j$. Toward this end, let "s(j)" denote the $s_k(c,\underset{\sim}{p}_h,\underset{\sim}{\xi}_h)$ value associated with TIP $\underset{\sim}{y}_j$, and let "κ(j)" denote the k family of s(j). Thus $\kappa(j) = 0$, 1 or 2, depending on whether k = 0, 1 or 2 for the $s_k(c,\underset{\sim}{p}_h,\underset{\sim}{\xi}_h)$ value belonging to $\underset{\sim}{y}_j$. With this notation, the triad intercept points are given by

$$\underset{\sim}{y}_j = \underset{\sim}{p}_h + s(j)\underset{\sim}{\xi}_h \qquad j = 0,1,2,\ldots,m. \tag{3.7}$$

The maximum possible value of m is 4n, an example of which is track AE of Fig. 5 (track BC has m = 3 and track BD has m = 4).

In practice the triad intercept points are found by the following steps: (1) generating all possible $s_k(c,\underset{\sim}{p}_h,\underset{\sim}{\xi}_h)$ values by Eq. (3.5); (2) finding $s_{min}(\underset{\sim}{p}_h,\underset{\sim}{\xi}_h)$ by Eq. (3.6); (3) recording all s_k-distances, as c varies, such that $0 \le s_k(c,\underset{\sim}{p}_h,\underset{\sim}{\xi}_h) \le s_{min}(\underset{\sim}{p}_h,\underset{\sim}{\xi})$ holds; (4) ordering the values of

step 3 from smallest to largest; (5) relabeling these ordered values as "s(j)", with j = 0 for the smallest value of step 4, namely $s_k(c,\underset{\sim}{p}_h,\underset{\sim}{\xi}_h) \equiv s(0)$, to j = m for the largest value $s_{min}(\underset{\sim}{p}_h,\underset{\sim}{\xi}_h) \equiv s(m)$; (6) recording the k values associated with each j value of step 5 according to the $\kappa(j)$ notation; and (7) generating the ordered TIP values $\underset{\sim}{y}_j$ from (3.7).

C. Determination of the triad vertices

We now show how to recover the locations of the triad vertices from the triad intercept points. This capability will enable us to identify those facets which are candidates for interaction with the ray, since triads (and their associated facets) are uniquely determined by the coordinates of their vertices.

Consider a triad which is crossed by a track of type r_1r_2. Triad II of Fig. 5 is an example. Figure 7 illustrates in greater detail the geometry of an r_1r_2 triad. The triad intercept points $\underset{\sim}{y}_{j_1} \equiv \underset{\sim}{y}_1$ and $\underset{\sim}{y}_{j_2} \equiv \underset{\sim}{y}_2$ locate an arbitrary pair of type r_1r_2 triad intercept points (i.e. either $j_2 = j_1 + 1$ or $j_1 = j_2 + 1$). The notation "$\underset{\sim}{y}_1$" and "$\underset{\sim}{y}_2$" is used only for convenience to label which TIP ($\underset{\sim}{y}_k$) lies on which side ($\underset{\sim}{r}_k$) of the triad. The triad intercept points $\underset{\sim}{y}_1$ and $\underset{\sim}{y}_2$ have the associated distances $s(1) \equiv s(j_1)$ and $s(2) \equiv s(j_2)$, respectively (cf. (3.7)). Clearly $\kappa(j_1) + \kappa(j_2) \equiv \kappa(1) + \kappa(2) = 3$ if and only if the triad crossing is of type r_1r_2.

Since TIP $\underset{\sim}{y}_k$ lies on a line of the $\underset{\sim}{r}_k$ family, k = 1 or 2, we can write, with the help of Fig. 7:

$$\underset{\sim}{y}_k = \underset{\sim}{p}_h + s(k)\underset{\sim}{\xi}_h = \lambda_k\underset{\sim}{r}_k + d_k\underset{\sim}{j} \; . \qquad (r_1r_2 \text{ case})$$

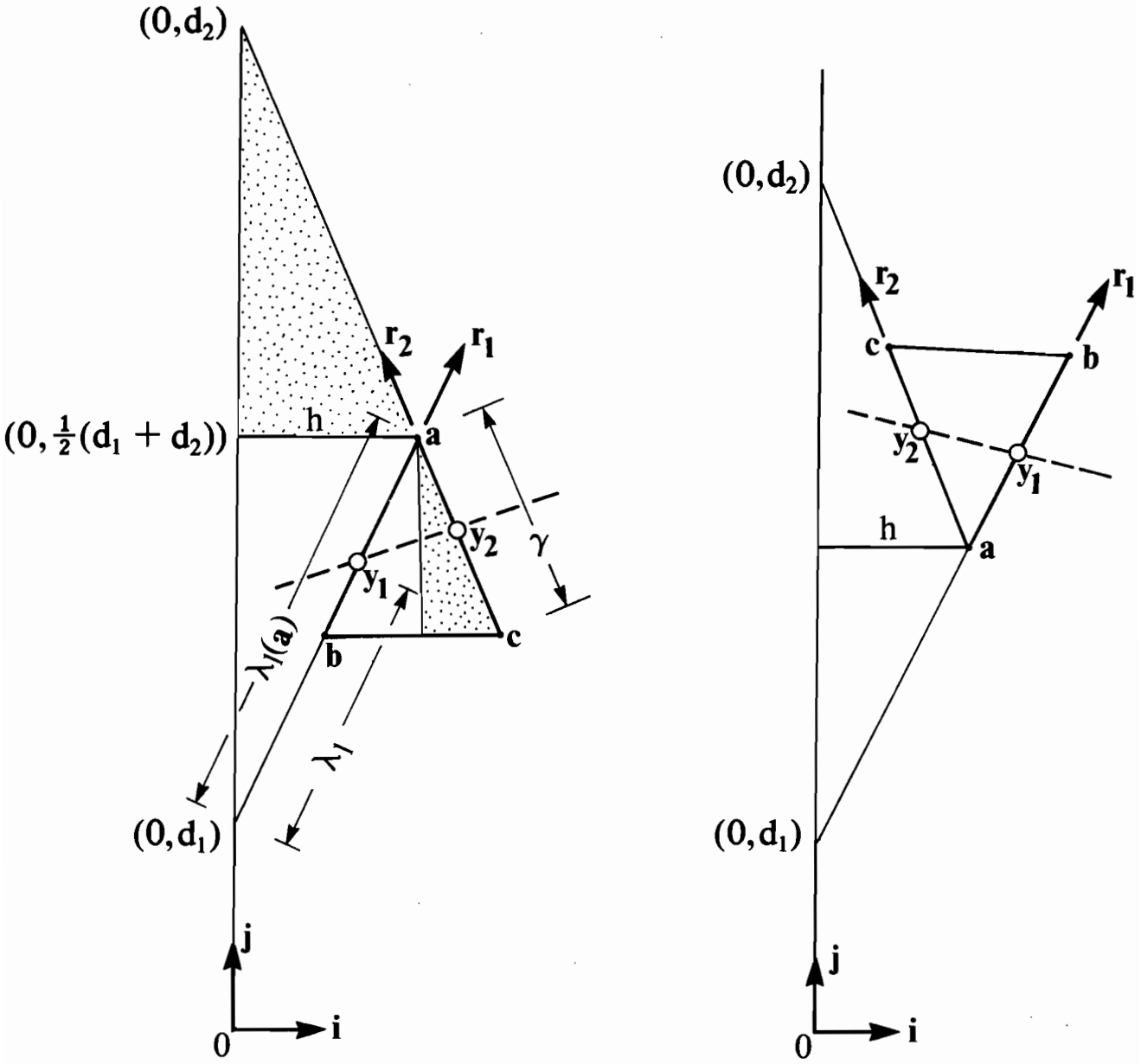

Figure 7.--Geometric relations for determination of the triad vertices $\underset{\sim}{a}$, $\underset{\sim}{b}$ and $\underset{\sim}{c}$ from triad intercept points $\underset{\sim}{y}_1$ and $\underset{\sim}{y}_2$ which are of type r_1r_2.

The rightmost equation above is illustrated in Fig. 7 for k = 1. d_1 and d_2 are as defined in the Figure. Taking the dot product with $\hat{\underset{\sim}{r}}_k$ yields d_k:

$$d_k = [\underset{\sim}{p}_h + s(k)\underset{\sim}{\xi}_h]\cdot\hat{\underset{\sim}{r}}_k/\underset{\sim}{j}\cdot\hat{\underset{\sim}{r}}_k = \hat{\underset{\sim}{y}}_k\cdot\hat{\underset{\sim}{r}}_k/\underset{\sim}{j}\cdot\hat{\underset{\sim}{r}}_k \ , \ k = 1,2. \qquad (3.8)$$

(r_1r_2 case)

Since vertex $\underset{\sim}{a}$, as shown in Fig. 7, lies on the $\underset{\sim}{r}_k$ lines, we have for some $\lambda_k \equiv \lambda_k(\underset{\sim}{a})$,

$$\lambda_k(\underset{\sim}{a})\underset{\sim}{r}_k + d_k\underset{\sim}{j} = \underset{\sim}{a} \ , \ k = 1,2. \qquad (r_1r_2 \text{ case})$$

From this we find

$$\lambda_k(\underset{\sim}{a}) = (\underset{\sim}{a} - d_k\underset{\sim}{j})\cdot\underset{\sim}{r}_k \quad , \quad k = 1,2 \ . \qquad (r_1r_2 \text{ case}) \quad (3.9)$$

Since $\underset{\sim}{y}_k$ lies on an $\underset{\sim}{r}_k$ line, we find in the same way that

$$\lambda_k = (\underset{\sim}{y}_k - d_k\underset{\sim}{j})\cdot\underset{\sim}{r}_k \quad , \quad k = 1, 2. \qquad (r_1r_2 \text{ case}) \quad (3.10)$$

Note that d_k, λ_k, and $\lambda_k(\underset{\sim}{a})$ can be positive or negative, depending on the location of the triad in the hexagonal grid. The quantities d_k, for k = 1,2 along with λ_1, and $\lambda_1(\underset{\sim}{a})$ are explicitly shown in Fig. 7. From similar triangles, shown shaded in Fig. 7, we have

$$\frac{h}{\frac{1}{2}(d_2 - d_1)} = \frac{\frac{1}{2}\delta}{\varepsilon}$$

or

$$h = (d_2 - d_1)\delta/4\varepsilon \ , \qquad (3.11)$$

where h is defined geometrically in Fig. 7, and δ,ε are shown in Fig. 3.

We can now write $\underset{\sim}{a}$ in terms of quantities computed from the triad intercept points:

$$\underset{\sim}{a} = h\underset{\sim}{i} + \tfrac{1}{2}(d_1 + d_2)\underset{\sim}{j} \ .$$

Defining

$$\text{sign}[x] \equiv \begin{cases} +1 \text{ if } x > 0 \\ -1 \text{ if } x < 0 \ , \end{cases}$$

we can write $\underset{\sim}{b}$ and $\underset{\sim}{c}$ as

$$\underset{\sim}{b} = \underset{\sim}{a} + \text{sign}[\lambda_1 - \lambda_1(a)]\gamma\underset{\sim}{r}_1$$
$$\underset{\sim}{c} = \underset{\sim}{a} + \text{sign}[\lambda_2 - \lambda_2(a)]\gamma\underset{\sim}{r}_2 \ ,$$

where γ is shown in Fig. 7 (cf. Fig. 3). Recalling the definitions of $\underset{\sim}{r}_1 \equiv (\delta/2\gamma)\underset{\sim}{i} + (\varepsilon/\gamma)\underset{\sim}{j}$ and $\underset{\sim}{r}_2 \equiv (-\delta/2\gamma)\underset{\sim}{i} + (\varepsilon/\gamma)\underset{\sim}{j}$, we can write $\underset{\sim}{a}$, $\underset{\sim}{b}$, and $\underset{\sim}{c}$ in terms of the $\underset{\sim}{i}$ and $\underset{\sim}{j}$ unit vectors and the quantities computed from the triad intercept points:

$$\underset{\sim}{a} = h\underset{\sim}{i} + \tfrac{1}{2}(d_1 + d_2)\underset{\sim}{j} \equiv (a_1, a_2, 0) \qquad (r_1r_2 \text{ case}) \quad (3.12a)$$

$$\underset{\sim}{b} = (a_1 + \text{sign}[\lambda_1 - \lambda_1(\underset{\sim}{a})]\tfrac{\delta}{2})\underset{\sim}{i} + (a_2 + \text{sign}[\lambda_1 - \lambda_1(\underset{\sim}{a})]\varepsilon)\underset{\sim}{j} \quad (3.12b)$$

$$\underset{\sim}{c} = (a_1 - \text{sign}[\lambda_2 - \lambda_2(\underset{\sim}{a})]\tfrac{\delta}{2})\underset{\sim}{i} + (a_2 + \text{sign}[\lambda_2 - \lambda_2(\underset{\sim}{a})]\varepsilon)\underset{\sim}{j}. \quad (3.12c)$$

Observe that these equations hold for both possible triad orientations of the r_1r_2 case shown in Fig. 7, as well as for the instances where the triad is to the left of the origin (in which case h is negative). Therefore given a pair of triad intercept points $\underset{\sim}{y}_{j_1}$ and $\underset{\sim}{y}_{j_2}$, we need only check the sum $\kappa(j_1) + \kappa(j_2)$. If this sum is 3, then Eqs. (3.8)-(3.12) immediately give the vertices of the triad.

Figure 8 shows the geometries of the remaining two types of triad intercepts, namely ir_1 and ir_2. Labeling the TIP (triad intercept point) which is on the i-side of the triad as "$\underset{\sim}{y}_0$", and with "$\underset{\sim}{y}_k$" as usual denoting the TIP on the $\underset{\sim}{r}_k$-side (k = 1 or 2), the analysis proceeds just as in the r_1r_2 case. The relevant equations are given below.

For triad intercept type ir_1, for which $\kappa(j_0) + \kappa(j_1) = 1$, we have (since $\underset{\sim}{y}_0$ lies on an i line)

$$\underset{\sim}{y}_0 = \underset{\sim}{p}_h + s(0)\underset{\sim}{\xi}_h = \lambda_0\underset{\sim}{i} + d_0\underset{\sim}{j}$$

whence

$$d_0 = \underset{\sim}{y}_0\cdot\underset{\sim}{j} \ .$$

Moreover, since $\underset{\sim}{a}$, as shown in Fig. 8, also lies on an i line we can write

$$\underset{\sim}{a} = \lambda_0(\underset{\sim}{a})\underset{\sim}{i} + d\underset{\sim}{j}$$

whence

$$\lambda_0(\underset{\sim}{a}) = \underset{\sim}{a}\cdot\underset{\sim}{i} \ .$$

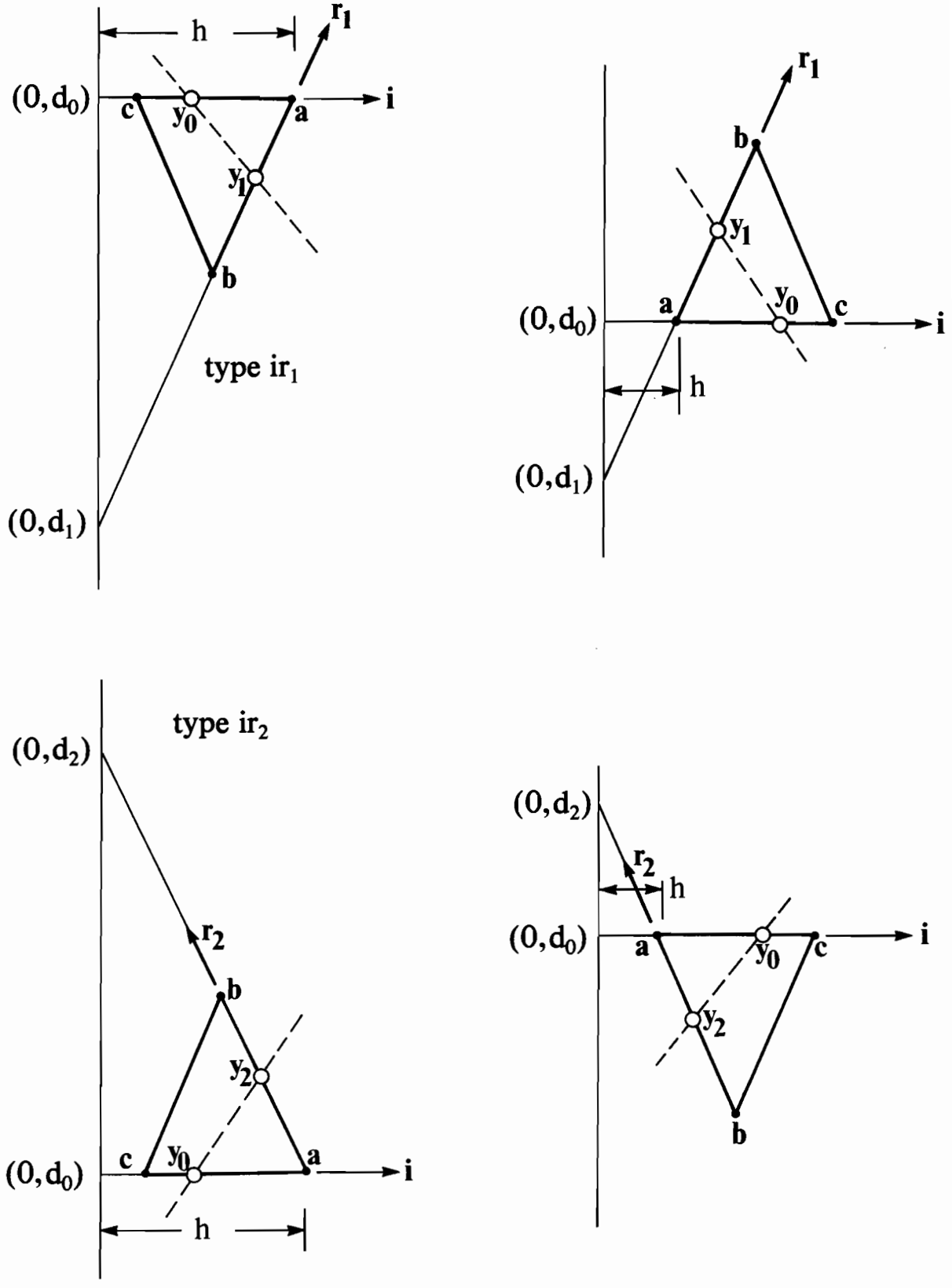

Figure 8.--Geometric relations as in Fig. 7 for triad intercept types ir_1 (top panel) and ir_2 (bottom panel).

Similarly

$$\lambda_0 = \underset{\sim}{y}_0 \cdot \underset{\sim}{i} \ .$$

Since $\underset{\sim}{y}_1$ lies on an r_1 line, we have d_1 given by (3.8), $\lambda_1(\underset{\sim}{a})$ by (3.9) and λ_1 by (3.10). As before, similar triangles give

$$\frac{h}{d_0 - d_1} = \frac{\frac{1}{2}\delta}{\varepsilon}$$

or

$$h = (d_0 - d_1)\delta/2\varepsilon \ .$$

The final equations for the triad vertices are

$$\underset{\sim}{a} = h\underset{\sim}{i} + d_0\underset{\sim}{j} \equiv (a_1, a_2, 0) \qquad (ir_1 \text{ case}) \quad (3.13a)$$

$$\underset{\sim}{b} = \underset{\sim}{a} + \text{sign}[\lambda_1 - \lambda_1(\underset{\sim}{a})]\gamma\underset{\sim}{r}_1$$

$$= (a_1 + \text{sign}[\lambda_1 - \lambda_1(\underset{\sim}{a})]\frac{\delta}{2})\underset{\sim}{i} + (a_2 + \text{sign}[\lambda_1 - \lambda_1(\underset{\sim}{a})]\varepsilon)\underset{\sim}{j} \quad (3.13b)$$

$$\underset{\sim}{c} = \underset{\sim}{a} + \text{sign}[\lambda_0 - \lambda_0(\underset{\sim}{a})]\delta\underset{\sim}{i}$$

$$= (a_1 + \text{sign}[\lambda_0 - \lambda_0(\underset{\sim}{a})]\delta)\underset{\sim}{i} + a_2\underset{\sim}{j} \quad (3.13c)$$

for type ir_1 or $\kappa(j_0) + \kappa(j_1) = 1$.

For triad intercept ir_2, for which $\kappa(j_0) + \kappa(j_2) = 2$, an identical analysis leads to the final equations

$$h = (d_2 - d_0)\delta/2\varepsilon \qquad (ir_2 \text{ case})$$

and

$$\underset{\sim}{a} = h\underset{\sim}{i} + d_0\underset{\sim}{j} \equiv (a_1, a_2, 0) \tag{3.14a}$$

$$\underset{\sim}{b} = \underset{\sim}{a} + \text{sign}[\lambda_2 - \lambda_2(\underset{\sim}{a})]\gamma\underset{\sim}{r}_2$$

$$= (a_1 - \text{sign}[\lambda_2 - \lambda_2(\underset{\sim}{a})]\tfrac{\delta}{2})\underset{\sim}{i} + (a_2 + \text{sign}[\lambda_2 - \lambda_2(\underset{\sim}{a})]\varepsilon)\underset{\sim}{j} \tag{3.14b}$$

$$\underset{\sim}{c} = \underset{\sim}{a} + \text{sign}[\lambda_0 - \lambda_0(\underset{\sim}{a})]\delta\underset{\sim}{i}$$

$$= (a_1 + \text{sign}[\lambda_0 - \lambda_0(\underset{\sim}{a})]\delta)\underset{\sim}{i} + a_2\underset{\sim}{j} \ . \tag{3.14c}$$

Here $\lambda_2(\underset{\sim}{a})$, λ_2 are given by (3.9), (3.10), and d_2 is given by (3.8).

Given any possible geometry for a track crossing a triad, we can now immediately obtain the vertices of the triad by either Eqs. (3.12), (3.13) or (3.14).

D. Determination of the facet intersection point

The elevations of the random sea surface are defined at the nodes of the hexagonal grid, i.e. at the triad vertices. Given the triad vertices $\underset{\sim}{a}$, $\underset{\sim}{b}$ and $\underset{\sim}{c}$, we can immediately obtain the vertices $\underset{\sim}{v}_1$, $\underset{\sim}{v}_2$ and $\underset{\sim}{v}_3$ (in 3-space) of the associated wave facet:

$$\underset{\sim}{v}_1 = \underset{\sim}{a} + z_a \underset{\sim}{k}$$

$$\underset{\sim}{v}_2 = \underset{\sim}{b} + z_b \underset{\sim}{k} \qquad (3.15)$$

$$\underset{\sim}{v}_3 = \underset{\sim}{c} + z_c \underset{\sim}{k} \ .$$

In Eq. (3.15), z_a, z_b and z_c the random elevations of the sea surface at nodes $\underset{\sim}{a}$, $\underset{\sim}{b}$ and $\underset{\sim}{c}$, respectively, of the hexagonal grid. These z's are found as explained in section 2C. As always, $\underset{\sim}{k} = (0,0,1)$ is the unit vector normal to the mean sea surface.

Let "$F(\underset{\sim}{v}_1,\underset{\sim}{v}_2,\underset{\sim}{v}_3)$" denote the wave facet defined by (3.15). Then a unit normal to this facet is given by

$$\underset{\sim}{n}_1 \equiv (\underset{\sim}{v}_3 - \underset{\sim}{v}_1) \times (\underset{\sim}{v}_2 - \underset{\sim}{v}_1)/\|(\underset{\sim}{v}_3 - \underset{\sim}{v}_1) \times (\underset{\sim}{v}_2 - \underset{\sim}{v}_1)\| \ ,$$

where $\underset{\sim}{u} \times \underset{\sim}{v}$ is the usual vector cross product of vectors $\underset{\sim}{u}$ and $\underset{\sim}{v}$, and $\|\underset{\sim}{v}\|$ is the length of the vector $\underset{\sim}{v}$. The unit *outward* normal $\underset{\sim}{n}$ to the facet $F(\underset{\sim}{v}_1,\underset{\sim}{v}_2,\underset{\sim}{v}_3)$ is such that $\underset{\sim}{n}\cdot\underset{\sim}{k} > 0$, and is obtained from

$$\underset{\sim}{n} = \text{sign}[\underset{\sim}{n}_1\cdot\underset{\sim}{k}]\underset{\sim}{n}_1 \ .$$

Consider a plane in space with normal $\underset{\sim}{n}$ and let $\underset{\sim}{v}$ be a point in the plane. A necessary and sufficient condition for another point $\underset{\sim}{q}$ to lie in the plane is

$$(\underset{\sim}{q} - \underset{\sim}{v})\cdot\underset{\sim}{n} = 0 \ .$$

Moreover, the condition that the same point $\underset{\sim}{q}$ lie on the ray $\{\underset{\sim}{p} + s\underset{\sim}{\xi}:\ s \text{ real}\}$ is

$$\underset{\sim}{q} = \underset{\sim}{p} + s(\underset{\sim}{q})\underset{\sim}{\xi} ,$$

where $s(\underset{\sim}{q})$ is the distance along the ray from $\underset{\sim}{p}$ to $\underset{\sim}{q}$ in the plane. We can solve for $s(\underset{\sim}{q})$ from

$$(\underset{\sim}{q} - \underset{\sim}{v}_1)\cdot\underset{\sim}{n} = (\underset{\sim}{p} + s(\underset{\sim}{q})\underset{\sim}{\xi} - \underset{\sim}{v}_1)\cdot\underset{\sim}{n} = 0$$

whence

$$s(\underset{\sim}{q}) = (\underset{\sim}{v}_1 - \underset{\sim}{p})\cdot\underset{\sim}{n}/\underset{\sim}{\xi}\cdot\underset{\sim}{n}$$

where we have explicitly chosen vertex $\underset{\sim}{v}_1$ of the facet $F(\underset{\sim}{v}_1,\underset{\sim}{v}_2,\underset{\sim}{v}_3)$ in (3.15) for the point $\underset{\sim}{v}$ in the plane.

We are therefore guaranteed, by construction of $s(\underset{\sim}{q})$, that a point $\underset{\sim}{q}$ of a ray lies somewhere in the plane determined by the three vertices of wave facet $F(\underset{\sim}{v}_1,\underset{\sim}{v}_2,\underset{\sim}{v}_3)$. Point $\underset{\sim}{q}$ in particular lies in the subset of the plane bounded by the facet itself if and only if

$$s(j_1) < s(\underset{\sim}{q})\underset{\sim}{\xi}\cdot\underset{\sim}{\xi}_h < s(j_2) , \tag{3.16}$$

where j_1 and j_2 label the two triad intercept points associated with the wave facet, and where $s(j)$ is as defined for (3.7).

We interpret and use (3.16) as follows. Given a ray emanating from $\underset{\sim}{p}$ in direction $\underset{\sim}{\xi}$, the track $\{\underset{\sim}{p}_h + s\underset{\sim}{\xi}_h:\ s \text{ real}\}$ across the hexagonal grid produces the triad intercept points $\underset{\sim}{y}_0,\underset{\sim}{y}_1,\ldots,\underset{\sim}{y}_m$. Each pair of intercepts $(\underset{\sim}{y}_j,\underset{\sim}{y}_{j+1})$, $j = 0,1,\ldots,m-1$, determines the vertices $\underset{\sim}{a},\underset{\sim}{b}$ and $\underset{\sim}{c}$ of the associated triad,

and thus the wave facet $F(\underset{\sim}{y}_1,\underset{\sim}{y}_2,\underset{\sim}{y}_3)$. The triad intercept points $\underset{\sim}{y}_j$ and $\underset{\sim}{y}_{j+1}$ are at distances s(j) and s(j+1), respectively, from $\underset{\sim}{p}_h$ along direction $\underset{\sim}{\xi}_h$. If the ray $\{\underset{\sim}{p} + s\underset{\sim}{\xi}:\ s \text{ real}\}$ intercepts the facet $F(\underset{\sim}{y}_1,\underset{\sim}{y}_2,\underset{\sim}{y}_3)$ at $\underset{\sim}{q}$, a distance $s(\underset{\sim}{q})$ from $\underset{\sim}{p}$ along $\underset{\sim}{\xi}$, then the horizontal projection in the plane of the hexagonal grid of the distance $s(\underset{\sim}{q})$ from $\underset{\sim}{p}$ to $\underset{\sim}{q}$, $s(\underset{\sim}{q})\underset{\sim}{\xi}\cdot\underset{\sim}{\xi}_h$, must lie between the indicated limits in (3.16). If (3.16) is not satisfied, then the ray $\{\underset{\sim}{p} + s\underset{\sim}{\xi}:\ s \text{ real}\}$ does not intercept the facet.

Whether or not a ray intercepts a sea surface facet within the hexagonal domain can be determined by systematically checking, in the above manner, each pair of triad intercept points, namely $(\underset{\sim}{y}_0,\underset{\sim}{y}_1)$, $(\underset{\sim}{y}_1,\underset{\sim}{y}_2)$, $(\underset{\sim}{y}_2,\underset{\sim}{y}_3),\ldots,$ $(\underset{\sim}{y}_{m-1},\underset{\sim}{y}_m)$. Either the ray will intercept one of the facets at a point $\underset{\sim}{q}$, or the sequence of triad intercept pairs $(\underset{\sim}{y}_j,\underset{\sim}{y}_{j+1})$ will be exhausted without ever satisfying (3.16), in which case the ray leaves the hexagonal domain without striking the sea surface.

E. Determination of reflected and transmitted rays

Suppose that a ray $\underset{\sim}{\xi}'$ has been found to intercept at point $\underset{\sim}{q}$ a wave facet whose unit outward normal is $\underset{\sim}{n}$. Let N' be the radiance of the incident ray. This ray generally gives rise to two daughter rays at $\underset{\sim}{q}$. Suppose that the reflected daughter ray along $\underset{\sim}{\xi}_r$ has radiance N_r and the refracted daughter ray along $\underset{\sim}{\xi}_t$ has radiance N_t. We now show how to calculate $\underset{\sim}{\xi}_r,\underset{\sim}{\xi}_t$ and N_r,N_t. In order to do this it is necessary to distinguish between the cases where $\underset{\sim}{\xi}'$ at $\underset{\sim}{q}$ is air- or water-incident, i.e., where $\underset{\sim}{\xi}'$ arrives at $\underset{\sim}{q}$ via a path through the air or water. In the *air-incident* case we have $\underset{\sim}{\xi}'\cdot\underset{\sim}{n} < 0$, while in the *water-incident* case $\underset{\sim}{\xi}'\cdot\underset{\sim}{n} > 0$. (Recall that $\underset{\sim}{n}$ in paragraph D above is defined with the help of the vertical upward direction $\underset{\sim}{k}$). Figure 9 shows the geometric relations between incident, reflected and transmitted (refracted) rays in

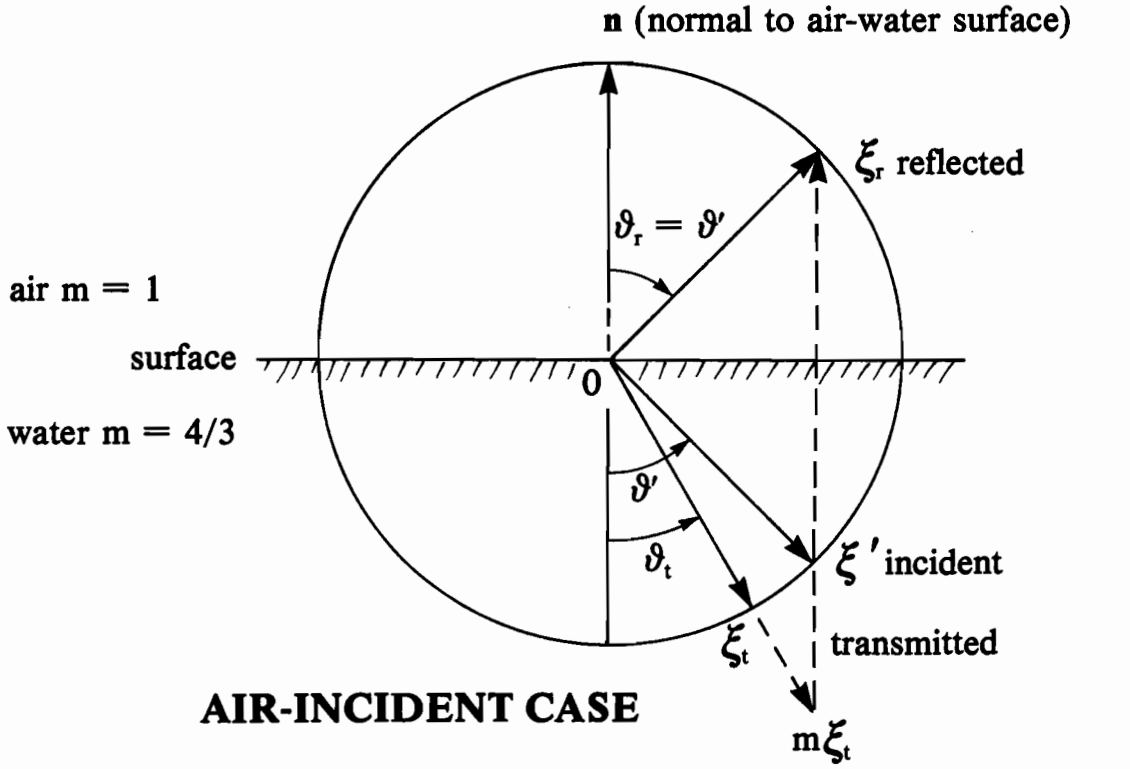

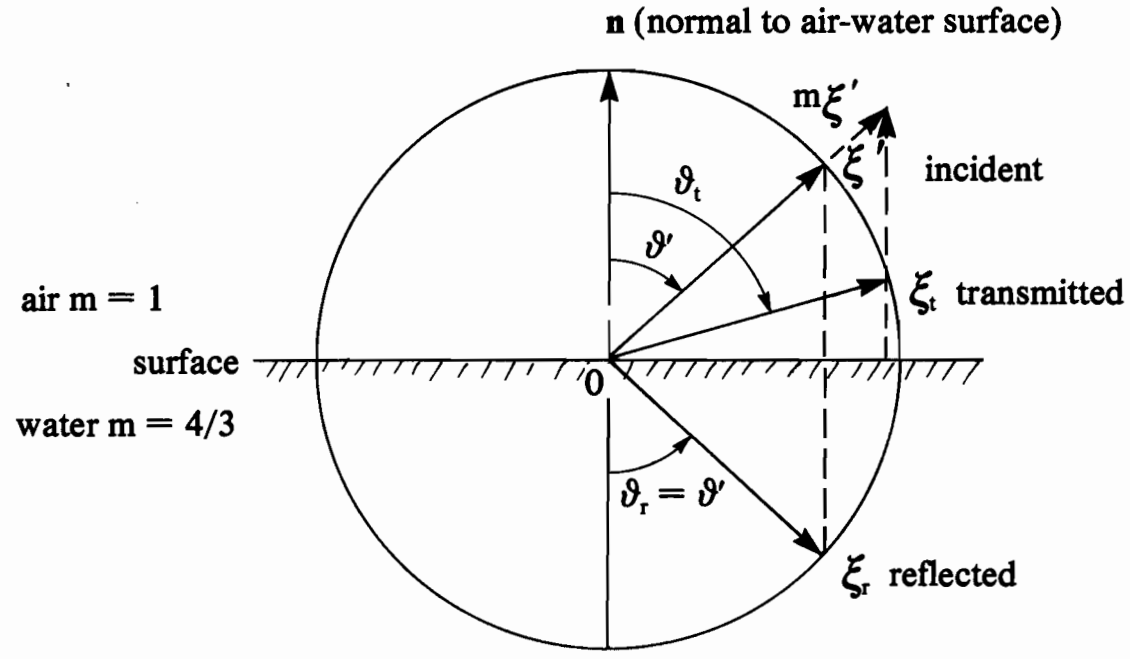

Figure 9.--Schematic diagrams for reflected and refracted rays. The diagrams are based on Snell's law of refraction and the law of reflection of rays. The top panel is for air-incident rays; the bottom panel is for water-incident rays. The dashed vertical lines connecting various vectors summarize the essence of the reflection and refraction laws of rays, as expressed in (3.18), (3.19).

these two cases. Write momentarily "m_a", "m_w" for the indexes of refraction of air and water. Further, write the acute angles between $\underset{\sim}{n}$ and the ray directions $\underset{\sim}{\xi}_a$ and $\underset{\sim}{\xi}_w$ in air and water as "ϑ_a", "ϑ_w" respectively. Then Snell's law states

$$m_a \sin\vartheta_a = m_w \sin\vartheta_w \ . \tag{3.17}$$

This form of the law holds regardless of the direction of approach of a ray to the air-water surface. Knowing m_a, m_w and one of the two angles ϑ_a, ϑ_w, the other can be found. The upper panel of Fig. 9 is the air-incident case and is obtained from (3.17) by setting* $m_a = 1$, $m = m_w = 4/3$, $\vartheta' = \vartheta_a$, $\vartheta_t = \vartheta_w$, with reflected ray angle $\vartheta_r = \vartheta'$. Therefore, given an incident direction $\underset{\sim}{\xi}'$ we have the following working formulas which can be read from the upper diagram of Fig. 9:

(air-incident case)

$$\begin{aligned}
&\underset{\sim}{\xi}_r \equiv \underset{\sim}{\xi}' - 2(\underset{\sim}{\xi}'\cdot\underset{\sim}{n})\underset{\sim}{n} \\
&\underset{\sim}{\xi}_t \equiv (\underset{\sim}{\xi}' - c\underset{\sim}{n})/m \ ; \ c = \underset{\sim}{n}\cdot\underset{\sim}{\xi}' - [(\underset{\sim}{\xi}'\cdot\underset{\sim}{n})^2 + m^2 - 1]^{\frac{1}{2}} \\
&\vartheta' \equiv \arccos|\underset{\sim}{\xi}'\cdot\underset{\sim}{n}| = \vartheta_r \\
&\vartheta_t \equiv \arcsin[m^{-1}\sin\vartheta'] \ .
\end{aligned} \tag{3.18}$$

* The index of refraction m_w of sea water, with salinity of 35 parts per thousand, at atmospheric pressure, and at 20°C, varies from 1.35 at light ray wavelength 400 nm to 1.34 at 700 nm. The variation of m_w with temperature, salinity and pressure is very mild. Therefore we may take m_w at its usual simple fractional value $m_w = 4/3 = 1.33$ as representative of m_w over the visible spectrum, for most practical applications of the present results. For a detailed study of m_w under a wide range of physical conditions, see Austin and Halikas (1976).

The lower panel of Fig. 9 is obtained from (3.17) by setting $m_a = 1$, $m = m_w = 4/3$, $\vartheta' = \vartheta_w$, $\vartheta_t = \vartheta_a$, with reflected ray angle $\vartheta_r = \vartheta'$. Therefore, given incident direction $\underset{\sim}{\xi}'$ we have the following formulas which may be read from the lower diagram of Fig. 9:

(water-incident case)

$$\begin{aligned} \underset{\sim}{\xi}_r &\equiv \underset{\sim}{\xi}' - 2(\underset{\sim}{\xi}'\cdot\underset{\sim}{n})\underset{\sim}{n} \\ \underset{\sim}{\xi}_t &\equiv m\underset{\sim}{\xi}' - c\underset{\sim}{n} \quad , \quad c = m\underset{\sim}{\xi}'\cdot\underset{\sim}{n} - [(m\underset{\sim}{\xi}'\cdot\underset{\sim}{n})^2 - m^2 + 1]^{\frac{1}{2}} \\ \vartheta' &\equiv \arccos|\underset{\sim}{\xi}'\cdot\underset{\sim}{n}| = \vartheta_r \\ \vartheta_t &\equiv \arcsin[m \sin\vartheta'] \ . \end{aligned} \tag{3.19}$$

The constant c in (3.18), (3.19) is fixed in each case by requiring $\underset{\sim}{\xi}_t$ to be a unit vector, given the unit vectors $\underset{\sim}{\xi}'$ and $\underset{\sim}{n}$. The choice of the minus sign before each square root is guided by physical reasoning and is made so as to have c approach zero as m approaches 1.

F. Fresnel reflectance formula

For either the air- or water-incident case in (3.18) or (3.19), the reflectance $r(\vartheta')$ of the air-water surface for unpolarized incident radiant flux is given by

$$r(\vartheta') \equiv r(\underset{\sim}{\xi}'\cdot\underset{\sim}{n}) \equiv \tfrac{1}{2}\left\{\left[\frac{\sin(\vartheta'-\vartheta_t)}{\sin(\vartheta'+\vartheta_t)}\right]^2 + \left[\frac{\tan(\vartheta'-\vartheta_t)}{\tan(\vartheta'+\vartheta_t)}\right]^2\right\}. \tag{3.20}$$

A derivation of the components of this formula may be found, for example, in Stratton (1941).

G. Radiant Flux conservation

The reflectance (3.20), as its derivation from Maxwell's equations shows, is basically that for unpolarized *irradiance* H watt/m^2 (in contrast to radiance) incident on the plane interface between two dielectric media of indexes of refraction m_a and m_w, with ϑ_t reckoned as in (3.18) or (3.19). For example, if H' is the incident irradiance (watt/m^2, in air or water) and H_r and H_t are the reflected and transmitted irradiances at the interface, then

$$H_r \equiv H' \, r(\underset{\sim}{\xi}' \cdot \underset{\sim}{n}) \tag{3.21}$$

$$H_t \equiv H' \, t(\underset{\sim}{\xi}' \cdot \underset{\sim}{n}) \, , \tag{3.22}$$

where

$$t(\underset{\sim}{\xi}' \cdot \underset{\sim}{n}) \equiv 1 - r(\underset{\sim}{\xi}' \cdot \underset{\sim}{n}) \tag{3.23}$$

and radiant flux conservation holds:

$$H' = H_r + H_t \, . \tag{3.24}$$

H. A ray pencil invariant

To derive the *radiance* reflectance and transmittance laws from (3.24) we use the following corollary of Snell's law (3.17):

$$m_a^2 \mu_a \Omega_a = m_w^2 \mu_w \Omega_w \tag{3.25}$$

where Ω_a and Ω_w are respectively the small solid angles of two refraction-related pencils of rays on the air and water sides of the air-water surface, and where $\mu_a = |\underset{\sim}{\xi}_a \cdot \underset{\sim}{n}|$ and $\mu_w = |\underset{\sim}{\xi}_w \cdot \underset{\sim}{n}|$. This relation is useful for deducing either Ω_a or Ω_w, knowing the other. It generally expresses the invariance of

the optical volume of a packet of photons along a pencil of rays as the packet traverses interfaces of optical media of different indexes of refraction (cf. Preisendorfer 1965, p. 37). The reflection process is simpler than the refraction process at an interface. There we have $\mu_a = \mu_w$ and $\Omega_a = \Omega_w$ for incident and reflected pencils of rays.

I. Radiance reflectance and transmittance laws.

Suppose N_a and N_w are the radiances of two refraction-related pencils of unpolarized light rays at the air-water interface. If the associated solid angles Ω_a, Ω_w and direction cosines μ_a, μ_w of these pencils are given, and if in (3.21)-(3.24) we set $\underset{\sim}{\xi}_a = \underset{\sim}{\xi}'$, $H_a = H'$ and $H_w = H_t$, as required in the air-incident case, then

$$H_r = H_a r(\underset{\sim}{\xi}' \cdot \underset{\sim}{n}) = N_a \mu_a \Omega_a \; r(\underset{\sim}{\xi}_a \cdot \underset{\sim}{n})$$
$$H_t = H_a t(\underset{\sim}{\xi}' \cdot \underset{\sim}{n}) = N_a \mu_a \Omega_a \; t(\underset{\sim}{\xi}_a \cdot \underset{\sim}{n}) \; .$$

The radiant flux conservation statement (3.24) becomes

$$H_a = N_a \mu_a \Omega_a = N_a \mu_a \Omega_a \; r(\underset{\sim}{\xi}_a \cdot \underset{\sim}{n}) + N_a \mu_a \Omega_a \; t(\underset{\sim}{\xi}_a \cdot \underset{\sim}{n}) \; . \tag{3.26}$$

Replacing $\mu_a \Omega_a$ in the transmission term of (3.26) by means of (3.25), we find

$$N_a \mu_a \Omega_a = N_a \mu_a \Omega_a \; r(\underset{\sim}{\xi}_a \cdot \underset{\sim}{n}) + [N_a (\frac{m_w^2}{m_a^2}) \; t(\underset{\sim}{\xi}_a \cdot \underset{\sim}{n})] \; \mu_w \Omega_w \; . \tag{3.27}$$

A study of the transmission term in (3.27) suggests that we define the transmitted radiance as

$$N_w \equiv N_a \left(\frac{m_w^2}{m_a^2}\right) t(\underset{\sim}{\xi}_a \cdot \underset{\sim}{n}) \tag{3.28}$$

which is the desired *radiance transmittance law for the air-incident case.* Interchanging "a" and "w" in (3.28) yields the corresponding *radiance transmittance law for the water-incident case*:

$$N_a \equiv N_w \left(\frac{m_a^2}{m_w^2}\right) t(\underset{\sim}{\xi}_w \cdot \underset{\sim}{n}) \ . \tag{3.29}$$

The reflectance term in (3.27) and our observation in paragraph H show how radiance is reflected, i.e., we have simply $N_r = N_a r(\underset{\sim}{\xi}_a \cdot \underset{\sim}{n})$.

In summary then, on setting $m_a = 1$ and $m_w \equiv m = 4/3$ and writing "$\underset{\sim}{\xi}$'" for $\underset{\sim}{\xi}_a$ or $\underset{\sim}{\xi}_w$ and writing "N'" for N_a or N_w, as the case may be, we find, in the notation of (3.18) and (3.19), the radiance reflectance and transmittance laws at the air-water interface:

$$N_r = N' r(\underset{\sim}{\xi}' \cdot \underset{\sim}{n}) \qquad \text{(reflectance; for air- or water-incidence)} \tag{3.30}$$

and

$$N_t = N' m^2 t(\underset{\sim}{\xi}' \cdot \underset{\sim}{n}) \qquad \text{(air-incident case)} \tag{3.31a}$$

$$N_t = N' m^{-2} t(\underset{\sim}{\xi}' \cdot \underset{\sim}{n}) \ . \qquad \text{(water-incident case)} \tag{3.31b}$$

In the present work we will make use only of (3.21) and (3.22) as our basic laws of reflection and refraction on the irradiance--and hence the radiant flux level. The purpose of introducing the laws (3.30)-(3.31) was to show that (3.21) and (3.22) are consistent with these more detailed *radiance* reflectance and transmittance laws.

4. *Defining Reflectances*

Let $S(\omega)$ be the ωth realization of a random capillary wave surface S over the hexagonal domain, $\omega = 1,\ldots,r$. Thus $S = \{S(\omega): \omega = 1,\ldots,r\}$, and is constructed as in section 2. The surface $S(\omega)$ can in principle be extended to infinity in all horizontal directions of the hexagonally partitioned plane of Fig. 1. The latter plane serves as a mean water surface about which the facets of $S(\omega)$ are randomly placed. Parallel to this mean horizontal surface, and just above and below $S(\omega)$ at fixed distances, are two *horizontal monitoring surfaces* (h.m.s.), which we will use in the derivations below. We now consider two specific examples of how to compute the reflectance of $S(\omega)$ to downward radiant flux. On the basis of these examples we can then describe the general recurrence formulas for the reflected and transmitted radiant fluxes P_r and P_t needed in steps 6 and 7 of the ray tracing flow diagram of Fig. 2.

A. Example of a simple ray path.

A narrow pencil of unpolarized rays of central direction $\underset{\sim}{\xi}'$ is incident on $S(\omega)$ at point B, as shown in Fig. 1. A close up of this is shown in the upper panel of Fig. 10. The pencil illumines a small patch A of outward normal $\underset{\sim}{n}$ on $S(\omega)$. To define the reflectance of $S(\omega)$ when the surface is highly crinkled, we place an h.m.s. just above $S(\omega)$, as shown. We use the h.m.s. to register the incident radiant flux P(I) of the pencil as it crosses a small patch I of the h.m.s. on its way to A on $S(\omega)$. Clearly $P(A) = P(I)$. Now in accordance with (3.21) a fraction $r(\underset{\sim}{\xi}'\cdot\underset{\sim}{n})$ of P(A) is reflected into the direction $\underset{\sim}{\xi}$ and then streams upward through patch R of the h.m.s. If P(R) is the radiant flux of the reflected pencil crossing R, then $P(R) = P(A)r(\underset{\sim}{\xi}'\cdot\underset{\sim}{n}) = P(I)r(\underset{\sim}{\xi}'\cdot\underset{\sim}{n})$.

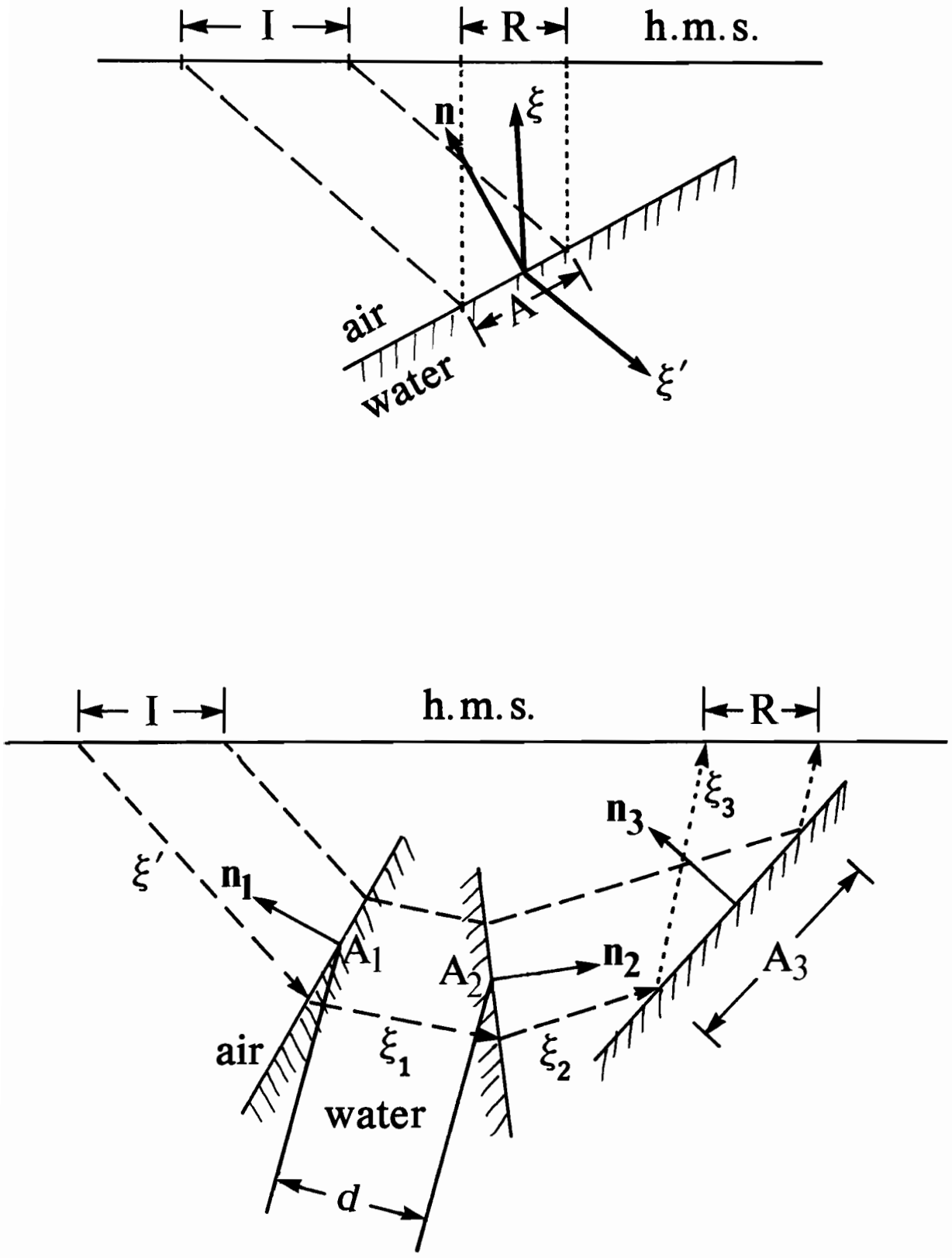

Figure 10.--Illustrating the use of the horizontal monitoring surface (h.m.s.) for single scattering (upper) and multiple scattering (lower).

The *albedo* or *irradiance reflectance* $r_{-}(\underset{\sim}{\xi}')$ (or $r_{-}(\underset{\sim}{\xi}';\omega)$) of $S(\omega)$ relative to this particular pencil is by definition

$$r_{-}(\xi') \equiv P(R)/P(I) = r(\underset{\sim}{\xi}'\cdot\underset{\sim}{n}) \ . \tag{4.1}$$

The irradiance transmittance $t(\underset{\sim}{\xi}')$ of $S(\omega)$ is then

$$t_{-}(\xi') \equiv 1 - r_{-}(\underset{\sim}{\xi}') \ . \tag{4.2}$$

B. Example of a complex ray path.

The preceding ideas may be extended to more complicated paths over $S(\omega)$. In the lower panel of Fig. 10 an incident pencil of rays of unpolarized radiant flux P(I) crosses the h.m.s. and illumines a small patch A_1 with outward normal $\underset{\sim}{n}_1$, whereupon a refracted daughter pencil of rays is born and travels along direction $\underset{\sim}{\xi}_1$ a distance d underwater to encounter patch A_2 of outward normal $\underset{\sim}{n}_2$, there to be partially refracted into a new daughter ray along $\underset{\sim}{\xi}_2$. The final encounter of this particular ray bundle with the water surface is over patch A_3 with outward normal $\underset{\sim}{n}_3$, from which the flux of a new daughter ray bundle proceeds along $\underset{\sim}{\xi}_3$ toward the h.m.s. and emerges through patch R carrying radiant flux P(R). The ratio of this emergent flux P(R) to the incident flux P(I), i.e., the albedo of $S(\omega)$ in this path instance, is

$$r_{-}(\underset{\sim}{\xi}') = P(R)/P(I) = t(\underset{\sim}{\xi}'\cdot\underset{\sim}{n}_1)\ \exp[-\alpha d]\ t(\underset{\sim}{\xi}_1\cdot\underset{\sim}{n}_2)\ r(\underset{\sim}{\xi}_2\cdot\underset{\sim}{n}_3) \ . \tag{4.3}$$

The exponential factor, for the underwater path segment of distance d, accounts for the flux lost from the daughter bundle, due to absorption and

scattering, as the bundle travels from patch A_1 to A_2. α is the *volume attenuation coefficient* for the water. The other factors are Fresnel factors and are understood in the same way as those in (4.1) and (4.2). Here we have, e.g., $t(\underset{\sim}{\xi}'\cdot\underset{\sim}{n}_1) = 1 - r(\underset{\sim}{\xi}'\cdot\underset{\sim}{n}_1)$, where $r(\underset{\sim}{\xi}'\cdot\underset{\sim}{n}_1)$ is as defined in (3.18). In our numerical studies of the present method we experiment with various choices of α in the transmission factor $\exp[-\alpha d]$. Setting $\alpha = 0$ in effect makes the water transparent. Setting $\alpha = \infty$ in effect eliminates any multiple scattering effects arising from subsurface travels of daughter rays. The true $r_-(\underset{\sim}{\xi}')$ (after a full run as described in Fig. 2) will lie somewhere between the two values governed by these limiting cases.

C. The general recursive ray path.

When we turn to find the general form of (4.1) and (4.3) we see at first a bewildering number of possible daughter paths that can spring from a single incident ray approaching $S(\omega)$ along a direction $\underset{\sim}{\xi}'$. Figure 11 shows some of these possibilities. We can classify these possibilities by counting the number n_s of scattering points and the number n_b of branches into which the original ray splits. For air-incident rays, the three-branch, single scattering event shown in Fig. 11 is by far the most common at all wind speeds and angles of incidence. As the wind speed increases, or if incident rays come in nearly horizontal, then the numbers of scatters and branches increase. For water-incident rays single scattering events are also most common. Figure 11 shows how these single scattering events consist of two kinds: the case of $n_s = 1$, $n_b = 2$ when total internal scattering occurs and the case of $n_s = 1$, $n_b = 3$ when an upward transmitted ray occurs. For crinkly surfaces, water-incident rays can undergo multiple scattering ($n_s \geq 2$), as indicated in the $n_s = 2$, $n_b = 4$ case of Fig. 11. Of the many possible

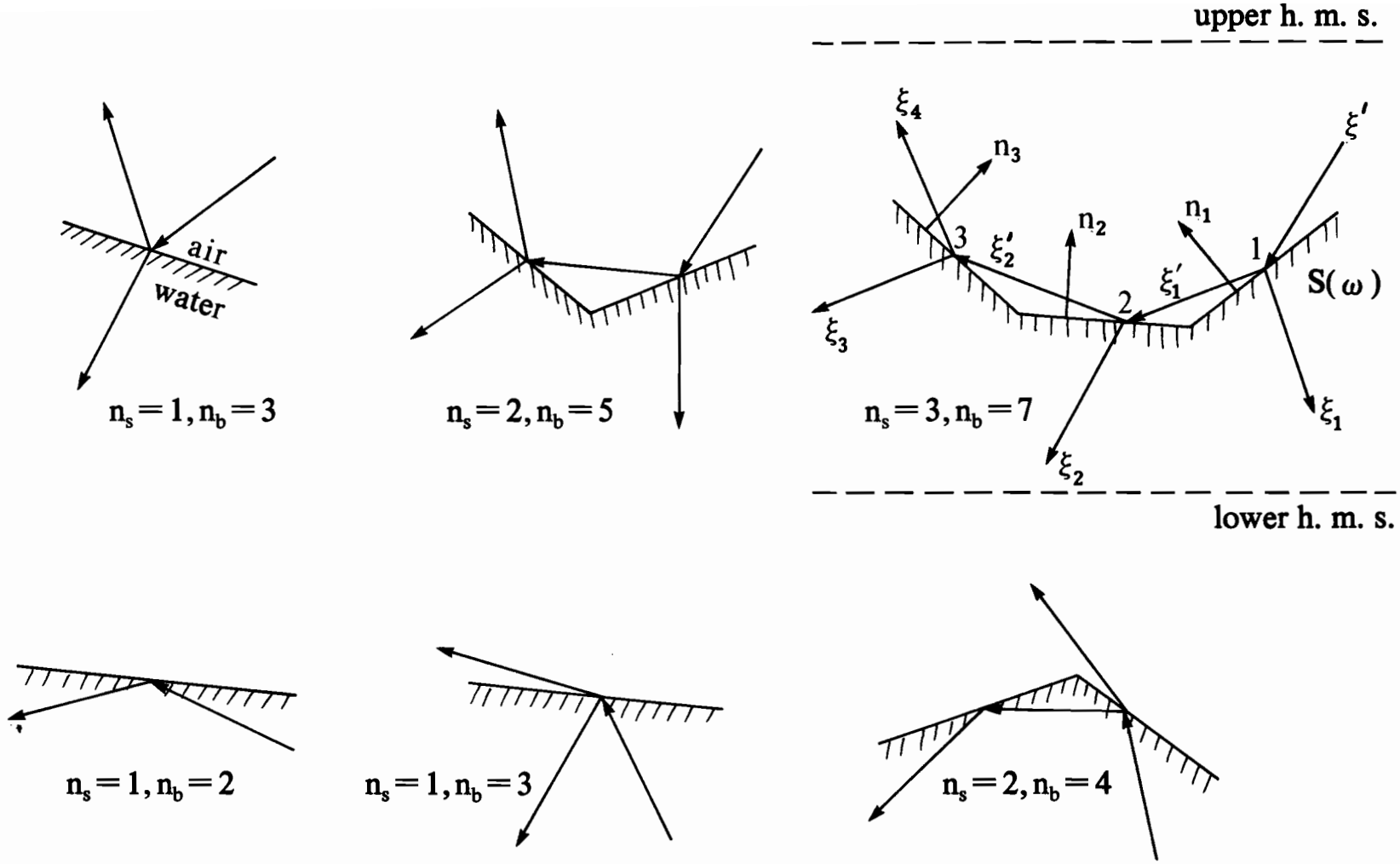

Figure 11.--Schematic diagrams of common scattering events. The top row is for the air-incident case; the bottom row is for the water-incident case. n_s counts the number of ray-surface encounters, n_b the total number of parent and daughter rays (branches).

configurations for air-incident multiple scattering, the second-order scatter, five-branch case is the most common with third-order scatter, seven-branch cases being the next most common. In the numerical studies to be described below, configurations such as $n_s = 3$, $n_b = 6$ (the case shown in Fig. 1) are rare; and cases where $n_b \geq 10$ almost never occur. While it is possible to develop an algebraic notation to explicitly represent the general forms of (4.1) or (4.3), it is more expedient for our numerical work to simply write down a recursive formula for the radiant flux content of a newly born daughter ray at each step between the beginning and end of the parent ray's travels; and so we proceed as follows.

Suppose the numerical computation is at step (5) of the ray tracing procedure of Fig. 2. We then know the values of $\underset{\sim}{\xi}$, $\underset{\sim}{p}$ and P defining the parent ray. Tracing the ray from $\underset{\sim}{p}$ to an interception point $\underset{\sim}{p}_i$ along $\underset{\sim}{\xi}$ yields a calculable distance $d = \|\underset{\sim}{p} - \underset{\sim}{p}_i\|$. The outward normal $\underset{\sim}{n}_i$ to $S(\omega)$ at $\underset{\sim}{p}_i$ is known from the formulas of section 3D. From $\underset{\sim}{n}_i$ we can decide whether the path of the ray was in air or water by finding whether $\underset{\sim}{\xi}\cdot\underset{\sim}{n}_i \leq 0$ (air-incident case) or $\underset{\sim}{\xi}\cdot\underset{\sim}{n}_i > 0$ (water-incident case). The daughter ray directions $\underset{\sim}{\xi}_r$ and $\underset{\sim}{\xi}_t$ at $\underset{\sim}{p}_i$ are then found as in section 3E. In the *air-incident case* the generated daughter rays are defined by

$$(\underset{\sim}{\xi}_r, \underset{\sim}{p}_i, P_r) \text{ , with } P_r = Pr(\underset{\sim}{\xi}\cdot\underset{\sim}{n}_i) \text{ , for the reflected ray}$$

and (4.4)

$$(\underset{\sim}{\xi}_t, \underset{\sim}{p}_i, P_t) \text{ , with } P_t = Pt(\underset{\sim}{\xi}\cdot\underset{\sim}{n}_i) \text{ , for the refracted ray,}$$

where P is modified according to (3.21) or (3.22), and $t(\underset{\sim}{\xi}\cdot\underset{\sim}{n}_i) \equiv 1 - r(\underset{\sim}{\xi}\cdot\underset{\sim}{n}_i)$. In the water-incident case the daughter rays are defined in a similar way:

$$(\underset{\sim}{\xi}_r, \underset{\sim}{p}_i, P_r) \text{ , with } P_r = P \exp[-\alpha d] r(\underset{\sim}{\xi}\cdot\underset{\sim}{n}_i) \text{ for the reflected ray}$$

and (4.5)

$$(\underset{\sim}{\xi}_t, \underset{\sim}{p}_i, P_t) \text{ , with } P_t = P \exp[-\alpha d] t(\underset{\sim}{\xi}\cdot\underset{\sim}{n}_i) \text{ for the refracted ray}$$

where the new fluxes are defined via (3.21) or (3.22). To account for flux lost from the ray during water transmission, we include $\exp[-\alpha d]$. As before, $t(\underset{\sim}{\xi}\cdot\underset{\sim}{n}_i) \equiv 1 - r(\underset{\sim}{\xi}\cdot\underset{\sim}{n}_i)$. In the case of total internal reflection, $r(\underset{\sim}{\xi}\cdot\underset{\sim}{n}_i) = 1$ so that there is no refracted ray. The daughter ray triples defined by (4.4) and (4.5) are immediately pushed into the stack for subsequent processing, as described in steps (6) and (7) of Fig. 2.

D. Using the result

The result of the calculations above, in the context of Fig. 2, i.e. after ensemble averaging has been done, is a number $r_-(\underset{\sim}{\xi}')$, say, for an unpolarized ray pencil directed downward at a random surface over which wind is moving at speed U. One uses this number in practice as follows. Let a pencil of rays of radiance $N(\underset{\sim}{\xi}')$ be incident on such a surface at each point of its upper h.m.s. (cf. Fig. 10 or 11). Let $\Delta\Omega$ be the (small) solid angle of the pencil. Then $N(\underset{\sim}{\xi}')|\underset{\sim}{\xi}'\cdot\underset{\sim}{k}|\Delta\Omega$ is the irradiance (watt/m^2) incident at each point of the h.m.s. of the air-water surface. Further, by construction of $r_-(\underset{\sim}{\xi}')$, $N(\underset{\sim}{\xi}')|\underset{\sim}{\xi}'\cdot\underset{\sim}{k}|\, r_-(\underset{\sim}{\xi}')\Delta\Omega$ is the radiant emittance (outward-directed irradiance) of the upper h.m.s. and $N(\underset{\sim}{\xi}')|\underset{\sim}{\xi}'\cdot\underset{\sim}{k}|\, t_-(\underset{\sim}{\xi}')\Delta\Omega$ is the radiant emittance of the lower h.m.s. of the air-water surface (cf. Fig. 11). Since the random air-water surface is on average flat and horizontal, we may, in practice, let the upper and lower horizontal monitoring surfaces approach this flat average surface, and coalesce with it. Hence in practice $r_\pm(\underset{\sim}{\xi}')$ and $t_\pm(\underset{\sim}{\xi}')$ may be associated with the mean horizontal surface of a wind roughened sea.

E. Remarks on the derivation

It should be noted that a *single* number such as $r_-(\underset{\sim}{\xi}';\omega)$, found in (4.1) or (4.3) by tracing a single pencil of rays, is meaningless, statistically speaking. It is only after several thousands of such reflection numbers have been accumulated, and then averaged over ω, that a statistically meaningful result begins to emerge. Thus imagine these reflections to occur independently and in great numbers over the extent of the hexagonal grid for a single realization $S(\omega)$ of the surface. For a sufficiently large number of reflections, the ratio of the total amount of reflected radiant flux from a small neighborhood about each point of the horizontal monitoring surface for $S(\omega)$ to that incident upon the neighborhood will approach a limit, the desired albedo, or irradiance reflectance. This limit will in principle be independent of location of the neighborhood on the h.m.s. and will be a weighted average of terms of the kind in (4.1) and (4.3) and others built up by means of (4.4) and (4.5). By ergodic equivalence, this argument will also go through by applying it to an ensemble of realized surfaces $S(\omega)$ irradiated over a small neighborhood about a fixed common point of their grid. A simple argument towards this end, using radiometric concepts, will now be sketched. It also provides the basis for the interpretations of $r_-(\underset{\sim}{\xi}')$ in paragraph 4D. It is an heuristic argument that may be elaborated into a rigorous derivation of $r_-(\underset{\sim}{\xi}')$.

Let P(I) be the downward incident radiant flux over patch I of the upper h.m.s. of a realization $S(\omega)$ of the random water surface (as in the diagrams of Fig. 10). This P(I) is produced by a pencil of rays of radiance $N(\underset{\sim}{\xi}')$ about direction $\underset{\sim}{\xi}'$. If $\Delta\Omega$ and ΔA are the solid angle and the area of the pencil normal to $\underset{\sim}{\xi}'$, then

$$P(I) = N(\underset{\sim}{\xi}')\Delta\Omega\Delta A \tag{4.6}$$

where $\underset{\sim}{k}$ is the unit outward normal to the h.m.s.

If $r_-(\underset{\sim}{\xi}';\omega)$ is the facet reflectance associated with one of the daughter rays initiated by this parent ray (in the form of (4.1), (4.3), etc.) then the associated upward emergent flux $P(R;\omega)$ through the upper h.m.s. of $S(\omega)$ is given by

$$\begin{aligned} P(R;\omega) &= P(I)\ r_-(\underset{\sim}{\xi}';\omega) \\ &= N(\underset{\sim}{\xi}')\Delta\Omega\Delta A\ r_-(\underset{\sim}{\xi}';\underset{\sim}{\omega}) \end{aligned} \tag{4.7}$$

Taking the ensemble average of each side over all realizations $S(\omega)$ we find, on rearranging and inserting the factor $|\underset{\sim}{\xi}'\cdot\underset{\sim}{k}|$, that

$$r_-(\underset{\sim}{\xi}') \equiv \frac{\underset{\omega}{E}\ P(R;\omega)/[\Delta A/|\underset{\sim}{\xi}'\cdot\underset{\sim}{k}|]}{N(\underset{\sim}{\xi}')\Delta\Omega\ |\underset{\sim}{\xi}'\cdot\underset{\sim}{k}|} = \underset{\omega}{E}\ r_-(\underset{\sim}{\xi}';\omega) \tag{4.8}$$

Here $\Delta A/|\underset{\sim}{\xi}'\cdot\underset{\sim}{k}|$ is the area of illuminated patch I which we may assign to the ensemble average of $P(R;\omega)$. Thus we see that the numerator of $r_-(\underset{\sim}{\xi}')$ in (4.8) is an average radiant emittance (watt/m^2) of the h.m.s. while the denominator is the irradiance (watt/m^2) on the h.m.s. The value of $r_-(\underset{\sim}{\xi}')$ in (4.8) is found in practice, as outlined in steps 8 and 9 of Fig. 2. This practical procedure gives the meaning of the ensemble average over all ω (= 1,...,r) on the right in (4.8), and in turn, (4.8) shows the theoretical basis of steps 8-11 and 9 of Fig. 2.

5. *Stacking Rays*

The ray stacking activity, i.e., the handling of the ray triples $(\underset{\sim}{\xi},\underset{\sim}{p},P)$, forms an integral part of the sequence of ray tracing steps in Fig. 2. In the computer program the stack S is a 10 × 7 array capable of storing 10 ordered septuples of the form

$$(\xi_1,\xi_2,\xi_3,p_1,p_2,p_3,P) \equiv (\underset{\sim}{\xi},\underset{\sim}{p},P) \ . \tag{5.1}$$

The NSth, or last, row of S, $\underset{\sim}{S}(NS) = \{S(NS,K): K = 1,\ldots,7\}$, is defined as

$$\begin{aligned} S(NS,1) &= \xi_1 \\ S(NS,2) &= \xi_2 \qquad NS \le 10, \\ &\vdots \\ S(NS,7) &= P \ . \end{aligned} \tag{5.2}$$

This constructs the ray triple $(\underset{\sim}{\xi},\underset{\sim}{p},P)$ of S using the geometric information $\underset{\sim}{\xi},\underset{\sim}{p}$ along with P. When the ray tracing procedure has just constructed a new surface as in step 2 of Fig. 2, we initialize the array S in step 3 by placing (i.e., *pushing*) $\underset{\sim}{S}(1) = (\underset{\sim}{\xi}',\underset{\sim}{p}',P')$ into S using the identifications in (5.2), and setting the *array counter* NS to 1. (At the outset of the program, set NS = 0 since no rays are in the stack.) In the general activity of step 4 we *pull* the general NSth (i.e., the last) row $\underset{\sim}{S}(NS)$ from S by reversing the FORTRAN identifications in (5.2):

$$\begin{aligned} \xi_1 &= S(NS,1) \\ \xi_2 &= S(NS,2) \qquad NS \le 10, \\ &\vdots \\ P &= S(NS,7)\ . \end{aligned} \tag{5.3}$$

This results in the ray triple $(\underset{\sim}{\xi},\underset{\sim}{p},P)$ ready for further processing in step 5. After this pull is completed the array counter NS is set to NS-1. In summary, a *push* (in step 3, 6, or 7) consists of noting the value of the array counter NS, forming anew the NS + 1 (the new last) row of S via (5.2), and updating NS to NS + 1. A *pull* (in step 4) consists of going to the last (i.e., the NSth) row of S, forming a triple $(\underset{\sim}{\xi},\underset{\sim}{p},P)$ via (5.3), and updating the array counter NS to NS - 1 (to expose a new last row of S).

When step 9 of Fig. 2 finds a value of NS = 0, the parent ray and all of its daughters have been traced to completion.

6. *Model characteristics*

There are several features of the ray tracing procedure that may be of interest to a reader should he attempt to code the procedure by himself.

A. Computer code optimization

Initial runs with capillary waves constructed over a hexagonal grid showed that almost all of the computational expense involved checking the triads, one by one, to see if the ray had intercepted the associated facet. Considerable computational savings result from the following observation. As a random surface realization is generated, the maximum and minimum node elevations are recorded respectively above and below the hexagonal grid. This determines a *vertical range* of surface elevations. Only when a ray is within this vertical range of the realized surface does a check for interception of the surface need to be made. For example, if a ray is incident from near the zenith, its track may cross many triads of the hexagonal grid before the ray is near the surface, i.e., within the above-defined vertical range. In such a case it often turns out that after the ray has dipped into the vertical range only one or two triads near the center of the hexagon need to be checked before a facet interception is found. Likewise, if a daughter ray leaves the surface in an upward or downward direction, no further checks need to be made after the outgoing ray leaves the vertical range of the realized surface, even though the track may thereafter cross many triads before the hexagonal grid's boundary is reached.

It sometimes happens that a daughter ray passing through the air in a downward direction, or through the water in an upward direction, leaves the hexagonal domain before interacting with the surface. With the bookkeeping procedure adopted in this study, such a ray is improperly tallied, since it

would intercept the surface again at some point outside the hexagon and hence outside the tallying area. By choosing the order of the hexagon sufficiently large, the number of such lost rays can be made arbitrarily small. In practice with capillary waves, a grid of order n = 7 with a target point near the center is sufficiently large to keep the number of lost rays to one per several thousand incident rays.

Certain other singular cases can occur. For example, a daughter ray traveling exactly straight up or down would never leave the hexagonal domain. Such special situations seldom if ever occur in practice, although the computer code must check for them in order to prevent the possibility of division by zero or infinite loops.

To trace one ray from start to finish, the carefully optimized computer code requires on average about 0.004 seconds of execution time on a CDC CYBER 170/750 computer. The program keeps a tally of the numbers of lost rays and multiply-scattered rays so that accuracy checks and comparisons of the relative contributions of single and multiple scattering can be made. Extensive direct and indirect checks have been made to guarantee the correctness of the present computer code. Several of these checks will be discussed at appropriate points below.

B. Multiple scattering

A phenomenon which is difficult to handle in analytic formulations, but nearly trivial in the present numerical study, is that of multiple scattering. In Fig. 11 we define the order n_s of scattering as the total number of times a parent ray or any of its daughter rays intercepts the wave surface.

Figure 12 shows the dependence of the multiple scattering index n_s on wind speed and angle of incidence of the parent light rays. For purposes of labeling graphs such as Fig. 12, it is often convenient to define the incident angle θ_s' as the acute angle between the ray and either the $+\underset{\sim}{k}$ (zenith) direction or the $-\underset{\sim}{k}$ (nadir) direction (see Fig. 4). Then $0 \leq \theta_s' \leq 90°$ and the phrase "air-incident rays" or "water-incident rays" must be added to avoid ambiguity. Figure 12 shows, as a function of θ_s' and wind speed, the percentage of incoming rays which undergo multiple scattering of any order ($n_s \geq 2$). This figure is for incoming rays which are parallel to the wind ($\phi_s' = 0$ in Fig. 4). The figure is based on over 150,000 ray tracings. The curves are applicable to both air-incident and water-incident rays. Observe that, for a given incidence angle θ_s', the percentage of rays undergoing multiple scattering generally increases with wind speed U (except for the incident angle range between 80° and 90°). Rays incident from within 30° of the zenith or from a similar cone near the nadir almost never have multiple scatters for winds in the range U = 0 to 20 m/s. We see that for wind speed $U \geq 5$ m/s, typically five to ten percent of the rays incident from the range $60° \leq \theta_s' \leq 80°$ have multiple scatters. This is because the relative angles between the tilted wave facets and the incident rays are then most conducive to reflecting the incident ray into a nearly horizontal direction, so that the reflected daughter ray hits a neighboring facet. There is an overall dropoff in multiple scattering for nearly horizontal (80°) incoming rays, since the daughter rays then tend to head away from the surface at angles which cause them on average to miss even the nearest facets. We note as a general rule that around 10% of the rays undergo multiple scattering by capillary waves, over a wide range of incident angles and wind speeds. The quantitative effects of multiple scattering will be discussed at appropriate locations below.

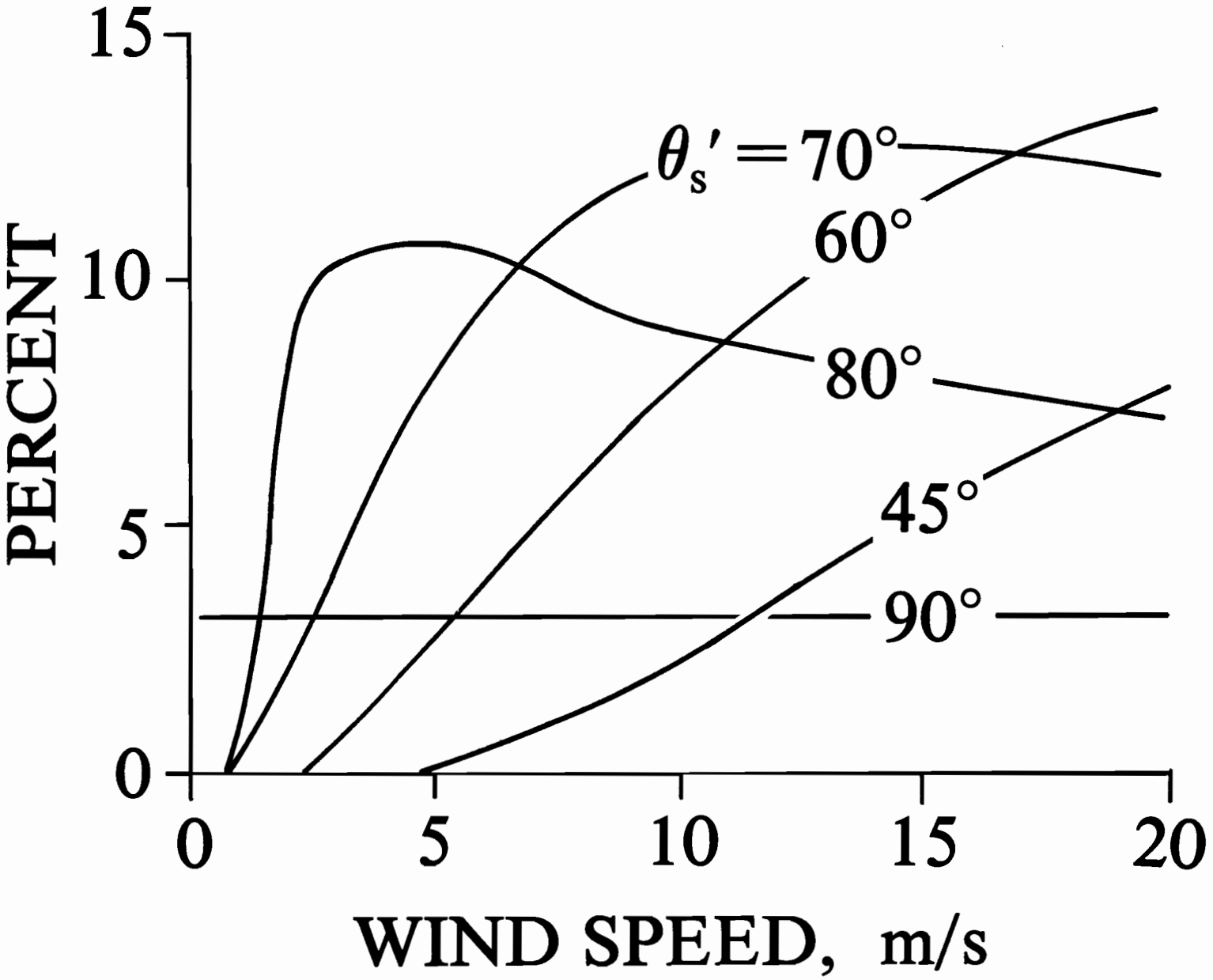

Figure 12.--The percentage of incident rays, as a function of wind speed, which undergo multiple scattering, for capillary waves with incident rays parallel to the wind ($\phi_s' = 180°$).

Additional experience with the model's behavior for capillary waves can be obtained from Fig. 13, which plots the average tilt $\bar{\beta}$ of the wave facet's unit normal $\underset{\sim}{n}$ from the vertical $\underset{\sim}{k}$. The tilt of a given facet is $\beta = \arccos(\underset{\sim}{n}\cdot\underset{\sim}{k})$. We see that the increase of the average tilt for capillary wave facets as a function of wind speed is qualitatively consistent with the curves of Fig. 12 and the comments of the preceding paragraph.

The area of a capillaried, wind-blown water surface relative to that of a calm sea may be estimated from Fig. 13. An element of area on a tilted wave facet is just $\sec\beta$ times the area of a triad. Computing $\sec\bar{\beta}$ from Fig. 13 and plotting as a function of U reveals a linear increase in the water surface area as a function of wind speed U (m/s), namely

$$\text{Relative surface area} = 1.0 + 0.0024U, \qquad 0 \le U \le 20 \text{ m/s} . \tag{6.1}$$

This model-derived fact is numerically consistent with a simple theoretical demonstration based on the empirical σ_u^2 and σ_c^2 laws in (2.1) (with p = 1) and the approximate trigonometric relation $\sec\beta \cong 1 + \frac{1}{2}\tan^2\beta$, for small β. Thus,

$$\begin{aligned} E[\sec\beta] &= E[1 + \tan^2\beta]^{\frac{1}{2}} \simeq E[1 + \tfrac{1}{2}\tan^2\beta] \\ &= 1 + \tfrac{1}{2}E[\zeta_u^2 + \zeta_c^2] = 1 + \tfrac{1}{2}(a_u + a_c)U = 1 + 0.0025U. \end{aligned} \tag{6.2}$$

In this derivation we have used the definitions of σ_u^2 and σ_c^2 (cf. (2.5)) and the geometric fact that

$$\tan^2\beta = \zeta_u^2 + \zeta_c^2 .$$

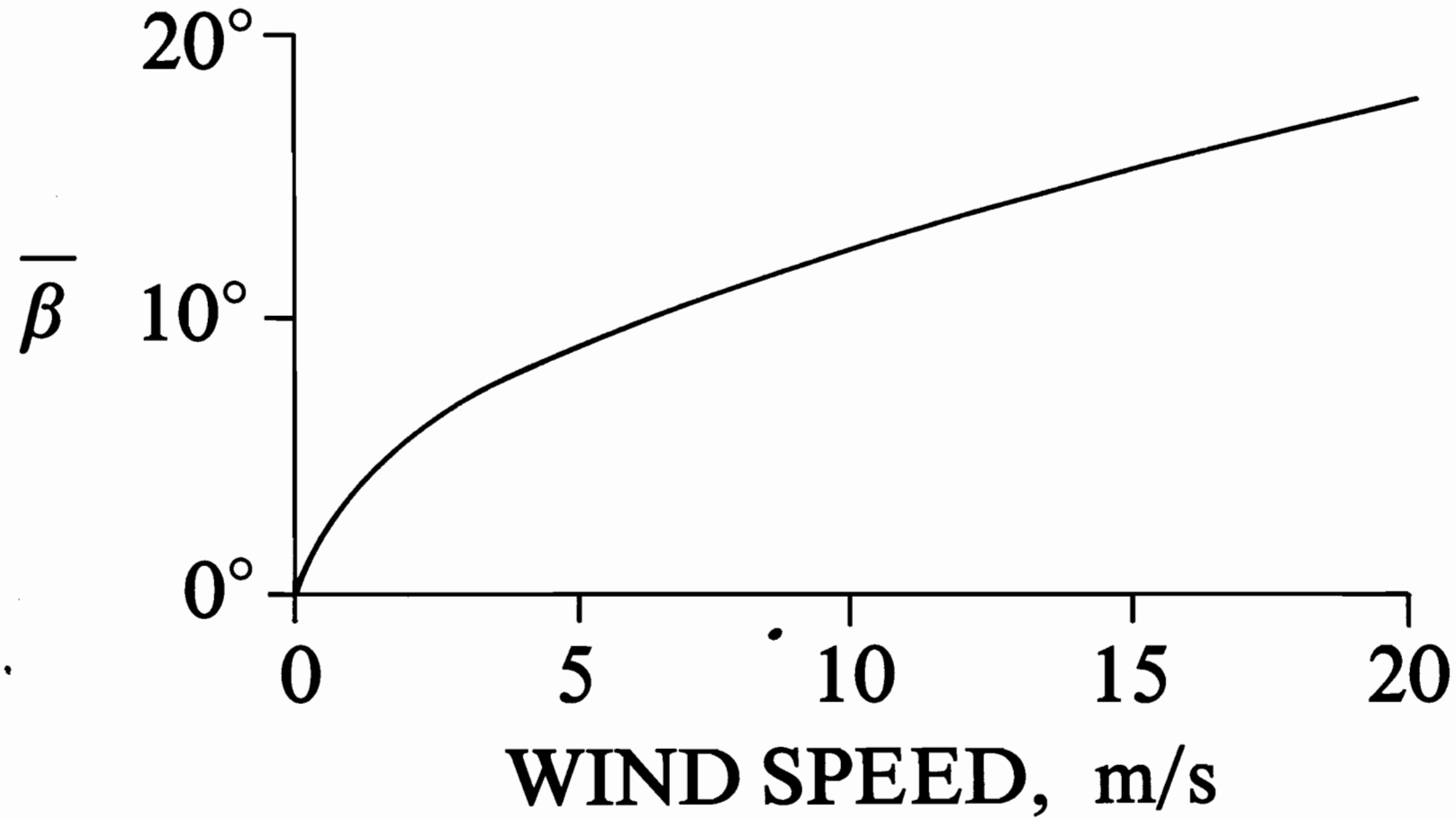

Figure 13.--The average tilt $\bar{\beta}$ of the wave facet normals from the vertical as a function of wind speed.

7. *Glitter patterns*

We are now prepared to discuss a central topic of our investigations: the generation and analysis of sea surface glitter patterns. The sun's glitter pattern on the sea surface has long been used as a tool for deducing the slope statistics of the sea surface. Important works in this area are those of Cox and Munk (op. cit.). In the present paper the sea surface statistics are assumed given, and the glitter pattern is generated by direct ray tracing on a set of sea surface realizations.

The generation of glitter patterns in this study serves two purposes. First, the comparison of model-generated glitter patterns with photographs of actual patterns serves as a partial check on the correctness of the ray-tracing model. Checks such as these give us confidence in the model's ability to determine the irradiance reflectances reported on in the next section of this study. Second, the model's ability to trace both reflected and refracted rays from light sources above and below the surface permits examinations of patterns which would be difficult to conduct experimentally, e.g. the glitter patterns of underwater light sources as seen from above or below the surface.

A. Coordinate systems

We develop our coordinate system following the usual manner of recording the sun's glitter pattern on the ocean surface, as shown in Fig. 14. An observer in an aircraft or generally at some remote point P aims a camera at the glitter pattern on the water surface and takes a photograph. The photograph is usually developed so that it has the horizon toward the top and the nadir toward the bottom. Stating the camera's viewing angle (field of view) gives the viewer of the photograph a feeling for the angular extent of

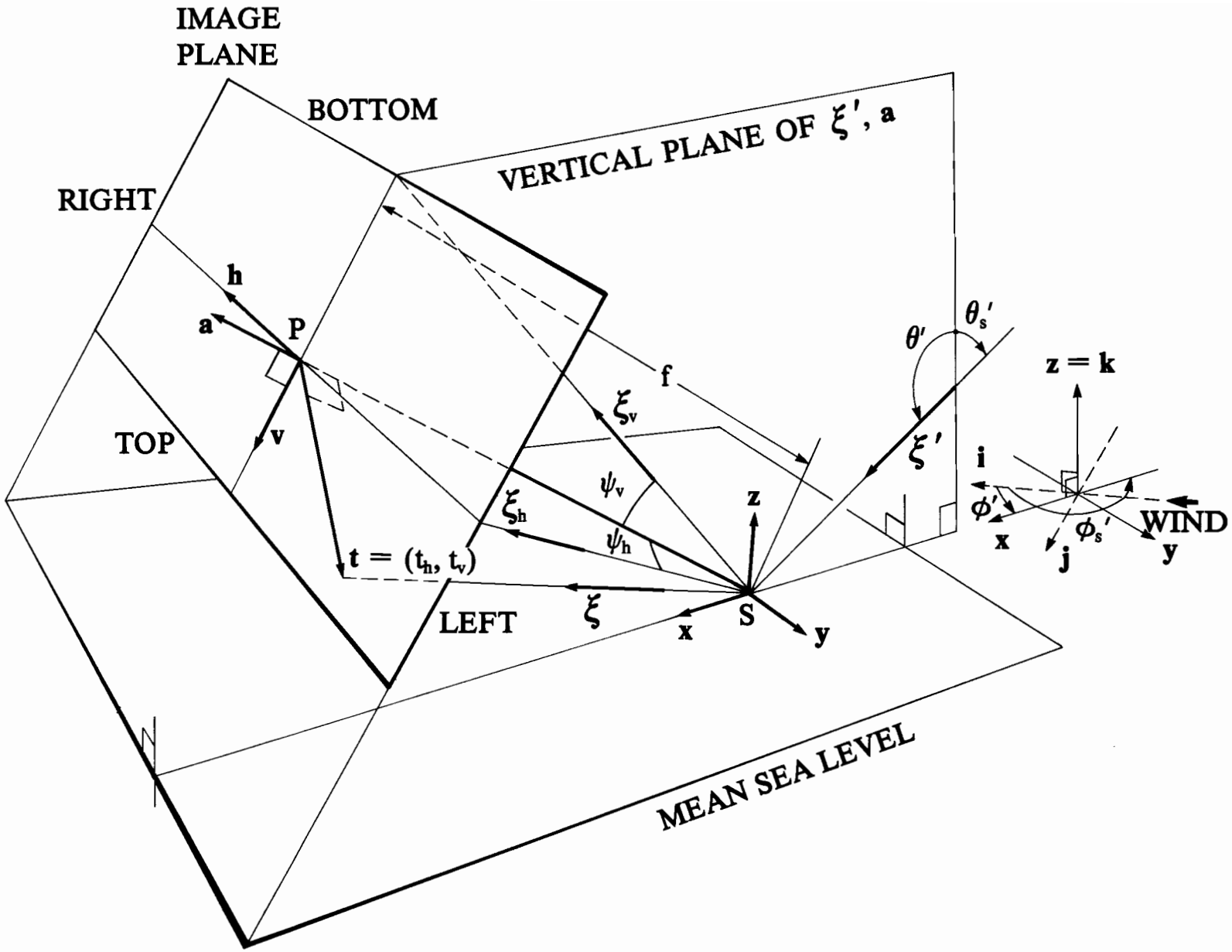

Figure 14.--Sun-based $\tilde{x}$-$\tilde{y}$-$\tilde{z}$ coordinate system used in defining the image plane by simulating a photograph of the glitter pattern on the water surface. P locates the camera film image plane a distance f along $\tilde{a}$ from S, the specular reflection point on the sea surface. $\tilde{t}$ is the image of ray $\tilde{\xi}$ from S.

the glitter pattern in nature. We may also imagine a scuba diver who photographs the glitter pattern of the sun's transmitted rays. In this case the camera below the surface is pointed upward, and the photograph is usually developed so that it has the zenith toward the top and the horizon toward the bottom.

Associated with a point light source are its *specular* reflection and transmission directions. These are the directions of the reflected and transmitted rays generated when the incoming ray $\underset{\sim}{\xi}'$, as in Fig. 14, strikes a flat horizontal surface (the case of zero wind speed). The initial $\underset{\sim}{\xi}'$ and specular ray path $\underset{\sim}{a}$ lie in the same vertical plane. For the numerical simulation of glitter pattern photographs, we will use coordinate systems based around these specular directions. The optical axes of cameras are aligned along the specular ray paths, and the cameras point toward the specular point on the ocean surface.

Figure 15 shows the four general camera positions used to present glitter patterns. Camera A photographs air-incident reflected rays, the usual case of the sun's glitter on the sea surface. The camera angle θ_c is θ_s', the angle of reflection for a level surface. Camera B, located along the specular transmission ray path, photographs the glitter pattern of air-incident transmitted rays. The camera angle is (by (3.18)) $\theta_c = \arcsin(\sin\theta_s'/m)$, the angle of refraction for a flat horizontal water surface. Cameras C and D photograph the reflected and refracted glitter patterns for an underwater light source. If the underwater light source is positioned so that there would be no transmitted rays for a calm surface, the camera D axis is placed in the specular (mean) water surface, and thus is pointed horizontally.

We now introduce the *image plane*. This plane can be thought of as the plane of the film in a camera. In Fig. 14, with the camera at P, we first

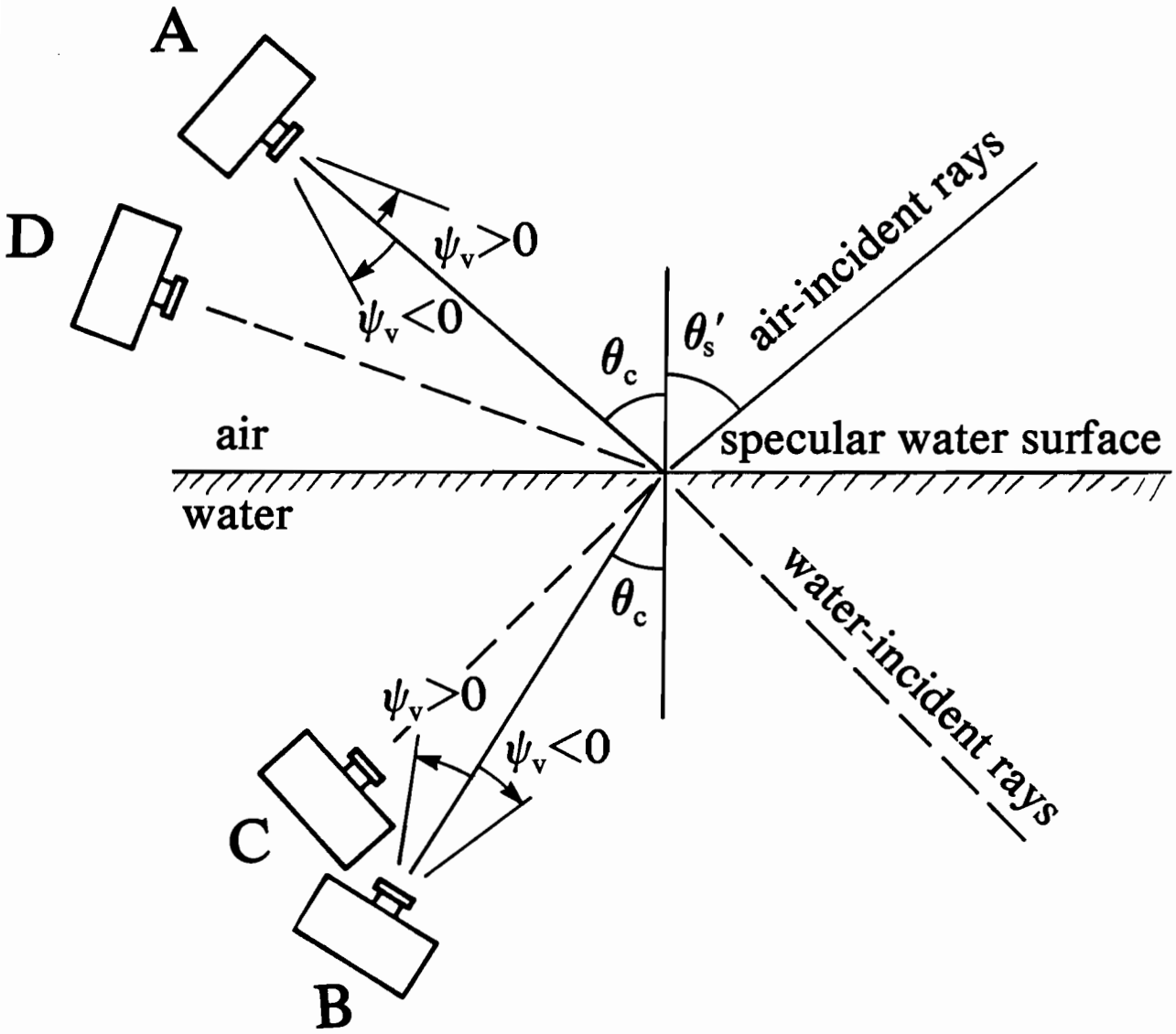

Figure 15.--Camera positions for viewing the four types of glitter patterns.

choose a sun-based coordinate system $\underset{\sim}{x}$-$\underset{\sim}{y}$-$\underset{\sim}{z}$ centered at the camera's specular point S on the water surface. The unit vector $\underset{\sim}{x}$ direction is chosen so that the incoming rays $\underset{\sim}{\xi}' = (\xi_x', \xi_y', \xi_z')$ always have $\xi_x' > 0$ and $\xi_y' = 0$. The unit vector $\underset{\sim}{z}$ axis is vertical upward and $\underset{\sim}{y}$ is chosen so that $\underset{\sim}{y} = \underset{\sim}{z} \times \underset{\sim}{x}$. The camera axis direction $\underset{\sim}{a}$ is chosen to be the specular reflection ($\underset{\sim}{\xi}_r$) or refraction ($\underset{\sim}{\xi}_t$) direction, depending on the case under study (Fig. 14 shows the case of camera position A in Fig. 15). The image plane at P is a plane perpendicular to the camera axis $\underset{\sim}{a}$ and positioned at a distance f (which simulates the focal length of the camera) from S along $\underset{\sim}{a}$. We thus imagine a camera at P pointed in the $-\underset{\sim}{a}$ direction. A coordinate system $\underset{\sim}{h}$-$\underset{\sim}{v}$ for the image plane is chosen by setting $\underset{\sim}{h} \equiv -\underset{\sim}{y}$ and $\underset{\sim}{v} \equiv \underset{\sim}{a} \times \underset{\sim}{h}$. This choice of $\underset{\sim}{h}$ and $\underset{\sim}{v}$ is such that, when the image plane of Fig. 14 (i.e. the camera film) is turned upside down for viewing as a photograph, the $\underset{\sim}{h}$ and $\underset{\sim}{v}$ axes will appear as horizontal and vertical axes appropriate to the photograph. The computer-generated glitter pattern will then appear as if a photograph were actually taken of a real air-water surface.

To locate glitter points in the image plane, we proceed as follows. Let an arbitrary ray along $\underset{\sim}{\xi}$ from S intersect the image plane at a point $\underset{\sim}{t} \equiv t_h\underset{\sim}{h} + t_v\underset{\sim}{v} \equiv (t_h, t_v)$. The image plane coordinates t_h and t_v are introduced to specify the location of a point in the image plane relative to the origin P of the $\underset{\sim}{h}$ and $\underset{\sim}{v}$ axes. Let $\underset{\sim}{t}$ be at a distance λ along $\underset{\sim}{\xi}$ from the specular point S. Note that $\underset{\sim}{t}$, lying in the image plane, is perpendicular to $\underset{\sim}{a}$. Then the vector identity

$$\lambda\underset{\sim}{\xi} = f\underset{\sim}{a} + \underset{\sim}{t} \tag{7.1}$$

yields $\lambda = f/\underset{\sim}{\xi}\cdot\underset{\sim}{a}$. The components of $\underset{\sim}{t}$ are, by (7.1),

$$t_h = \underset{\sim}{t}\cdot\underset{\sim}{h} = f\ \underset{\sim}{\xi}\cdot\underset{\sim}{h}/\underset{\sim}{\xi}\cdot\underset{\sim}{a}$$

and

$$t_v = \underset{\sim}{t}\cdot\underset{\sim}{v} = f\ \underset{\sim}{\xi}\cdot\underset{\sim}{v}/\underset{\sim}{\xi}\cdot\underset{\sim}{a}\ .$$

Substituting for $\underset{\sim}{h} = -\underset{\sim}{y}$ and $\underset{\sim}{v} = \underset{\sim}{a} \times \underset{\sim}{h}$, gives t_h and t_v in terms of $\underset{\sim}{\xi} = (\xi_x,\xi_y,\xi_z)$ and $\underset{\sim}{a} = (a_x,a_y,a_z) = (a_x,0,a_z)$:

$$t_h = -f\ \xi_y/\underset{\sim}{\xi}\cdot\underset{\sim}{a}$$

and (7.2)

$$t_v = f(\xi_x a_z - \xi_z a_x)/\underset{\sim}{\xi}\cdot\underset{\sim}{a}\ .$$

Once the camera position is fixed (i.e. f and $\underset{\sim}{a}$ are chosen), (7.2) yields the image plane coordinates of any ray $\underset{\sim}{\xi}$ (for which $\underset{\sim}{\xi}\cdot\underset{\sim}{a} > 0$).

An inverse relation for $\underset{\sim}{\xi}$ in terms of $\underset{\sim}{t}$ in the image plane is obtained from (7.1) after using the Pythagorean relation on right triangle $SP\underset{\sim}{t}$ to find that $\lambda = (f^2 + t_h^2 + t_v^2)^{\frac{1}{2}}$. We then have

$$\underset{\sim}{\xi} = (f^2 + t_h^2 + t_v^2)^{-\frac{1}{2}}\ (f\underset{\sim}{a} + t_h\underset{\sim}{h} + t_v\underset{\sim}{v})\ .$$

Expressing $\underset{\sim}{h}$ and $\underset{\sim}{v}$ in terms of $\underset{\sim}{x}$, $\underset{\sim}{y}$, and $\underset{\sim}{z}$, this may be written

$$\xi_x = (f^2 + t_h^2 + t_v^2)^{-\frac{1}{2}}\ (fa_x + t_v a_z)$$

$$\xi_y = (f^2 + t_h^2 + t_v^2)^{-\frac{1}{2}}\ (-t_h) \qquad (7.3)$$

$$\xi_z = (f^2 + t_h^2 + t_v^2)^{-\frac{1}{2}}\ (fa_z - a_x t_v)\ .$$

The ray-tracing model generates a glitter pattern on the image plane of Fig. 14 as follows. A light source with location direction angles (θ_s', ϕ_s') is chosen, and the associated incident ray $\underset{\sim}{\xi}'$ is aimed at a target point of the hexagonal grid. The incoming ray $\underset{\sim}{\xi}'$ is scattered by a realization of the random surface, and the final daughter rays $\underset{\sim}{\xi}$ are recorded. This process is repeated for each of an ensemble of surface realizations presented to $\underset{\sim}{\xi}'$. Those daughters rays which have $\underset{\sim}{\xi} \cdot \underset{\sim}{a} > 0$ generate a distribution of points (t_h, t_v) in the image plane. A plot of the (t_h, t_v) locations is the model-generated glitter pattern.

The directions $\underset{\sim}{\xi}'$ and $\underset{\sim}{\xi}$ characterize the initial and final rays. During the Monte Carlo simulation, the process of scattering $\underset{\sim}{\xi}'$ to $\underset{\sim}{\xi}$ can be thought of as occurring at the fixed point S of Fig. 14. When a camera records a glitter pattern, the camera, located at point P of Fig. 14, records rays $\underset{\sim}{\xi}$ which actually have been scattered from various points of the water surface other than S. However, the pattern of points in the image plane, generated by the Monte Carlo ray tracing procedure over each of an ensemble of randomly realized surfaces, is equivalent to a simulated photograph of an extended statistically homogeneous area of the sea surface irradiated, say, by sunlight, provided the ensemble of surfaces is itself statistically stationary. That is, the set of (t_h, t_v) points arising from the traces of a single $\underset{\sim}{\xi}'$ incident in turn at point S on each of an ensemble of sea surface realizations (as in Fig. 14) is statistically equivalent to the set of (t_h, t_v) points produced by an ensemble of rays parallel to $\underset{\sim}{\xi}'$ and simultaneously incident at points randomly chosen on a single realization of the surface and then focussed (as by a camera lens) onto the image plane. In this way we use the ergodic equivalence between the Duntley and the Cox-Munk approaches described in section 1B to justify the image plane approach of Fig. 14.

To assist in visualizing a glitter pattern formed from the (t_h,t_v) points in the image plane, we define horizontal and vertical viewing angles ψ_h and ψ_v as follows. Let a glitter point on the image plane be at (t_h,t_v). Let $\underset{\sim}{\xi}_h$ and $\underset{\sim}{\xi}_v$ be unit vectors emanating from S whose extensions intersect the viewing plane at point $(t_h,0)$ lying on the $\underset{\sim}{h}$ axis and at point $(0,t_v)$ on the $\underset{\sim}{v}$ axis, as shown in Fig. 14. Then

$$\psi_h \equiv \arccos(\underset{\sim}{\xi}_h \cdot \underset{\sim}{a})\ \mathrm{sign}[t_h] \tag{7.4a}$$

$$\psi_v \equiv \arccos(\underset{\sim}{\xi}_v \cdot \underset{\sim}{a})\ \mathrm{sign}[t_v]. \tag{7.4b}$$

The viewing angles have been given the signs of t_h and t_v.

The inverse relation between ψ_h and t_h is obtained at once by simple trigonometry from Fig. 14, or formally via (7.3). In the latter case, as a check on (7.3), for $\underset{\sim}{\xi} = \underset{\sim}{\xi}_h$, we have $t_v \equiv 0$ and $\underset{\sim}{a} = (a_x,0,a_z)$, with $\underset{\sim}{a}\cdot\underset{\sim}{a} = a_x^2 + a_z^2 \equiv 1$. Then the relation $\cos\psi_h = \underset{\sim}{\xi}_h \cdot \underset{\sim}{a}$ reduces to

$$\cos\psi_h = (f^2 + t_h^2)^{-\frac{1}{2}}\,(fa_x^2 + fa_z^2) = f(f^2 + t_h^2)^{-\frac{1}{2}}.$$

Squaring and solving for t_h gives

$$t_h^2 = f^2(\sec^2\psi_h - 1)\ .$$

On reducing this (via the positive square root) we obtain the required form for t_h which, along with its similarly derived companion t_v, may be summarized as

$$t_h = f \tan\psi_h \tag{7.5a}$$

$$t_v = f \tan\psi_v \tag{7.5b}$$

Figure 16 further clarifies the relation between the image plane and a glitter pattern photograph. The top panel of Fig. 16 shows a particular instance of the $\underset{\sim}{\xi}'$-$\underset{\sim}{a}$ plane ($t_h \equiv 0$) of Fig. 14, corresponding to camera position A of Fig. 15. An incoming ray $\underset{\sim}{\xi}'$ with $\theta_s' = 60°$ is reflected by a non horizontal water facet at S to generate a reflected ray $\underset{\sim}{\xi}$ with $\theta = 45°$, which strikes the image plane at $\underset{\sim}{t}$. The camera axis $\underset{\sim}{a}$ is fixed by the specular reflection direction at $\theta_c = \theta_s' = 60°$. The viewing angle ψ_v associated with $\underset{\sim}{\xi}$ is seen to be $\psi_v = -15°$. A ray reflected straight up would strike the image plane at $\psi_v = -60°$, and a horizontally reflected ray would have $\psi_v = +30°$.

We now show that this method of recording glitter patterns is a reasonable simulator of glitter photographs. The bottom panel of Fig. 16 shows the image plane of the top panel turned "upside down" and placed at point S. We now imagine an observer in an aircraft at point P. The ray $\underset{\sim}{\xi}'$ is reflected by a wave facet at R to generate a reflected ray $\underset{\sim}{\xi}$ which is seen by the observer. We note that the ray $\underset{\sim}{\xi}$ coming from point R on the ocean surface is exactly what the observer would see if he were looking at point $\underset{\sim}{t}$ in the relocated image plane. The observer looking along the camera axis, $\psi_v = 0$, is looking at the specular point S. If the observer lifts his eyes upward from S by 30°, he sees the ocean horizon, which corresponds to $\psi_v = +30°$ in the bottom panel's photograph. Looking downward by 60°, i.e. at $\psi_v = -60°$ in the photograph, the observer at P sees the point on the ocean surface directly below him. In this way the image plane technique for recording ray paths, as

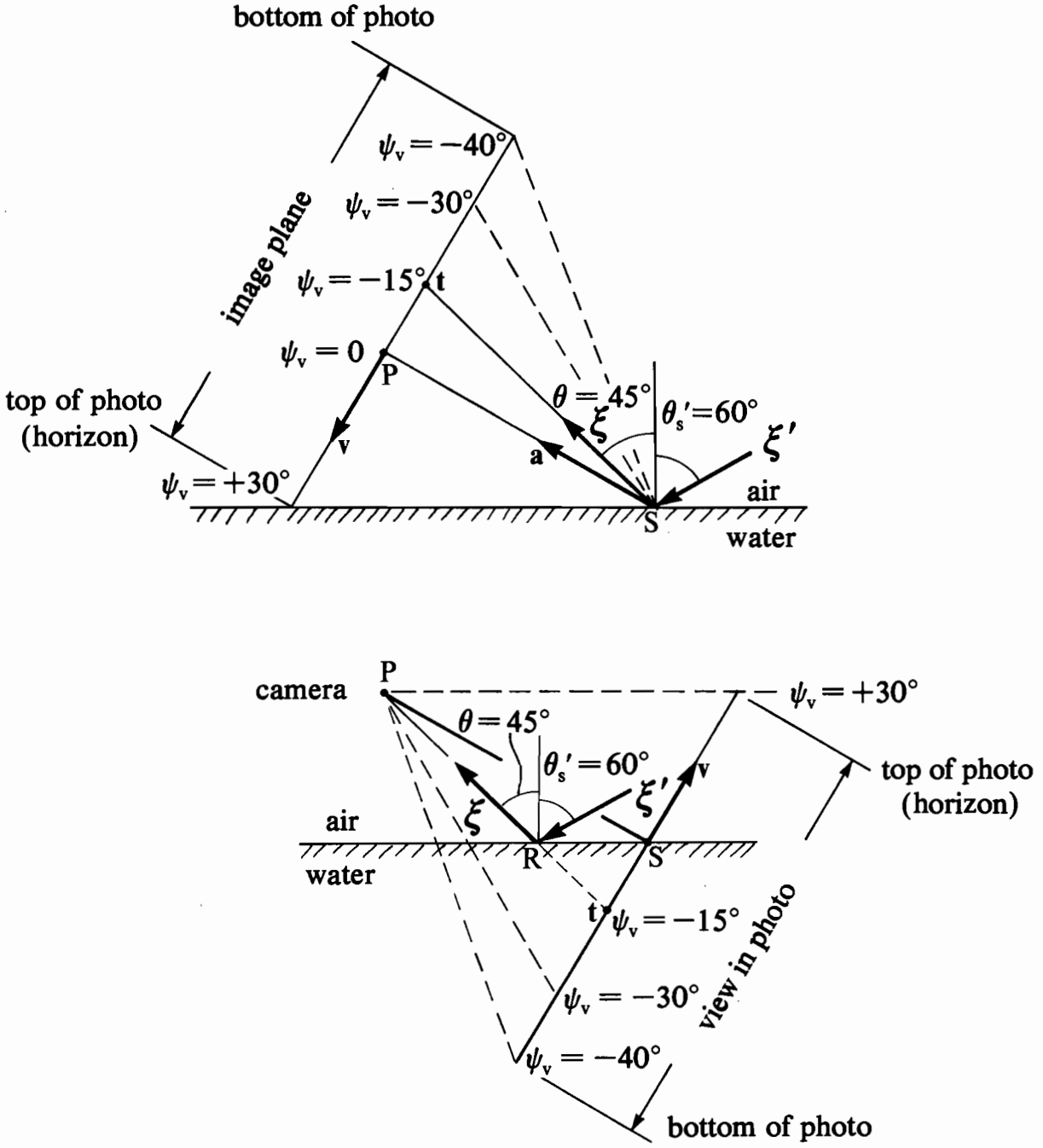

Figure 16.--Turning the image plane "upside down" to simulate a photograph of a glitter pattern.

shown in Fig. 14, enables us to simulate glitter pattern photographs, and we see that ψ_h and ψ_v are properly referred to as "viewing angles." The above definitions and coordinate systems hold without change for the other camera positions of Fig. 15. Since only the ray directions are of importance, we can set $f \equiv 1$ without loss of generality.

It is important to note that the coordinate systems used to represent glitter patterns are sun-based, since the $\underset{\sim}{x}$, $\underset{\sim}{y}$, and $\underset{\sim}{z}$ axes (cf. Fig. 14) are defined in relation to the incoming ray direction $\underset{\sim}{\xi}'$, which most often in applications will be emanating from the sun. Specifically, $\underset{\sim}{x}$ is chosen so that $\xi_x' > 0$ and $\xi_y' = 0$, where $\underset{\sim}{\xi}'$ is the incoming ray. The $\underset{\sim}{i}$-$\underset{\sim}{j}$-$\underset{\sim}{k}$ coordinate system (cf. Figs. 4 and 14) used in the ray-tracing calculations, on the other hand, is "wind-based," since $\underset{\sim}{i}$ by construction is always in the direction of the wind. These two systems are shown schematically in Fig. 14. Each coordinate system is the logical one for its purpose, and minimal effort is required to switch between them since they are related by a rotation about their common vertical axes, $\underset{\sim}{z} = \underset{\sim}{k}$. Thus suppose the light source is located at an angle ϕ_s' relative to the wind direction (measured counterclockwise from the $\underset{\sim}{i}$-axis in the $\underset{\sim}{i}$-$\underset{\sim}{j}$ plane), so that a ray $\underset{\sim}{\xi}'$ coming *from* the light source has $\phi' = 180° + \phi_s'$. Then the angle from $\underset{\sim}{i}$ to $\underset{\sim}{x}$ is ϕ'. Consequently, a vector $\underset{\sim}{v}$ with components $\underset{\sim}{v}_{wind} = (v_i, v_j, v_k)$ in the wind-based system has components $\underset{\sim}{v}_{sun} = (v_x, v_y, v_z)$ in the sun-based system given by

$$\underset{\sim}{v}_{sun} = \begin{pmatrix} v_x \\ v_y \\ v_z \end{pmatrix} = \begin{pmatrix} \cos\phi' & \sin\phi' & 0 \\ -\sin\phi' & \cos\phi' & 0 \\ 0 & 0 & 1 \end{pmatrix} \begin{pmatrix} v_i \\ v_j \\ v_k \end{pmatrix}, \tag{7.6a}$$

which is easily inverted to get $\underset{\sim}{v}_{wind}$ from $\underset{\sim}{v}_{sun}$:

$$\underset{\sim}{v}_{wind} = \begin{pmatrix} v_i \\ v_j \\ v_k \end{pmatrix} = \begin{pmatrix} \cos\phi' & -\sin\phi' & 0 \\ \sin\phi' & \cos\phi' & 0 \\ 0 & 0 & 1 \end{pmatrix} \begin{pmatrix} v_x \\ v_y \\ v_x \end{pmatrix} . \qquad (7.6b)$$

In practice, all vectors from the ray tracing calculations are immediately transformable by (7.6a) so that the resulting vectors can be used in the sun-based glitter pattern diagrams when sun and wind directions are arbitrarily related.

Cox and Munk (op. cit.) used the glitter pattern to deduce the orientations of the reflecting wave facets relative to the zenith and the sun. In order to conveniently specify the facet orientations that produce the glitter points on their photographs, they defined azimuth and tilt angles α and β, respectively, for the facet normal and overlaid α and β isolines on their photographs. We also adopt these angles as a way of displaying the facet information of a glitter pattern. Let $\underset{\sim}{n}$ be the surface normal of that wave facet which reflects or refracts a ray $\underset{\sim}{\xi}'$ into the $\underset{\sim}{\xi}$ direction. Then α and β are defined by

$$\alpha \equiv \arctan(-n_y/n_x) \qquad \text{(azimuth angle, positive clockwise from } \underset{\sim}{i})$$

and (7.7)

$$\beta \equiv \arccos(\underset{\sim}{n}\cdot\underset{\sim}{k}) = \arccos(n_z), \qquad \text{(tilt angle from } \underset{\sim}{k})$$

where $\underset{\sim}{n} = (n_x, n_y, n_z)$ is measured in the sun-based coordinate system of Fig. 14. Given the initial and final ray directions $\underset{\sim}{\xi}'$ and $\underset{\sim}{\xi}$, the facet normal $\underset{\sim}{n}$, on recalling Fig. 9, is available from any one of the appropriate relations:

$$\underset{\sim}{n} = (\underset{\sim}{\xi} - \underset{\sim}{\xi}')/\|\underset{\sim}{\xi} - \underset{\sim}{\xi}'\| \quad \text{for air-incident reflected rays, or} \tag{7.8a}$$

$$\underset{\sim}{n} = (\underset{\sim}{\xi}' - m\underset{\sim}{\xi})/\|\underset{\sim}{\xi}' - m\underset{\sim}{\xi}\| \quad \text{for air-incident transmitted rays, or} \tag{7.8b}$$

$$\underset{\sim}{n} = (\underset{\sim}{\xi}' - \underset{\sim}{\xi})/\|\underset{\sim}{\xi}' - \underset{\sim}{\xi}\| \quad \text{for water-incident reflected rays, or} \tag{7.8c}$$

$$\underset{\sim}{n} = (m\underset{\sim}{\xi}' - \underset{\sim}{\xi})/\|m\underset{\sim}{\xi}' - \underset{\sim}{\xi}\| \quad \text{for water-incident transmitted rays.} \tag{7.8d}$$

It should be noted that for a given $\underset{\sim}{\xi}'$ and $\underset{\sim}{\xi}$ in the above formulas, the $\underset{\sim}{n}$ and α,β values are those of a unique wave facet which would scatter $\underset{\sim}{\xi}'$ into $\underset{\sim}{\xi}$. Observe, however, that the final $\underset{\sim}{\xi}$ ray used in making a glitter photograph in our diagrams may have been generated as a result of multiple scattering of a parent ray from two or more facets; nevertheless, at each intermediate scattering facet, the incoming and outgoing rays are related by (3.18) or (3.19). Hence for a given incident $\underset{\sim}{\xi}'$ a single realized surface $S(\omega)$ can give rise to one or more glitter points in the final pattern.

We can draw contours of α and β on the image plane as follows. Fix the focal length f and the camera axis $\underset{\sim}{a}$. At each point of a regular grid of (t_h,t_v) values in the image plane, determine the associated $\underset{\sim}{\xi}$ by (7.3). Then $\underset{\sim}{n}$ is obtained from (7.8), and finally the α and β values to be associated with point (t_h,t_v) are found from (7.7). These arrays of $\alpha(t_h,t_v)$ and $\beta(t_h,t_v)$ values can then be used in a contouring subroutine to draw lines of constant α and constant β on a generated glitter pattern.

B. Examples of glitter patterns

We now present a sequence of numerically generated glitter patterns. These patterns were made using capillary waves for a variety of wind speeds and light source locations. In accordance with the conventions described above, the glitter patterns are plotted in the sun-based coordinate system of

Fig. 14. The computations, however, are done in the wind-based coordinate system (cf. section 3). Our source location angles (θ_s', ϕ_s'), in particular, are measured in the wind-based system. θ_s' is measured from the zenith (air-incident case) or nadir (water-incident case). ϕ_s' is measured positive counterclockwise from $\underset{\sim}{i}$ in the $\underset{\sim}{i}$-$\underset{\sim}{j}$ plane.

Figure 17 is presented for comparison with an actual glitter pattern photograph, Fig. 18. Figure 17 was generated for the air-incident case with a wind speed of U = 5 m/s (at 12.5 m elevation) and a point light source located at $\theta_s' = 60°$ from the zenith. Panel a has the light source in the alongwind or $\phi_s' = 180°$ direction, and panel b has the source in the crosswind or $\phi_s' = 90°$ direction (cf. Figs. 4 and 14). The geometry is similar to that of Fig. 16, in that the camera angle is $\theta_c = 60°$ and a viewing angle $\psi_v = 30°$ corresponds to looking toward the ocean horizon. The angular field of view in Fig. 17 is seen to be from 30° above the specular point (i.e. from the horizon) to 50° below the specular point (almost to the observer's nadir), and 30° to either side of the specular point. Contours of the wave facet angles α and β are displayed. A small dot is plotted at each of 2,000 ray-image plane intersections to generate the glitter pattern. A qualitative feeling for the brightness, or radiance, of the glitter pattern is given by the area density of the scattered dots. A more faithful representation of the radiance could be obtained by making the size of each dot proportional to the radiant flux associated with the ray, but for our present purposes (outlined at the outset of this section) simply locating the ray-image plane intersections is sufficient.

Comparison of Figs. 17a and 17b shows the effects of the anisotropy of the capillary waves. In Fig. 17a the wind is blowing from the top to bottom of the picture, while in Fig. 17b the wind is blowing from left to right. The

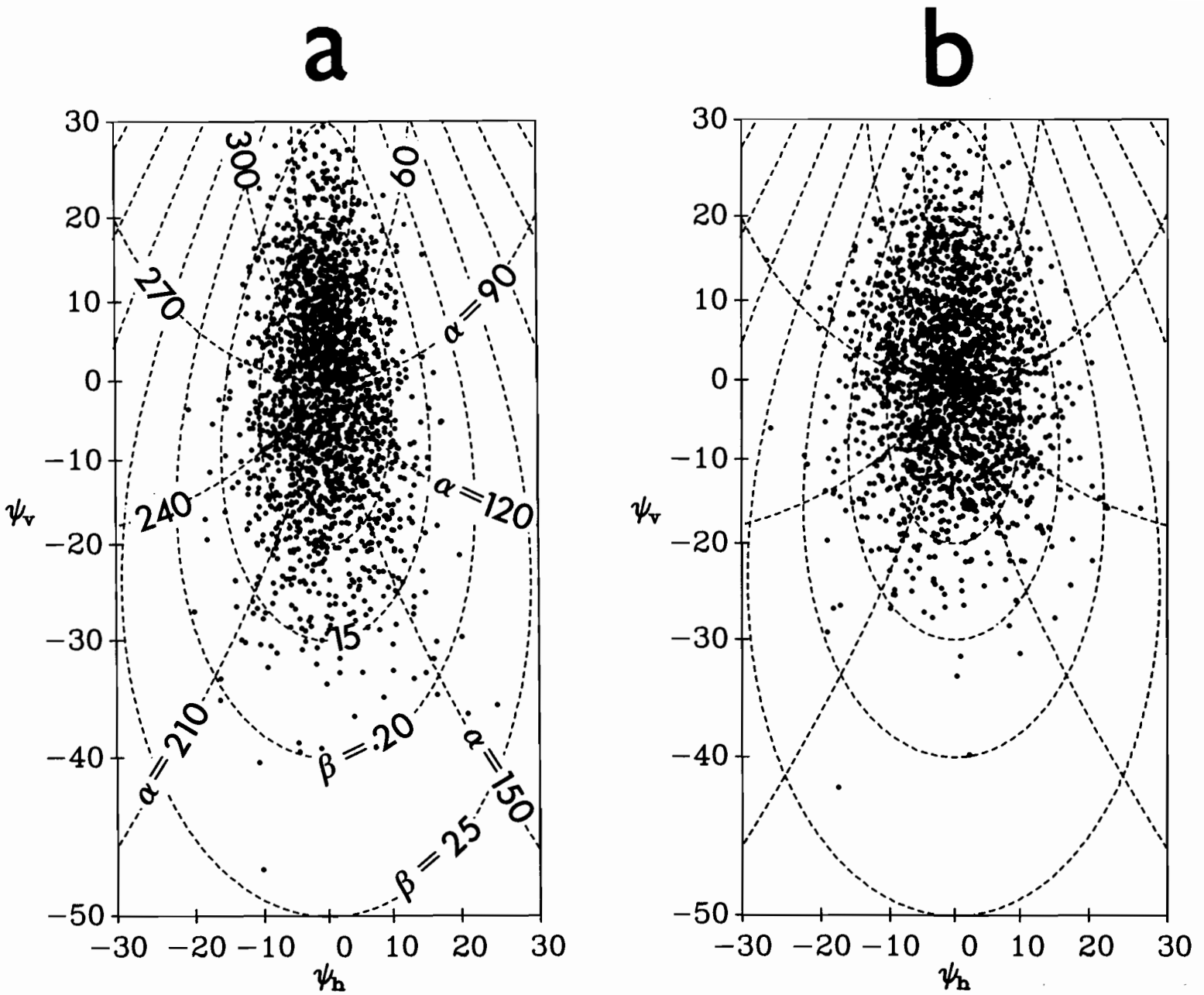

Figure 17.--Model-generated glitter patterns for comparison with Fig. 18. Panel (a) has parameter values $\theta_s' = 60°$, $\phi_s' = 180°$, $\theta_c = 60°$ and U = 5 m/s with 2000 points plotted. Panel (b) is the same except that $\phi_s' = 90°$. ϕ_s' is measured positive counterclockwise from $\hat{i}$ in the wind-based system.

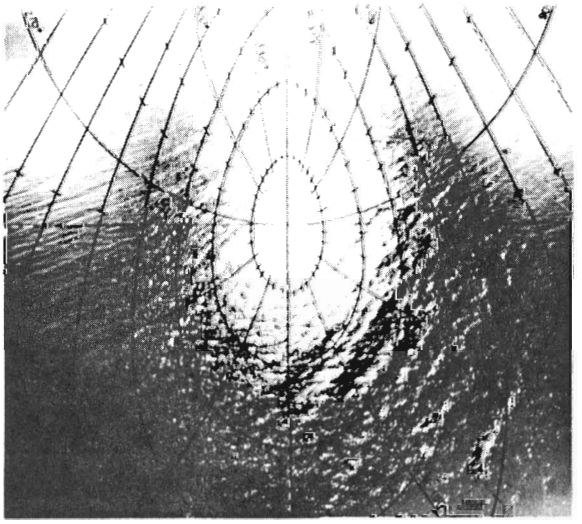

Figure 18.--Photograph of a glitter pattern on the open ocean. The conditions were similar to those modeled in Fig. 17.

glitter pattern of Fig. 17a, for which the air-incident rays are parallel to the wind, is somewhat more elongated than the pattern of Fig. 17b, for which the air-incident rays are perpendicular to the wind. This shape difference in the glitter patterns occurs because rays incident parallel to the wind tend to encounter the wave facets "head on" and are thus more strongly influenced by the upwind slope, ζ_u. Rays incident perpendicular to the wind are more influenced by the crosswind slope, ζ_c. Recall that the variances of these slopes are such that $\sigma_u^2 > \sigma_c^2$ in Eqs. (2.1), (2.1)' (with p = 1).

Figure 18 is a photograph by Cox and Munk of a physical situation similar to those used to generate Fig. 17. In particular, the sun angle θ_s' is the same, and the wind speed was 9 knots ($\cong$ 4.6 m/s) at 12.5 m elevation, although the wind direction ϕ_s' relative to the sun is not known. There are several features in the photograph which are not modeled in the ray-tracing calculations, namely striations in the glitter, due to ocean swell, and diffuse side lobes of glitter. However, the major features of the actual glitter pattern centered on the specular point are well reproduced in Fig. 17, as can be seen by comparing the "brightness" of the figures at corresponding β contours. The β contours of Fig. 18 are in 5° increments beginning with $\beta = 5°$.

Figure 19 shows the development of an air-incident capillary-wave reflected glitter pattern as a function of wind speed. Other parameter values are the same as in Fig. 17a, except that a wider-angle view is taken. In Fig. 19a, we see a small, very dense pattern for a wind speed of 1 m/s. As the wind increases through 5, 10 and 20 m/s in panels b, c and d, the glitter pattern becomes larger and less dense at its center. From the β contours of Fig. 19a, we see that at U = 1 m/s only rarely is a wave facet normal tilted by as much as 10° from the vertical, the bulk being around 2° or 3° (cf.

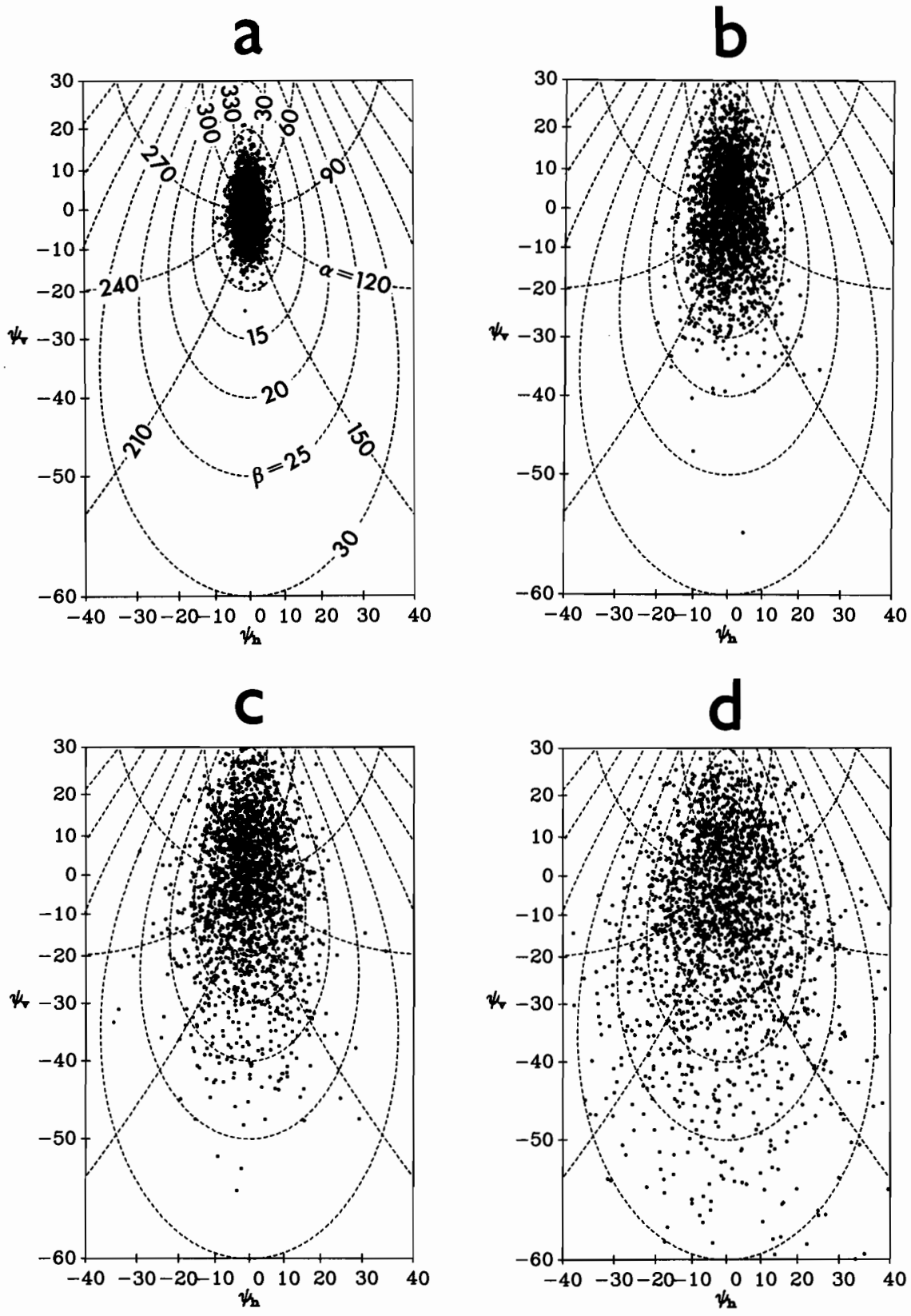

Figure 19.--Dependence of the glitter pattern on wind speed for fixed air-incident light source. Each diagram is for $\theta_s' = 60°$, $\phi_s' = 180°$, $\theta_c = 60°$ with 2000 points. Diagram (a) is for U = 1 m/s, (b) 5 m/s, (c) 10 m/s, (d) 20 m/s.

Fig. 13). At winds of 20 m/s, Fig. 19d shows occasional facet tilts of β greater than 30°.

Figure 20 illustrates the dependence of the air-incident reflected glitter pattern on solar position for a given wind speed of 5 m/s. Figure 20a shows a pattern for the light source at $\theta_s' = 1.0°$ and $\phi_s' = 180°$. The camera is essentially looking straight down with the sun overhead. The pattern is nearly circular, although there is a slight elongation in the alongwind direction (top to bottom of the picture) due to the anisotropy of the capillary wave surface. Figure 20b has $\theta_s' = 80°$ and $\phi_s' = 180°$, and Fig. 20c has $\theta_s' = 80°$ and $\phi_s' = 90°$. Just as in Fig. 17, we see an elongation of the pattern for the alongwind source location compared to the pattern for the crosswind source location. The glitter patterns are now becoming elongated into the "road to happiness" (Shuleikin, 1968, p. 383) due to the near-horizontal angle of incidence of the incoming rays. Figure 20d shows the case of a setting sun, $\theta_s' = 90°$ and $\phi_s' = 180°$. The "road to happiness" is now fully developed.

The above Figs. 17-20 have all been for the usual case of air-incident reflected rays (camera position A in Fig. 15). Cox and Munk (1955) also estimated the appearance of glitter patterns of air-incident transmitted rays as seen from below the water surface (camera position B of Fig. 15). Figure 21a shows our glitter pattern for air-incident transmitted rays for the same parameter values as those of the reflected rays in Fig. 20a. The camera is looking essentially straight up toward the sun. The glitter pattern is much more compressed relative to Fig. 20, as is expected from the laws of geometric optics. Only 500 points are plotted, due to the compactness of the pattern.

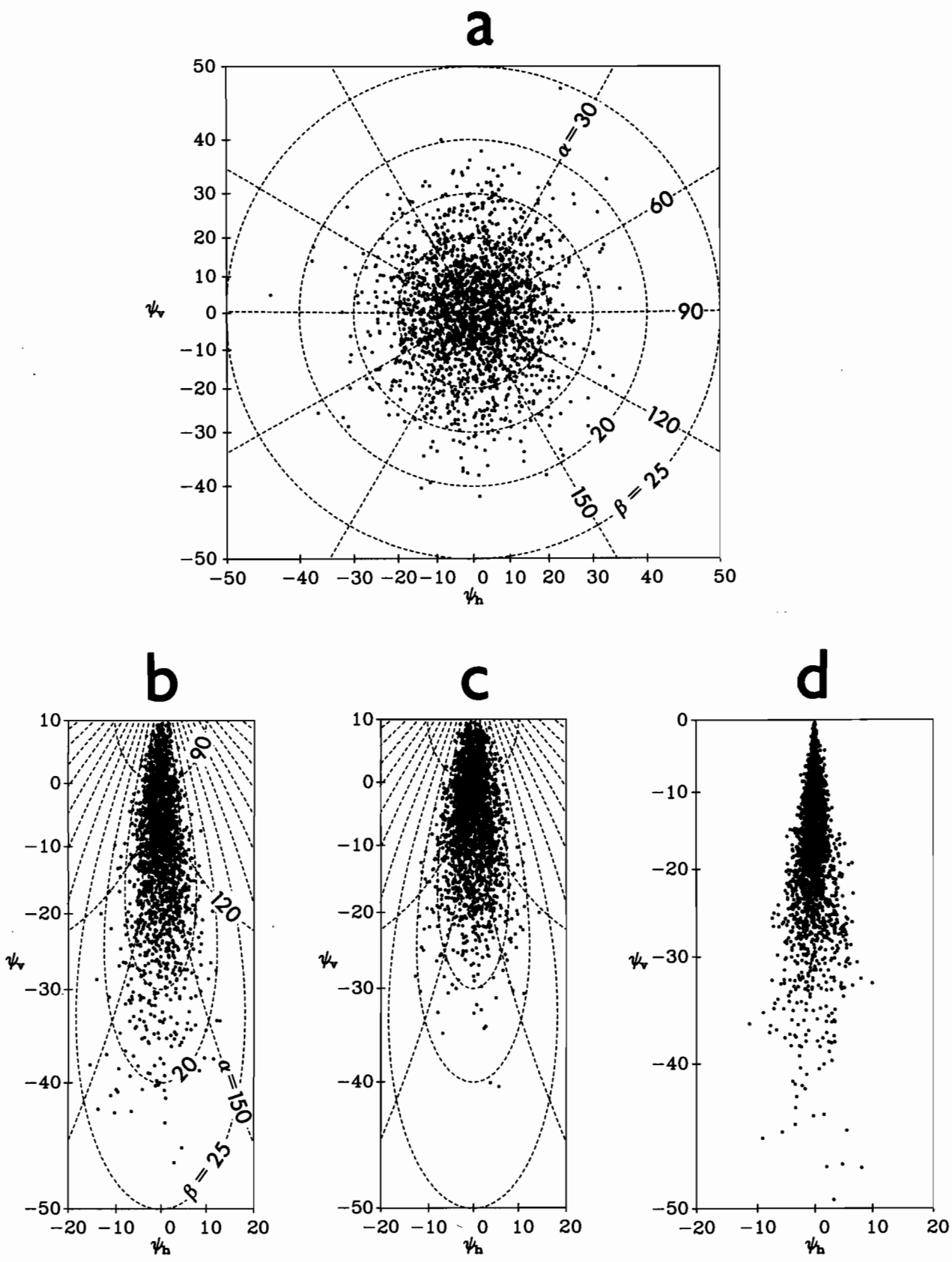

Figure 20.--Dependence of the glitter pattern on light source location for air-incident reflected rays. For each panel the wind speed is 5 m/s, $\theta_c = \theta_s'$, and 2000 points are plotted. Panel (a) has $\theta_s' = 1°$, $\phi_s' = 180°$, (b) has $\theta_s' = 80°$, $\phi_s' = 180°$, (c) has $\theta_s' = 80°$, $\phi_s' = 90°$, and (d) has $\theta_s' = 90°$, $\phi_s' = 180°$.

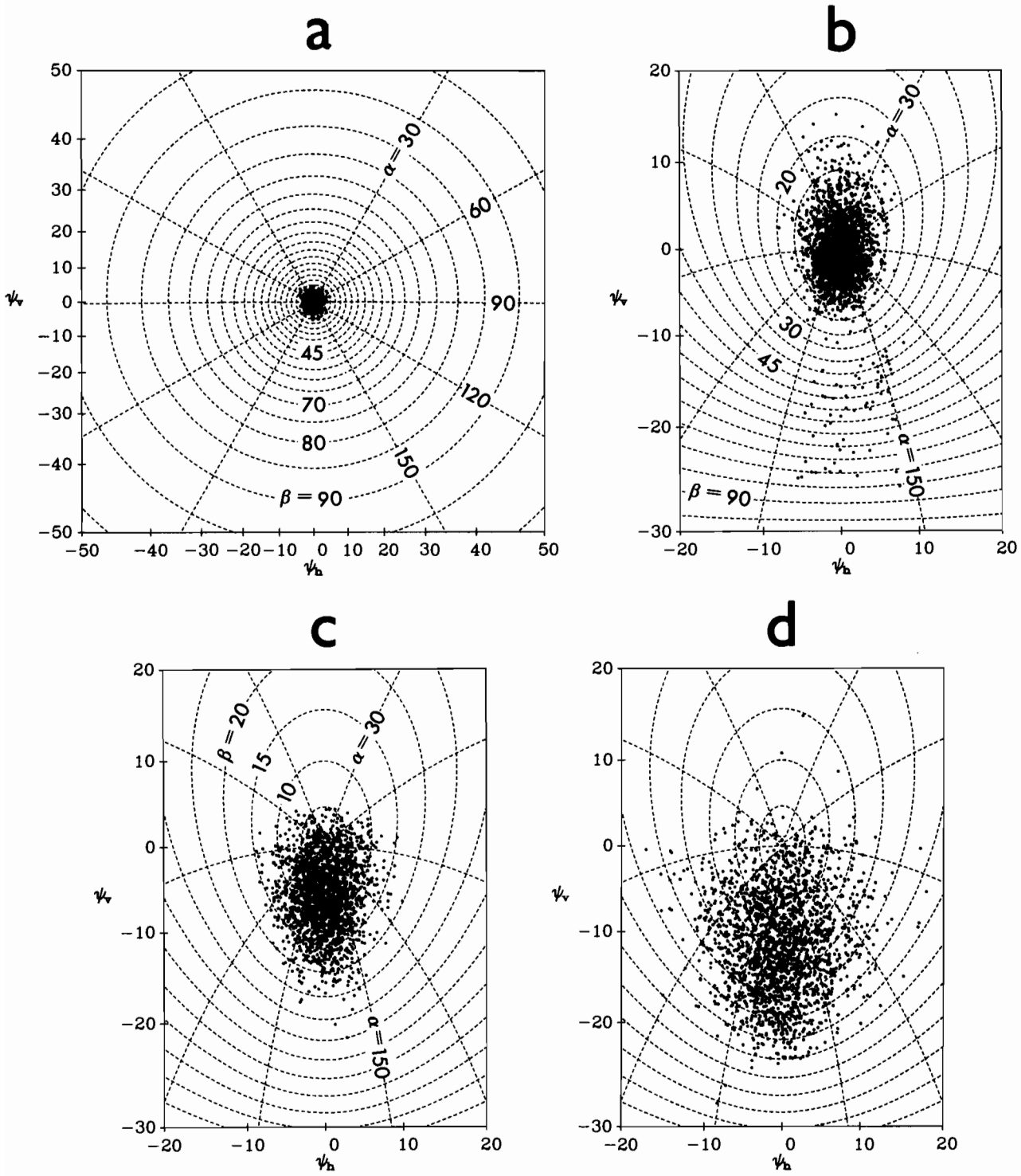

Figure 21.--Glitter patterns for air-incident transmitted rays. Panel (a) has $\theta_s' = 1°$, $\phi_s' = 180°$, $\theta_c = 0.7°$, U = 5 m/s and 500 points plotted. Panel (b) has $\theta_s' = 60°$, $\phi_s' = 180°$, $\theta_c = 40.5°$, U = 5 m/s and 2000 points. Panels (c) and (d) each have $\theta_s' = 85°$, $\phi_s' = 180°$, $\theta_c = 48.3°$ and 2000 points; (c) has U = 5 m/s and (d) has U = 20 m/s.

Figure 21b shows the air-incident transmitted ray pattern for the same parameter values as Fig. 17a, namely $\theta_s' = 60°$, $\phi_s' = 180°$ and U = 5 m/s. The camera angle is now $\theta_c' = 40.5°$, as determined by the specular transmission direction. Most of the 2000 transmitted rays deviate less than 10° from the specular direction, as seen from the ψ_h and ψ_v values, although there is a noticeable sprinkling of points below and outside the main pattern. Figs. 21c and 21d have $\theta_s' = 85°$, $\phi_s' = 180°$ and $\theta_c = 48.3°$. Figure 21c has U = 5 m/s and Fig. 21d has U = 20 m/s. In each of these figures the glitter pattern is shifted away from the specular transmission direction. As in the reflected ray case, an increasing wind speed gives a more diffuse pattern, although the effect is not as pronounced in the case of transmitted rays.

Glitter patterns for water-incident reflected rays (camera position C in Fig. 15), in the form of dot-density diagrams, appear on the whole the same as those for air-incident reflected rays (camera position A in Fig. 15), since the presently constructed capillary surface appears the same from above or below. However, if the glitter patterns were generated with the dot size proportional to the radiant flux of the rays, then the patterns for water-incident reflected rays would appear brighter than those of the air-incident case, because of the greater Fresnel reflectance for water-incident rays.

The patterns for water-incident transmitted rays in principle should be much different than those of the air-incident transmitted case. Figure 22a shows the pattern for rays passing almost straight up through the surface (camera position D in Fig. 15 with the camera looking almost straight down). The pattern is not quite as compact as the corresponding air-incident case of Fig. 21a and is in accord with the well-known magnification effect of the water surface on submerged objects. Figure 22b shows the case for a water-incident angle of $\theta_s' = 45°$ and $\phi_s' = 180°$ for a unidirectional source spatially

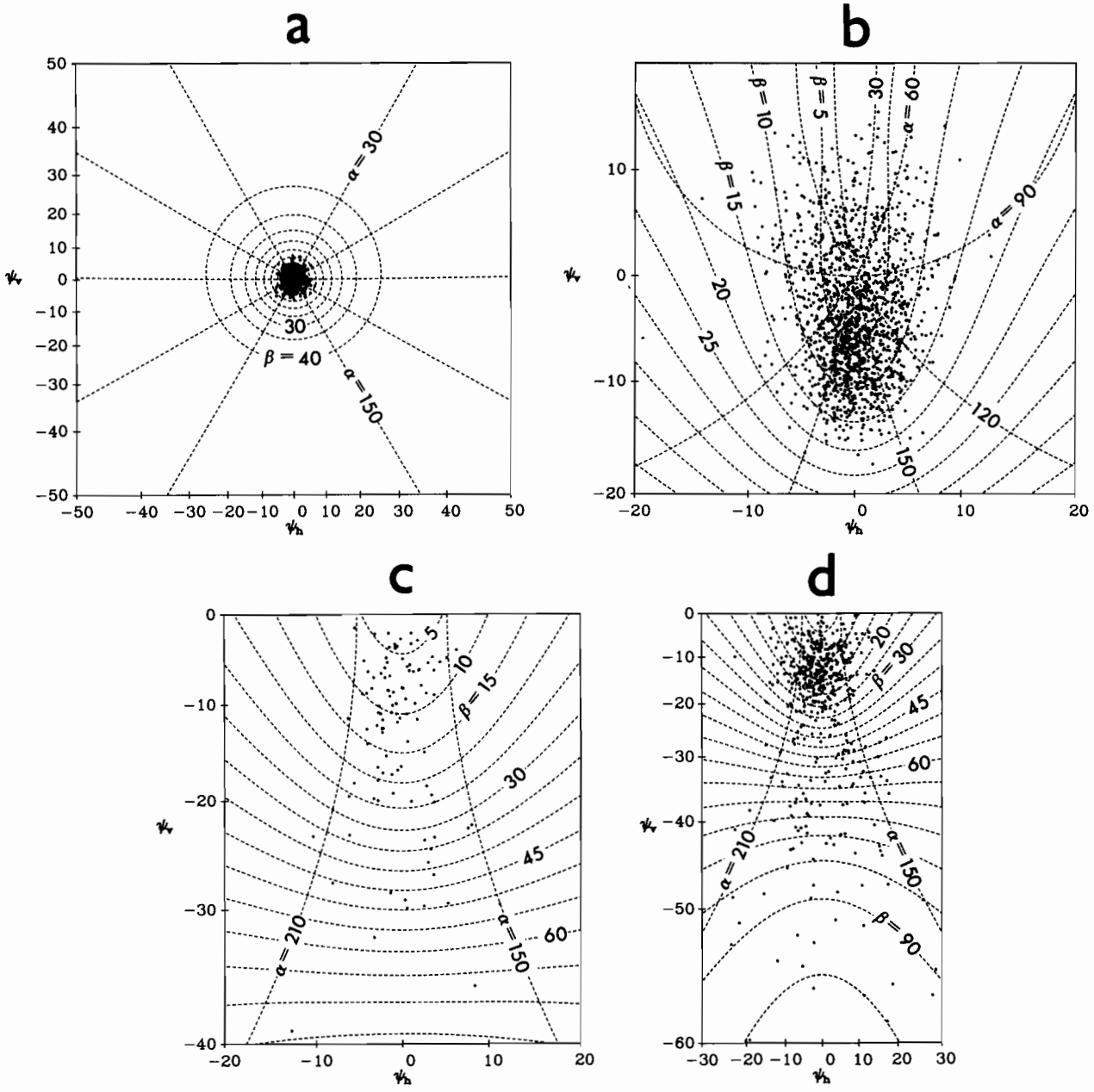

Figure 22.--Glitter patterns for water-incident transmitted rays. θ_s' is measured from the nadir to the source location. Panel (a) has $\theta_s' = 1°$, $\phi_s' = 180°$, $\theta_c = 1.3°$, U = 5 m/s and 500 points plotted. Panel (b) has $\theta_s' = 45°$, $\phi_s' = 180°$, $\theta_c = 70.5°$, U = 5 m/s and 1369 points. Panels (c) and (d) each have $\theta_s' = 60°$, $\phi_s' = 180°$ and $\theta_c = 90°$. Panel (c) has U = 5 m/s and 105 points; (d) has U = 20 m/s and 468 points.

distributed just below the water surface, with $\theta_c = 70.5°$. This θ_s' is measured from the nadir and is near the critical angle of 48.59° for total internal reflection, in the specular case. For the wind speed of 5 m/s shown in Fig. 22b, only 1369 of 2000 incident rays were transmitted; the other 631 rays encountered facets which were tilted so as to cause total internal reflections. Figures 22c and 22d both have $\theta_s' = 60°$ and $\phi_s' = 180°$. For a specular surface there would be no transmitted rays at this value of θ_s', and therefore the camera angle is set to $\theta_c = 90°$. Note from the ψ_v values that the tops of the figures are at the horizon and the entire view is then downward toward the water surface. As the wind increases, an occasional facet is sufficiently tilted so as to transmit a ray through the surface. At U = 5 m/s, shown in Figure 22c, 105 of 2000 incident rays passed through the surface to generate a sparse glitter pattern. At U = 20 m/s, shown in Figure 22d, 468 of 2000 rays were able to pass through the surface.

C. First-order theory

The glitter patterns presented in the previous section were generated by rays which use the full power of the present ray-tracing model. No distinction was made between rays which intersected the image plane after a single scattering and those which were the final products of a multiple-scattering event. But it is of interest to know, for example, what contribution multiply-scattered rays make to a glitter pattern. One approach to this problem would be to alter the ray-tracing code so that multiply-scattered rays are ignored and the glitter pattern is generated by singly-scattered rays only. The two glitter patterns could then be compared. Another approach is that of comparing an exactly produced glitter pattern with one predicted by an analytic first-order theory; this approach is the topic of this section.

On the assumption that the water surface is undulating gently, various nonlinear features of the surface and of the resulting glitter pattern theory can be neglected. The result is a simple linear theory which predicts the shape and dot-density distribution of a glitter pattern. We now develop a linearized theory for rays reflected by capillary waves. The theory is inspired by some notes of Eckart (1946).

Let ζ be a realization of a random function defined on the wind-based $\underset{\sim}{i}$-$\underset{\sim}{j}$ plane of Fig. 1, the mean sea surface. ζ simulates the water surface and is assumed to be continuously differentiable. Let ζ_u and ζ_c be the slopes of the realized water surface in the upwind and crosswind directions, respectively. The joint probability density $p(\zeta_u,\zeta_c)$ of occurrence of these slopes is assumed to be a binormal distribution

$$p(\zeta_u,\zeta_c) = \frac{1}{2\pi\sigma_u\sigma_c} \exp\left[-\tfrac{1}{2}\left(\frac{\zeta_u^2}{\sigma_u^2} + \frac{\zeta_c^2}{\sigma_c^2}\right)\right] , \tag{7.9}$$

where σ_u^2 and σ_c^2 are given in Eq. (2.1) with $p = 1$. Observe that ζ_u and ζ_c are assumed to be independent random variables. The unit normal to the wave surface is given by

$$\underset{\sim}{n} = (1 + \zeta_u^2 + \zeta_c^2)^{-\frac{1}{2}} (-\zeta_u \underset{\sim}{i} - \zeta_c \underset{\sim}{j} + \underset{\sim}{k}) . \tag{7.10}$$

Thus $\underset{\sim}{n}$ is measured in the wind-based coordinate system of Fig. 4, which we recall has the wind in the $+\underset{\sim}{i}$ direction. If the surface is only slightly perturbed, the wave slopes ζ_u and ζ_c are small in magnitude, and the higher order terms ζ_u^2 and ζ_c^2 can be neglected. Thus an approximate first-order surface normal is

$$\underset{\sim}{n} \approx -\zeta_u \underset{\sim}{i} - \zeta_c \underset{\sim}{j} + \underset{\sim}{k} \,. \tag{7.11}$$

We now have the option of choosing an air-incident or a water-incident ray $\underset{\sim}{\xi}'$, and also the option of choosing a reflectance or a transmittance calculation. To fix ideas, we consider the following. An air-incident ray $\underset{\sim}{\xi}' \equiv \xi_u' \underset{\sim}{i} + \xi_c' \underset{\sim}{j} + \xi_3' \underset{\sim}{k}$ is reflected into a direction $\underset{\sim}{\xi}$ given by (3.18):

$$\underset{\sim}{\xi} = \underset{\sim}{\xi}' - 2(\underset{\sim}{\xi}' \cdot \underset{\sim}{n})\, \underset{\sim}{n}.$$

Substituting the approximate normal $\underset{\sim}{n}$ from (7.11) gives an approximate $\underset{\sim}{\xi}$, which in wind-based component form becomes

$$\underset{\sim}{\xi} \approx (\xi_u', \xi_c', -\xi_3') + 2(\xi_3'\zeta_u, \xi_3'\zeta_c, \xi_u'\zeta_u + \xi_c'\zeta_c) \equiv \underset{\sim}{\xi}_o + \underset{\sim}{\varepsilon}.$$

Here $\underset{\sim}{\xi}_o \equiv (\xi_u', \xi_c', -\xi_3')$ is the specular reflection direction for $\underset{\sim}{\xi}'$ and

$$\underset{\sim}{\varepsilon} \equiv 2(\xi_3'\zeta_u, \xi_3'\zeta_c, \xi_u'\zeta_u + \xi_c'\zeta_c)$$

is a *deflection vector* (in the wind-based system) representing the difference between the specular reflection direction $\underset{\sim}{\xi}_o$ and the actual (although approximate)* reflection direction $\underset{\sim}{\xi}$. Note that $\underset{\sim}{\xi}_o \cdot \underset{\sim}{\varepsilon} = 0$. Since ζ_u and ζ_c are independent normal variates distributed as in (7.9), the deflection vector $\underset{\sim}{\varepsilon}$ is a random vector whose three components are normal random variates of zero means and variances $4\xi_3'^2\sigma_u^2$, $4\xi_3'^2\sigma_c^2$, and $4(\xi_u'^2\sigma_u^2 + \xi_c'^2\sigma_c^2)$, respectively, in the $\underset{\sim}{i}$-$\underset{\sim}{j}$-$\underset{\sim}{k}$ coordinate system.

* If we had chosen the air-incident transmittance option, then we would have used the ξ_t representation in (3.18) with the (7.11) form of $\underset{\sim}{n}$, and would have obtained a similar decomposition $\xi_o + \underset{\sim}{\varepsilon}$ of $\underset{\sim}{\xi}$. The other two options are pursued in a similar fashion.

Since $\underset{\sim}{\xi}_o$ and $\underset{\sim}{\varepsilon}$ are perpendicular, it is possible to define a *deflection plane* which is analogous to the image plane in Fig. 14. Accordingly, we are guided by the image plane concept of Fig. 14 and set $f = 1$, $\underset{\sim}{a} = \underset{\sim}{\xi}_o$, and recall that $\underset{\sim}{z} = \underset{\sim}{k}$ in both sun- and wind-based systems. Then define the deflection plane axes $\underset{\sim}{h}$ and $\underset{\sim}{v}$ as $\underset{\sim}{h} \equiv (\underset{\sim}{\xi}_0 \times \underset{\sim}{k})/\|\underset{\sim}{\xi}_0 \times \underset{\sim}{k}\|$ and $\underset{\sim}{v} \equiv \underset{\sim}{\xi}_o \times \underset{\sim}{h}$. Substituting $\underset{\sim}{\xi}_o$ in these relations and expanding we find

$$\underset{\sim}{h} = (\xi_u'^2 + \xi_c'^2)^{-\frac{1}{2}}(\xi_c'\underset{\sim}{i} - \xi_u'\underset{\sim}{j})$$

and

$$\underset{\sim}{v} = -(\xi_u'^2 + \xi_c'^2)^{-\frac{1}{2}} [(\xi_u'\xi_3')\underset{\sim}{i} + (\xi_c'\xi_3')\underset{\sim}{j} + (\xi_u'^2 + \xi_c'^2)\underset{\sim}{k}]$$

as measured in the wind-based system. We can measure $\underset{\sim}{\varepsilon}$ in the deflection plane, relative to the basis $\underset{\sim}{h},\underset{\sim}{v}$ as

$$\varepsilon_h \equiv \underset{\sim}{\varepsilon}\cdot\underset{\sim}{h} = 2\xi_3'(\xi_u'^2 + \xi_c'^2)^{-\frac{1}{2}} (\xi_c'\zeta_u - \xi_u'\zeta_c)$$

$$\varepsilon_v \equiv \underset{\sim}{\varepsilon}\cdot\underset{\sim}{v} = -2(\xi_u'^2 + \xi_c'^2)^{-\frac{1}{2}} (\xi_u'\zeta_u + \xi_c'\zeta_c) .$$

Noting that

$$\cos\phi' = \xi_u'(\xi_u'^2 + \xi_c'^2)^{-\frac{1}{2}}$$

and

$$\sin\phi' = \xi_c'(\xi_u'^2 + \xi_c'^2)^{-\frac{1}{2}},$$

where ϕ' is the azimuth angle of the $\underset{\sim}{\xi}'$ vector measured positive counterclockwise from $\underset{\sim}{i}$ in the $\underset{\sim}{i}$-$\underset{\sim}{j}$ plane to the $\underset{\sim}{x}$-axis (cf. Fig. 14), we find

$$\varepsilon_h = 2\xi_3'(\zeta_u \sin\phi' - \zeta_c \cos\phi')$$

$$\varepsilon_v = -2(\zeta_u \cos\phi' + \zeta_c \sin\phi') \ . \tag{7.12}$$

Equation set (7.12) gives the desired first-order theory of the glitter pattern. The interpretation of $(\varepsilon_h, \varepsilon_v)$ is that of a randomly located point in the deflection plane. Since ζ_u and ζ_c are normal random variables of zero mean, so too are ε_h and ε_v. The second order moments of ε_h and ε_v are

$$E\{\varepsilon_h^2\} \equiv \sigma_h^2 = 4\xi_3'^2(\sigma_u^2 \sin^2\phi' + \sigma_c^2 \cos^2\phi') \ ,$$

$$E\{\varepsilon_v^2\} \equiv \sigma_v^2 = 4(\sigma_u^2 \cos^2\phi' + \sigma_c^2 \sin^2\phi') \ ,$$

and

$$E\{\varepsilon_h \varepsilon_v\} = 4\xi_3'^2(\sigma_c^2 - \sigma_u^2)\cos\phi' \sin\phi' \ ,$$

where E is the ensemble average operator which averages the indicated quantity over all realizations of the random surface ζ. Therefore the $(\varepsilon_h, \varepsilon_v)$ points in the deflection plane for the cases of $\phi' = 0°$, $90°$, $180°$, or $270°$ obey a normal probability density function in which ε_h and ε_v are uncorrelated:

$$p(\varepsilon_h, \varepsilon_v) = \frac{1}{2\pi\sigma_h\sigma_v} \exp\left[-\tfrac{1}{2}\left(\frac{\varepsilon_h^2}{\sigma_h^2} + \frac{\varepsilon_v^2}{\sigma_v^2}\right)\right] \ . \tag{7.13}$$

Observe, from the presence of ξ_3' in $E\{\varepsilon_h^2\}$ for the case $\phi' = 0$, how the predicted glitter pattern becomes elongated toward the horizon as the light source descends toward the horizon.

Equation (7.13) suggests a means of comparing the set of ray-dots of a Monte-Carlo produced pattern, or even an actual glitter pattern, with that of

the first-order theory under identical conditions. If the patterns of ray dots are sufficiently close, then the first-order theory is deemed adequate; otherwise, the first-order theory fails perhaps because higher-order processes (multiple scattering, or shielding, or nonlinear hydrodynamics) have in some way distorted the glitter pattern. In this manner we can determine the parameter values (e.g., wind speed, incident ray direction) for which a first-order theory is a reasonable approximation to reality. We shall compare the present first-order theory with the Monte Carlo procedure.

One matter remains before making this comparison of ray-dot patterns. The $(\varepsilon_h,\varepsilon_v)$ points refer to the deflection plane, but the glitter pattern points (t_h,t_v) refer to the image plane of the full model. We must be able to convert $(\varepsilon_h,\varepsilon_v)$ values into (t_h,t_v) values, and inversely. The details of such transformations are as follows. It is assumed that $f = 1$ and the common value $\underset{\sim}{a} = \underset{\sim}{\xi}_0$ is known, so that the image and deflection planes are well-defined and coincide.

For the transformation from $(\varepsilon_h,\varepsilon_v)$ to (t_h,t_v):

(1) Eq. (7.12) is inverted to find those slopes ζ_u,ζ_c in the first-order theory that are consistent with $(\varepsilon_h,\varepsilon_v)$, namely

$$\zeta_u = \left(\frac{\sin\phi'}{2\xi_3'}\right)\varepsilon_h - \left(\frac{\cos\phi'}{2}\right)\varepsilon_v$$

$$\zeta_c = -\left(\frac{\cos\phi'}{2\xi_3'}\right)\varepsilon_h - \left(\frac{\sin\phi'}{2}\right)\varepsilon_v \ .$$

(2) The facet normal $\underset{\sim}{n}$ in the wind-centered system is obtained from (7.10), using the (ζ_u,ζ_c) just found.

(3) The facet normal's components in the sun-based coordinate system are obtained from (7.6), and likewise $\underset{\sim}{\xi}'$ is represented in the sun-based system.

(4) The reflected ray $\underset{\sim}{\xi}$ associated with $(\varepsilon_h,\varepsilon_v)$ is obtained in the sun-based system from (3.18), in which $\underset{\sim}{n}$ and $\underset{\sim}{\xi}'$ of step (3) above are used.

(5) Finally, $\underset{\sim}{\xi}$ is substituted into (7.2) to obtain the (t_h,t_v) values associated with $(\varepsilon_h,\varepsilon_v)$.

The inverse transformation from (t_h,t_v) to the corresponding $(\varepsilon_h,\varepsilon_v)$ is effected as follows:

(1) The $\underset{\sim}{\xi}$ in the sun-based system associated with (t_h,t_v) is obtained from (7.3). (The values of $\underset{\sim}{a}$, f, and $\underset{\sim}{\xi}'$ are known for the image plane.)

(2) The facet normal $\underset{\sim}{n} = (n_x,n_y,n_z)$ in the sun-based system is obtained from (7.8a).

(3) The facet normal $\underset{\sim}{n} = (n_u,n_c,n_3)$ in the wind-based system is obtained from the inverse of (7.6).

(4) The slopes in the wind-based system are obtained from

$$\zeta_u = -n_u/n_3 \quad \text{and} \quad \zeta_c = -n_c/n_3 \ .$$

(5) The slopes from step (4) are exact. Under the first-order model assumption they are used in (7.12) to find $(\varepsilon_h,\varepsilon_v)$.

Returning now to the deflection plane and the distribution (7.13) for $(\varepsilon_h,\varepsilon_v)$, we proceed with the comparison of exact and approximate glitter models as follows. Defining

$$\varepsilon^2 \equiv \frac{\varepsilon_h^2}{\sigma_h^2} + \frac{\varepsilon_v^2}{\sigma_v^2} ,$$

Eq. (7.13) becomes

$$p(\varepsilon_h,\varepsilon_v) = \frac{1}{2\pi\sigma_h\sigma_v} \exp(-\tfrac{1}{2}\varepsilon^2) ,$$

and we observe that the set of points $(\varepsilon_h,\varepsilon_v)$, such that ε is a constant, defines an ellipse of "radius" ε in the deflection plane. We next find the probability mass contained within such an ellipse. Defining an angular parameter ω,

$$\begin{aligned} \varepsilon_h &\equiv \sigma_h \varepsilon \cos\omega \\ & \qquad 0 \le \omega \le 2\pi , \\ \varepsilon_v &\equiv \sigma_v \varepsilon \sin\omega \end{aligned} \tag{7.14}$$

the probability density function p of (7.13) can be transformed from rectangular $(\varepsilon_h,\varepsilon_v)$ coordinates to polar (ε,ω) coordinates via

$$p(\varepsilon_h,\varepsilon_v)d\varepsilon_h d\varepsilon_v \equiv p_0(\varepsilon,\omega)d\varepsilon d\omega.$$

where p_0 is the polar coordinate form of p. The Jacobian of the transformation is

$$J = \begin{vmatrix} \frac{\partial\varepsilon_h}{\partial\varepsilon} & \frac{\partial\varepsilon_h}{\partial\omega} \\ \frac{\partial\varepsilon_v}{\partial\varepsilon} & \frac{\partial\varepsilon_v}{\partial\omega} \end{vmatrix} = \begin{vmatrix} \sigma_h\cos\omega & -\sigma_h\varepsilon\sin\omega \\ \sigma_v\sin\omega & \sigma_v\varepsilon\cos\omega \end{vmatrix} = \sigma_h\sigma_v\varepsilon .$$

Therefore

$$p_0(\varepsilon,\omega) = J\ p(\varepsilon_h,\varepsilon_v) = \frac{\varepsilon}{2\pi} \exp(-\tfrac{1}{2}\varepsilon^2) \ .$$

Integrating $p_0(\varepsilon,\omega)$ over $0 \le \omega \le 2\pi$ yields

$$q(\varepsilon) \equiv \int_0^{2\pi} p_0(\varepsilon,\omega)d\omega = \varepsilon\exp(-\tfrac{1}{2}\varepsilon^2) \ ,$$

and integrating $q(\varepsilon')$ over $0 \le \varepsilon' \le \varepsilon$ gives

$$Q(\varepsilon) = \int_0^{\varepsilon} q(\varepsilon')d\varepsilon' = 1 - \exp(-\tfrac{1}{2}\varepsilon^2) \ .$$

$Q(\varepsilon)$ represents the probability mass contained within the $(\varepsilon_h,\varepsilon_v)$ ellipse of radius ε. The inverse relation

$$\varepsilon = [-2\ \log(1 - Q)]^{\frac{1}{2}} \qquad (7.15)$$

gives the radius of the ellipse containing an amount Q, $0 \le Q < 1$, of the probability mass.

Selecting values of Q = 0.5, 0.9 and 0.99, say, Eqs. (7.14) and (7.15) allow us to draw the $(\varepsilon_h,\varepsilon_v)$-ellipses in the deflection plane which contain on average 50%, 90% and 99% of the $(\varepsilon_h,\varepsilon_v)$ points, respectively. Then the (t_h,t_v) points of the actual glitter pattern are mapped from the image plane onto the deflection plane via the (t_h,t_v) to $(\varepsilon_h,\varepsilon_v)$ transformation described above. The numbers of actual ray points in the Monte Carlo produced glitter pattern which fall within the various contours of Q are then counted. A χ^2

goodness-of-fit test between the numbers of points predicted by first-order theory and the observed numbers of ray points in the glitter pattern is then made. The hypothesis being tested is

H_o: The glitter pattern (distribution of points in the image plane) produced by Monte Carlo ray tracing is compatible with the first-order theory.

The χ^2 test is performed as follows. The values Q = 0.5, 0.9 and 0.99 define four disjoint classes of points that partition the deflection plane into elliptical annuli whose probability masses under the null hypothesis H_o are respectively $p_1 = 0.5$, $p_2 = 0.4$, $p_3 = 0.09$ and $p_4 = 0.01$. Under the $(\varepsilon_h,\varepsilon_v)$ to (t_h,t_v) mapping, these elliptical annuli produce a similar partition of the image plane into probability classes. For example, under H_o, the probability of a randomly chosen point (t_h,t_v) in the glitter pattern falling between the Q = 0.5 and Q = 0.9 contours (i.e., mapped ellipses) is $p_2 = 0.4$. In a glitter pattern of N points, let N_j be the number of points falling in the jth of the four image plane probability classes (thus $N_1 + N_2 + N_3 + N_4 = N$). Then set

$$\chi^2 = \sum_{j=1}^{k=4} \frac{(N_j - Np_j)^2}{Np_j} \,. \tag{7.16}$$

We choose to test H_o at the $\alpha = 0.01$ significance level, for which the critical value is $\chi^2(\alpha,k-1) = \chi^2(0.01,3) = 11.325$. We then accept or reject H_o according to the following scheme:

accept H_o if $\chi^2 < \chi^2(\alpha,k-1)$

or

reject H_o if $\chi^2 \geq \chi^2(\alpha,k-1)$.

Figure 23 shows three glitter patterns in the image plane produced by the Monte Carlo ray tracing procedure. The Q-labeled contours are the images, under the $(\varepsilon_h,\varepsilon_v)$ to (t_h,t_v) mapping, of the elliptical contours in the deflection plane. Deflection plane regions defined by the Q-contours and containing probability masses of Q = 0.5, 0.9 and 0.99 according to the first-order theory are thus seen superimposed on the Monte Carlo realized glitter patterns. The parameters in each pattern differ only in the incident θ_s' values used. For each panel, $\phi_s' = 180°$, U = 5 m/s and 2000 points are plotted. It is not easy for the eye to discern from Fig. 23 whether or not each pattern should lead to an acceptance of H_o. The distorted ellipses in panels b and c should give a preliminary indication that the first-order theory is perhaps not adequate in all these cases.

The results of testing H_o for the three patterns of Fig. 23 are displayed in Table 1. Here we see that for the $\theta_s' = 1°$ case of Fig. 23a, the realized distribution of points is close to that predicted by first order theory, leading to a very small χ^2 of 0.720 and thus acceptance of H_o. The case of $\theta_s' = 60°$ produces a real pattern with χ^2 less than the critical value; so H_o is accepted. However, for the $\theta_s' = 85°$ case of Fig. 23c, the glitter pattern is relatively diffuse; i.e. not enough points fall in the central part of the pattern and too many fall in the outer regions, causing χ^2 to be large and thus H_o to be rejected. Hence in this case the first order theory is not adequate to describe the Monte Carlo produced results.

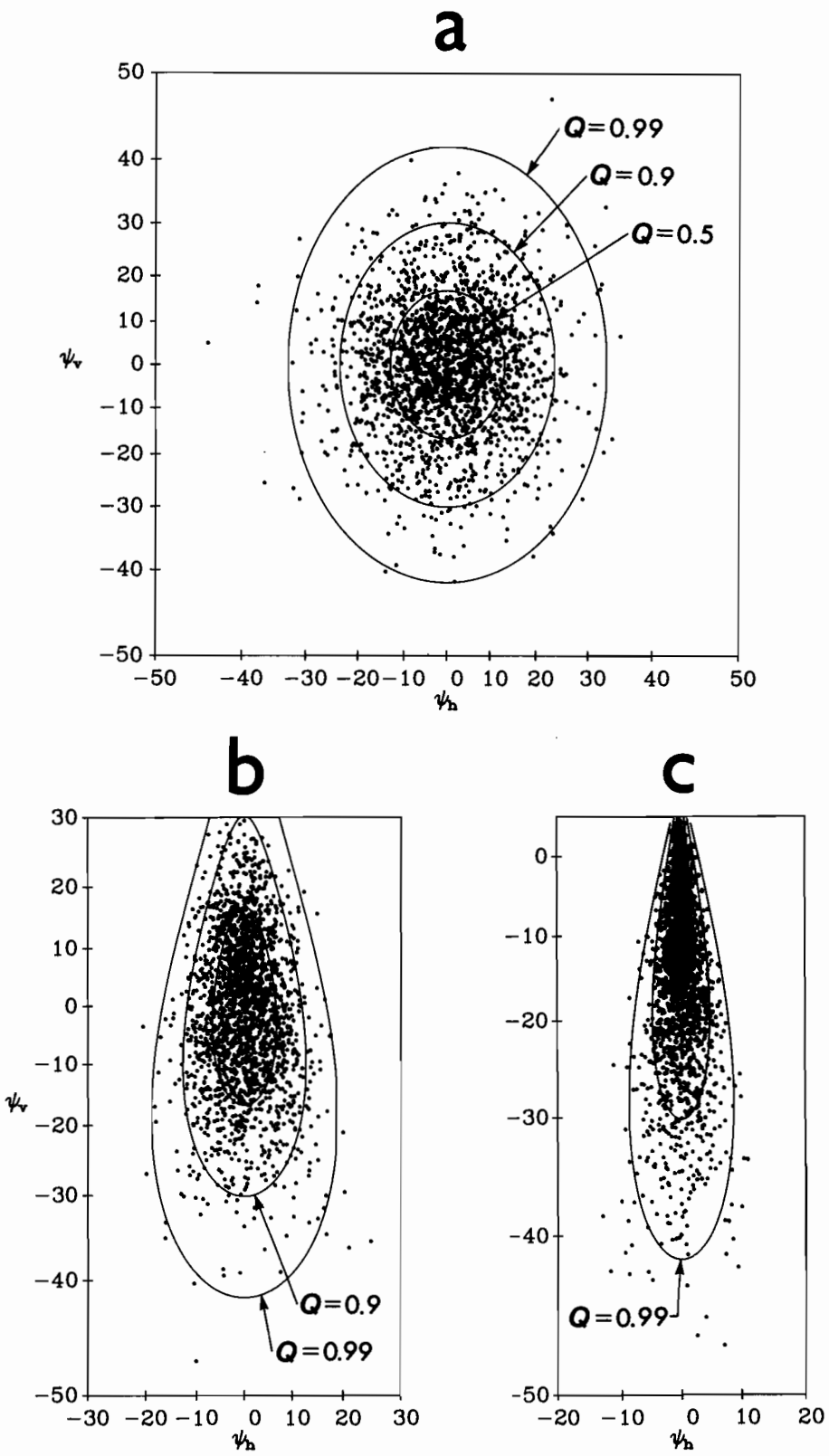

Figure 23.--Glitter patterns for air-incident reflected rays used for the hypothesis tests of Table 1. The Q-contours are the transformed (mapped) ellipses defined by first-order theory and delineate regions containing probability mass Q = 0.5, 0.9 and 0.99. These ellipses are mapped into the image plane of the exact Monte Carlo method using the $(\varepsilon_h, \varepsilon_v)$ to (t_h, t_v) mapping described in the text. Each panel has $\phi_s' = 180°$, $\theta_c = \theta_s'$, $U = 5$ m/s and 2000 points. Panel (a) has $\theta_s' = 1°$, (b) has $\theta_s' = 60°$ and (c) has $\theta_s' = 85°$.

	θ_s'	categories				χ^2	comments
		$0 \le Q \le 0.5$	$0.5 < Q \le 0.9$	$0.9 < Q \le 0.99$	$0.99 < Q \le 1$		
category populations expected under hypothesis H_o	--	1000	800	180	20	11.325	critical value $\chi^2(\alpha,k-1) = \chi^2(0.01,3)$
realized category populations	1°	985	806	189	20	0.720	clear acceptance
	60°	1044	796	147	13	10.456	borderline acceptance
	85°	837	862	261	40	87.824	clear rejection

Table 1. Example results of χ^2 tests for the glitter patterns of Fig. 23. The displayed results are for U = 5 m/s and 2000 rays coming from a source at $\phi_s' = 180°$, with the indicated θ_s' values.

The results of testing H_o systematically for a variety of 2000-point glitter patterns are summarized in Fig. 24. In this figure cases of clear acceptance or rejection at the χ^2-test's $\alpha = 0.01$ level are indicated by "A" or "R" respectively. Borderline cases where $\chi^2 \approx \chi^2(\alpha,k-1)$, as was the case of Fig. 23b, are indicated by "B". This figure gives a rough idea of where the first-order theory is adequate. More extensive testing would have to be done in order to accurately fix the boundary line and in order to determine the weak dependence on ϕ_s' (all points in Fig. 24 are for $\phi_s' = 180°$, with some points recomputed for $\phi_s' = 90°$). We note from Fig. 24 that the first-order theory holds over a great range of θ_s' values for very low wind speeds, as expected, since the surface is then quite smooth and locally nearly level. However, for incident angles near $\theta_s' = 0$ (rays coming nearly straight down), the first order theory also holds for high wind speeds. This probably reflects the fact that only single-order scattering occurs for rays coming from near the zenith, even though the rms slopes at U = 20 m/s are of order $\zeta_u \sim 0.25$ so that $\zeta_u^2 \sim 0.06$. For nearly horizontal incident rays, first-order theory fails even at wind speeds of less than 1 m/s, for which the rms slopes are $\zeta_u \sim 0.05$ and $\zeta_u^2 \sim 0.003$. Presumably this failure of the first order theory is due to the effects of multiple scattering and shielding, which become important at low incident angles, even at low wind speeds (recall Fig. 12).

D. Application of first-order theory

Under conditions on $\underset{\sim}{\xi}'$ and U for which the first-order theory holds, one can simulate glitter patterns as follows. Suppose $\underset{\sim}{\xi}'$ and U are given. Then σ_u^2 and σ_c^2 are determined, and are related to U by means of (2.1) for the case of p = 1. Next, generate n (~2000) pairs (ζ_u,ζ_c) of normal random

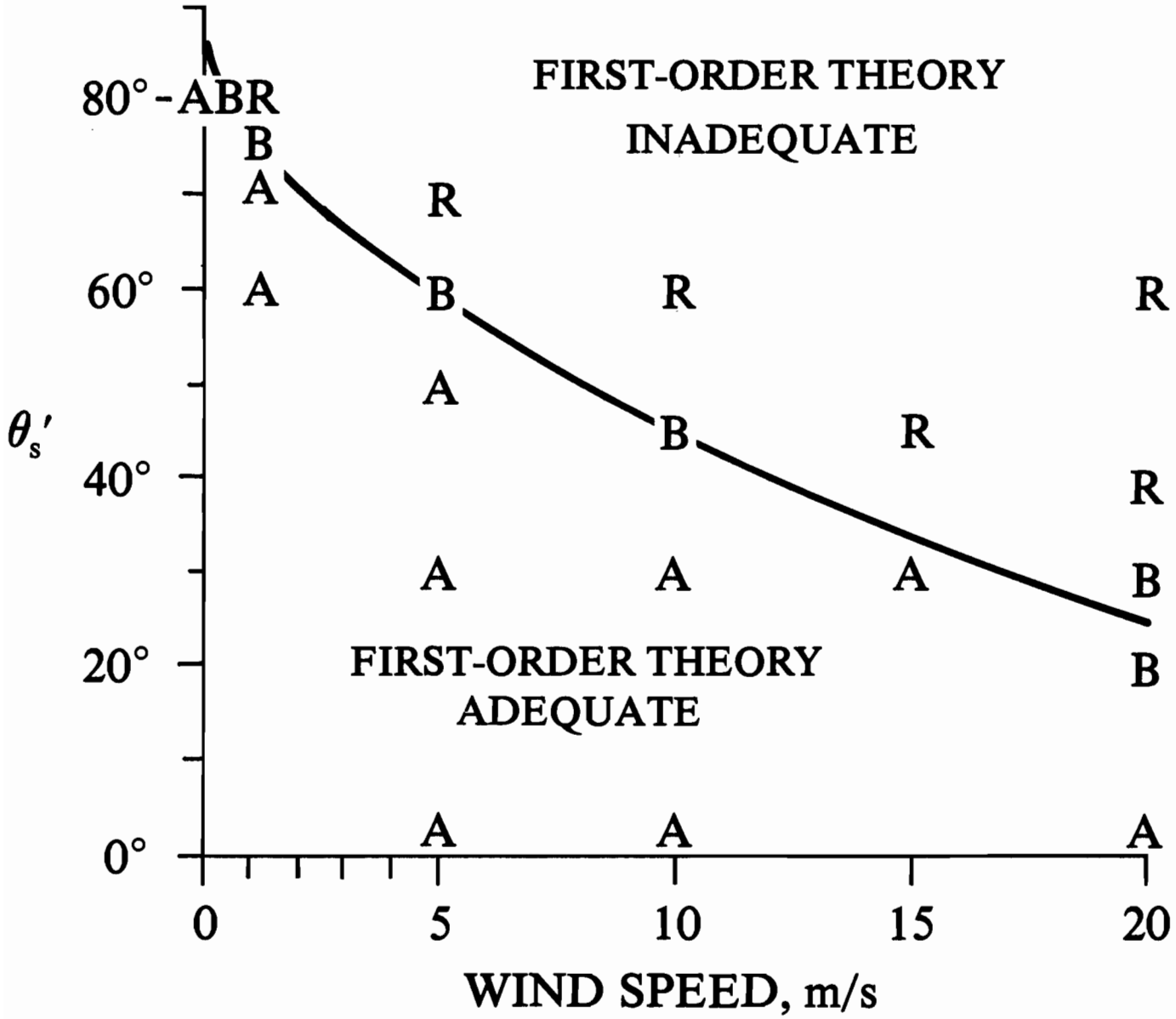

Figure 24.--The region of validity of first-order glitter pattern theory, according to χ^2 testing at the $\alpha = 0.01$ significance level. An "A" ("R") indicates clear acceptance (rejection) of H_o, and a "B" indicates borderline acceptance or rejection at the $\alpha = 0.01$ level. Generally, for a given θ_s', the first order theory is acceptable for winds from 0 up to some critical speed, beyond which it is not acceptable, as indicated.

variables by making n random independent selections from $N(0,\sigma_u^2)$ and $N(0,\sigma_c^2)$. For each of the n pairs (ζ_u,ζ_c), with ϕ' known from $\underset{\sim}{\xi}'$, compute the associated deflection plane pair $(\varepsilon_h,\varepsilon_v)$ using (7.12). A good simulation of a reflected glitter pattern for the air-incident case is obtained (when the model is valid) if one plots at the point $(\varepsilon_h,\varepsilon_v)$ in the deflection plane a dot whose radius is proportional to $r_-(\underset{\sim}{\xi}'\cdot\underset{\sim}{n})$, where $\underset{\sim}{n}$ is the wave facet normal given by (7.11). Note that the use of (7.12) imparts the correct "tilt" to the elliptical glitter pattern's major axis relative to the $\underset{\sim}{h}$-axis in the deflection plane, so as to account for the relative azimuths of the wind and sun angles.

When the first-order theory holds, the surface albedo r_- for arbitrary lighting conditions can be estimated in the following way. We begin as in the preceding glitter pattern simulation and generate $r_-(\underset{\sim}{\xi}'\cdot\underset{\sim}{n})$, as described above, for each of the 2000 pairs (ζ_u,ζ_c). These reflectances $r_-(\underset{\sim}{\xi}'\cdot\underset{\sim}{n})$ are the present method's counterparts to $r_-(\underset{\sim}{\xi}';\omega)$ in (4.8), $\omega = 1,\ldots,2000$. On averaging $r(\underset{\sim}{\xi}';\omega)$ over ω, we obtain the corresponding value $r_-(\underset{\sim}{\xi}')$. This in turn is used in (8.2), below in the form $r_-(\theta_s',\phi_s')$, where (θ_s',ϕ_s') are the location angles for the source giving rise to ray $\underset{\sim}{\xi}'$.

In general for each $\underset{\sim}{\xi}'$ we can make four first-order glitter patterns using $r_\pm(\underset{\sim}{\xi}'\cdot\underset{\sim}{n})$ or $t_\pm(\underset{\sim}{\xi}'\cdot\underset{\sim}{n})$ by adopting the four options outlined below (7.11). The theory of the three additional cases follows by suitably adopting that developed above for the air-incident reflectance case.

8. *Irradiance reflectances*

We now turn our attention to the primary goal of this study: the computation of the irradiance reflectance, or albedo, of the sea surface as a function of wind speed, light source distribution, and scattering order.

Before describing the results we remark on the performance of the Monte Carlo method. As is generally known, sampling variability in Monte Carlo experiments is a source of numerical uncertainty in the desired results. Initial experiments with the ray-tracing model revealed that albedos $r_{\pm}(\underset{\sim}{\xi}')$ computed from ensemble averages based on 3000 surface realizations (with one ray $\underset{\sim}{\xi}'$ per realization) are reproducible to within few percent of the desired magnitude for independent runs of 3000 realizations. Other possible sources of error, such as rays "lost" from the hexagonal grid, we find are completely negligible.

It should be noted that our reflectance results are those produced by infinitely distant single-direction light sources. The sun, while essentially infinitely distant, subtends a small but finite solid angle in the sky. There is therefore the possibility of error owing to the slight variation of the Fresnel reflectance for rays incident from different directions within the solar disk. A series of runs was made in which the incident rays $\underset{\sim}{\xi}'$ were randomly distributed within a solid angle equal to the sun's and centered at the sun-center direction $\underset{\sim}{\xi}_0'$. These finite-disk $r_-(\underset{\sim}{\xi}')$ results were compared with the point-disk $r_-(\underset{\sim}{\xi}_0')$ results. It was found that even for nearly horizontal angles of incidence, where the Fresnel reflectance varies the most, the difference between $r_-(\underset{\sim}{\xi}')$ and $r_-(\underset{\sim}{\xi}_0')$ was generally less than one percent. At wind speeds of 20 m/sec, the difference was at most a few percent. Thus there seems to be no need to consider the sun to be anything more than a point light source, unless extremely accurate results are required.

We are therefore confident that the albedos presented below are accurate to within 5%, for the assumed numerical model. The magnitude of errors due to physical processes not modeled, in particular the presence of whitecaps at higher wind speeds, and for polarized incident flux is not known. It is, however, likely that our results for unpolarized incident flux are quite accurate (to within a few percent) at low wind speeds, but may differ somewhat more from reality at very high wind speeds.

A. Albedos for capillary waves

We now discuss the computed albedos for a water surface covered by capillary waves. Figure 25 shows $r_-(\underset{\sim}{\xi}')$ (= $r_-(\theta_s',\phi_s')$) as a function of wind speed for selected θ_s' and ϕ_s' values. By symmetry, we find $r_-(\theta_s',\phi_s') = r_-(\theta_s', 180°-\phi_s')$, and $r_-(\theta_s',\phi_s') = r_-(\theta_s',-\phi_s')$, for $0° \le \phi_s' \le 360°$. Hence it is sufficient to determine $r_-(\theta_s',\phi_s')$ over the range $0° \le \phi_s' \le 90°$ for each θ_s'. Four curves are shown for each θ_s' value. The solid lines are for the alongwind case, $\phi_s' = 0$, in which the incoming rays are in the vertical plane parallel to the wind. The dashed lines are for the crosswind case, $\phi_s' = 90°$, in which the incoming rays are in the vertical plane perpendicular to the wind. In the computations a separate tally was kept for singly-scattered rays, so that the effects of multiple scattering could be isolated. For each pair of solid or dashed curves, the top curve gives the total albedo computed from all rays and the bottom curve gives the albedo as computed from singly scattered rays only. Most points on the curves of Fig. 25, above each labelled wind speed, are the average of three separate experiments (with 3000 surface realizations per experiment). Spot checks of the accuracy of these curves show that they are within a few percent of the true values (as defined by an infinite number of surface realizations). For example, for the

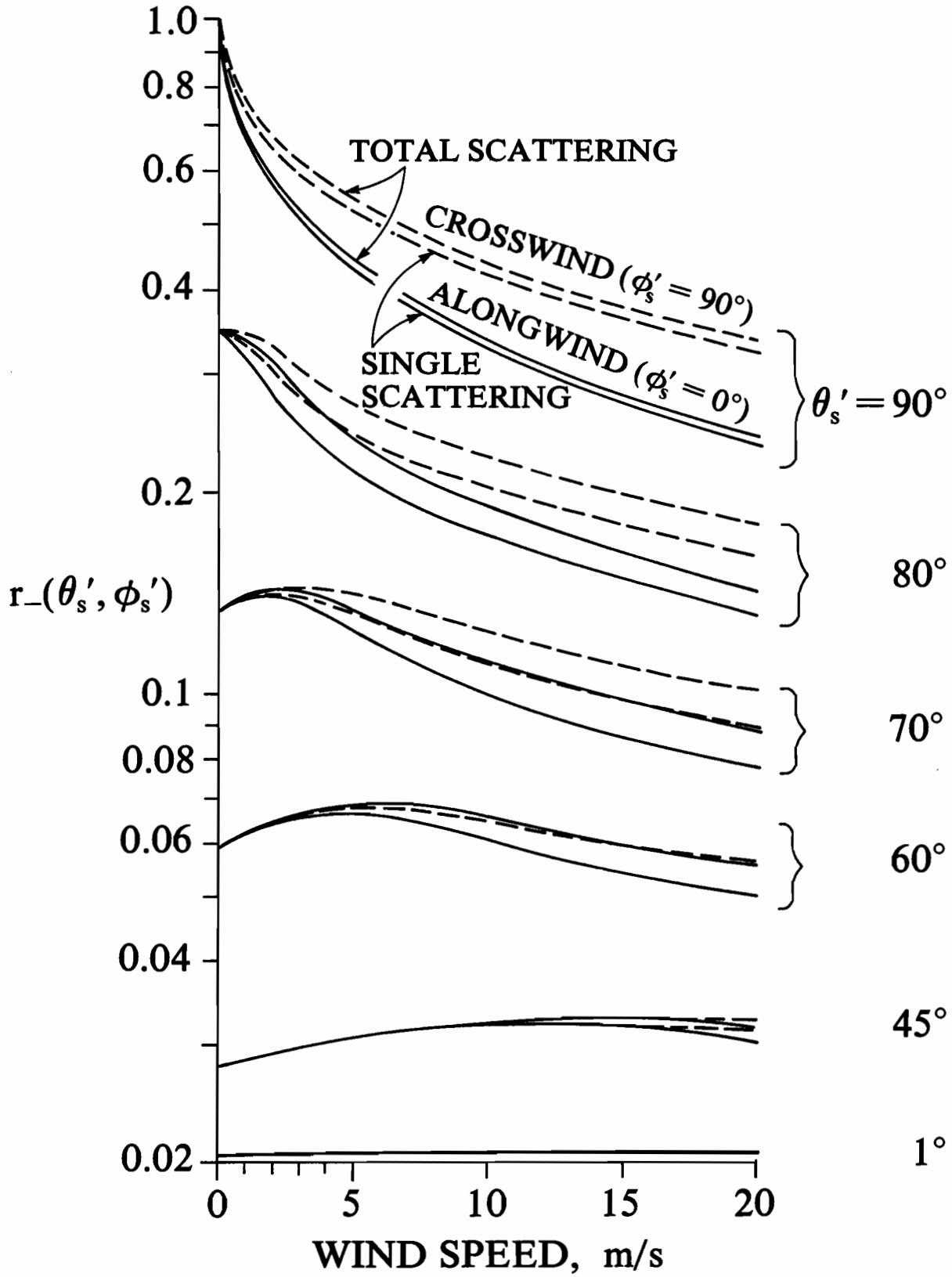

Figure 25.--Albedos (i.e., irradiance reflectances) $r_-(\theta_s', \phi_s')$ for random capillary waves, and air-incident light rays from distant point sources. For each group of θ_s'-curves, the solid lines are for $\phi_s' = 0$ (sun and wind along same direction) and the dashed curves are for $\phi_s' = 90°$ (light source at right angles to wind direction). For each pair of solid or pair of dashed curves, the top curve is for total scattering and the bottom curve is for single scattering only.

alongwind total scattering case of U = 20 m/s with $\theta_s' = 60°$, five experiments (of 3000 realizations each) yielded an average $r_-(\xi')$ value of 0.05456, with a standard deviation of 0.00053. For the same situation except for $\theta_s' = 80°$, the five experiment average yielded $r_-(\xi') = 0.14045$ with a standard deviation of 0.00128. Two of these standard deviations on each side of the curves will define points that are only slightly more separated than the drawn thickness of the curves. According to standard statistical reasoning, we are 95% confident that the true mean values lie between these points.

The albedos for zero wind speed in Fig. 25 are of course just the Fresnel reflectance of a horizontal plane surface (index of refraction m = 4/3) for the given θ_s'. For high solar altitudes (i.e. small θ_s'), the albedo increases slightly as the wind increases from zero, whereas for low solar altitudes, the albedo decreases markedly as the wind picks up. In polar regions of the earth, low-sun power input to the ocean increases with wind speed. This qualitative behavior was predicted by Cox and Munk (1955) from approximate analytic calculations. The present study reveals in detail the quantitative features of this behavior, in particular the effects of wave anisotropy and multiple scattering.

A detailed view of the dependence of $r_-(\theta_s', \phi_s')$ on the azimuth angle ϕ_s' of the source relative to the wind direction is shown in Fig. 26. This figure gives the total-scattering albedo at a wind speed of 20 m/s for capillary waves. Since the wave facets are slightly less tilted, on average, in the crosswind direction than in the alongwind direction (recall $\sigma_u^2 > \sigma_c^2$ in (2.1) for p = 1), rays incident at right angles to the wind see a slightly flatter water surface, and thus have a slightly higher albedo. This behavior is seen in Fig. 26. The dependence is very weak at high sun altitudes (small θ_s') but becomes substantial for incident angles near the horizon.

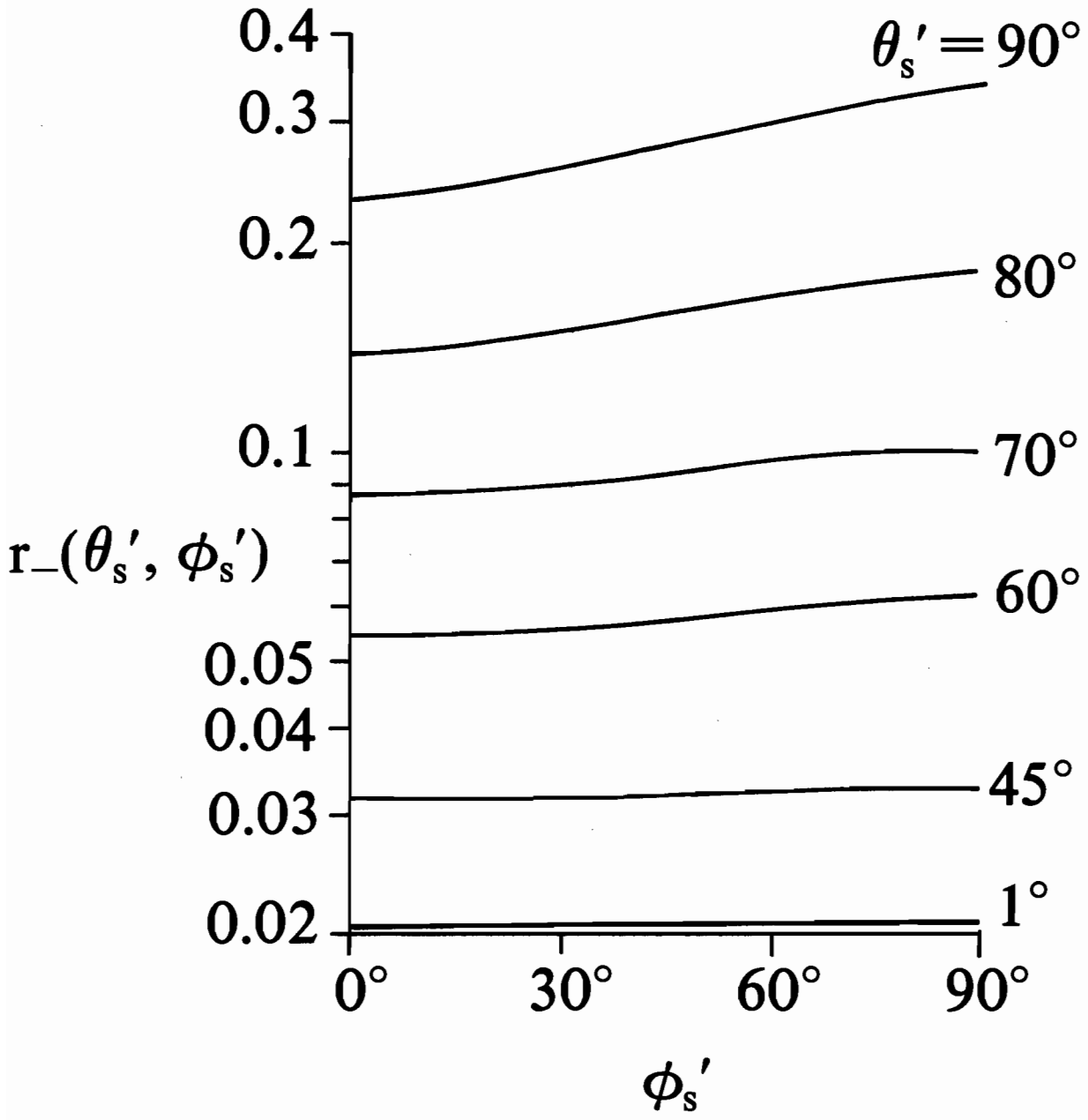

Figure. 26.--Dependence of capillary-wave albedo $r_-(\theta_s', \phi_s')$ (including all scattered rays) on light source position relative to wind direction, for a wind speed of U = 20 m/s.

Figure 27 reproduces in different form the total scattering curves of Fig. 25 for the alongwind case, $\phi_s' = 0$. The form of Fig. 27 is more convenient if the albedo is desired for intermediate θ_s' values.

The albedos for an underwater light source, $r_+(\underset{\sim}{\xi}')$ (= $r_+(\theta_s', \phi_s')$), are shown in Fig. 28. Now θ_s' is measured from the nadir to the source location. The arrangement of the curves (alongwind, crosswind, total and single scattering) is analogous to that for the air-incident case in Fig. 25. However, the curves are strikingly different from their counterparts in Fig. 25 because of the effects of total internal reflection. For the specular surface at zero wind speed, any water-incident ray with $\theta_s' \geq \arcsin(1/m) = 48.59°$ (cf. (3.19)) is totally reflected, giving an albedo of 1. The albedo increases quite rapidly as this limit is approached, and of course is constant thereafter. As soon as the wind increases from U = 0, rays incident at $\theta_s' = 48.59°$ begin hitting tilted facets and sometimes experience only partial reflection; the albedo then drops sharply for this θ_s' value. Rays water-incident at angles near the horizon are almost always totally reflected even at high wind speeds, so $r_+(\underset{\sim}{\xi}')$ remains extremely close to 1 at these angles. For angles of incidence $\theta_s' \lesssim 45°$ there is a strong dependence on θ_s', unlike the air-incident case of Fig. 25. We see that increasing wind speed now causes a rapid increase in the albedos, with the alongwind values now generally being greater than the crosswind values. Comparing the curves for total and single scattering shows that multiply-scattered rays often make a substantial contribution to the albedo. The curves for total scattering are for white* convexification ($\alpha = 0$ in (4.5)). The curves for single scattering are in essence the black* convexification case ($\alpha = \infty$ in (4.5)), since almost

* These convexification concepts are used in Preisendorfer (1965, pp. 77, 100) to formulate the application of invariant imbedding ideas to disconnected and concave optical media. Here, these concepts help organize the single and multiple scattering results.

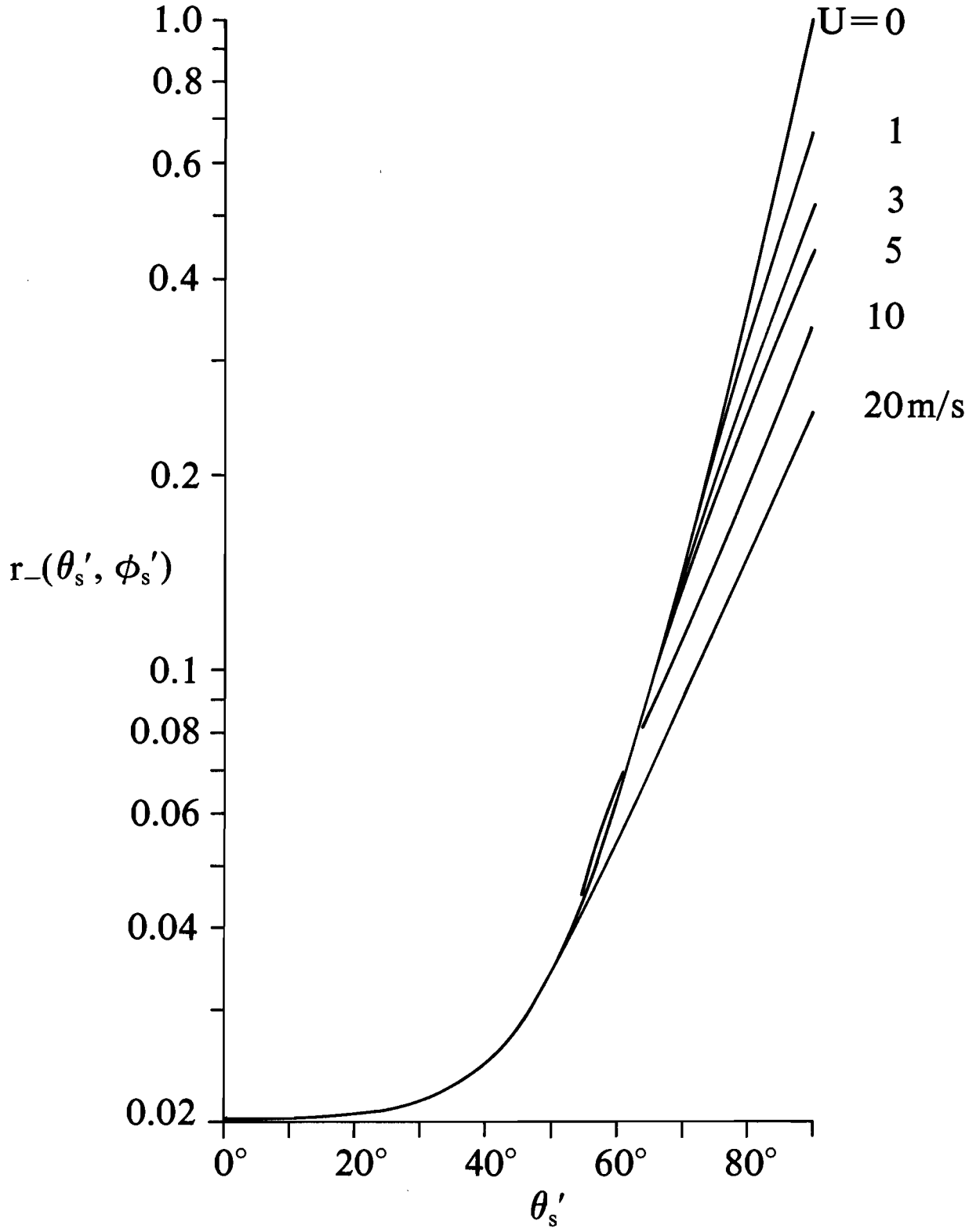

Figure 27.--Albedos as a function of wind speed and θ_s', for $\phi_s' = 0$ and a random capillary wave surface (replots of the upper solid curve of each solid pair in Fig. 25).

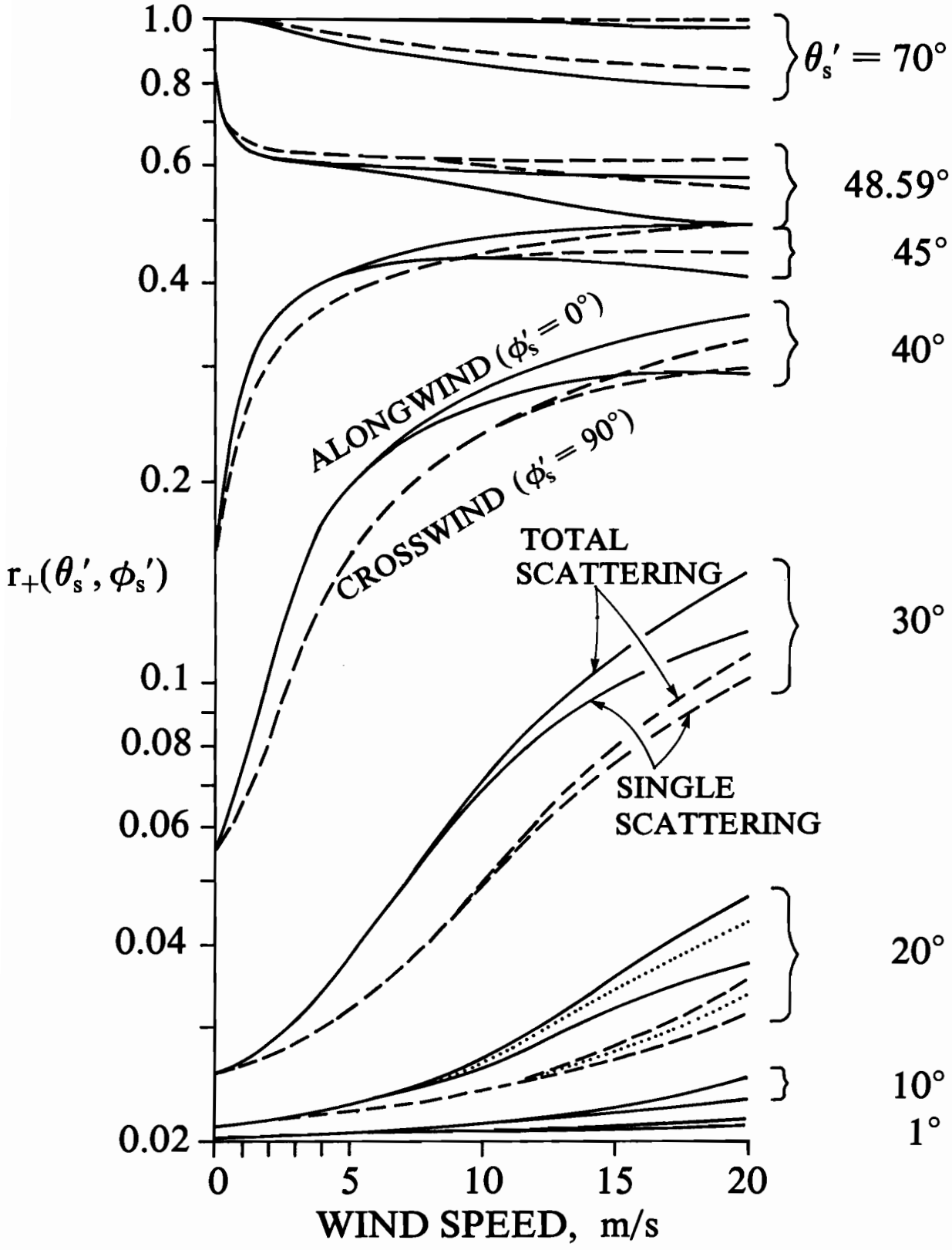

Figure 28.--Albedos (i.e., irradiance reflectances $r_+(\theta_s', \phi_s')$ for random capillary waves and for water-incident light rays from distant point sources. θ_s' is measured from the nadir to the source location. The solid and dashed line conventions are as in Fig. 25, and the dotted curve for $\theta_s' = 20°$ shows the grey convexification result for $\alpha = 0.5$ m^{-1} (see text).

all possibilities for multiple scattering of water-incident rays are then eliminated (recall the $n_s = 2$, $n_b = 4$ case of Fig. 11 which is ruled out in black convexification). A case of "grey convexification" with $\alpha = 0.5$ m^{-1} is shown by the dotted lines in the $\theta_s' = 20°$ curves. (Since α is in units of meters^{-1}, $\delta = 1$ in (2.12) has units of meters for interpreting the dotted lines.) This serves to show that in practical calculations such as the present one, the optical properties of a random surface cannot be fully separated from those of the medium it bounds.*

Figure 29 replots selected total scattering curves (solid) from Fig. 28 in order to better show the dependence of $r_+(\underset{\sim}{\xi}')$ on θ_s'. A grey convexification curve (dotted) with $\alpha = 0.5$ m^{-1} and the black convexification curve (dashed) are shown for a wind speed of 20 m/s. The steep slopes of these curves for the 20 m/s case show the importance of including multiple scattering in the r_+ estimates. The remaining solid curves are for total scattering, alongwind cases for the U = 3 m/s and U = 0 wind speeds shown.

The point source albedo $r_-(\underset{\sim}{\xi}')$ is a reasonable approximation to nature for the case of the sun in a clear sky. Likewise $r_+(\underset{\sim}{\xi}')$ applies to a bright unidirectional horizontally extensive light source just under the surface. However, in the air-incident case, if the sky is overcast the position of the sun may be indiscernible, so that an extensive diffuse light source must be used in the calculations. Depending upon the exact form of the continuous radiance distribution over the appropriate hemisphere of incident directions, the albedo for a diffuse source is in essence a weighted average of the point-source albedos presented above. Albedos for diffuse light sources can be

---

* The analytic approach to random air-water surface reflectance calculations, as described in *H.O.* vol. VI, sec. 12.0-12.14, handles this separation problem in a satisfactory way. However, no numerical tests of the analytic approach have been made.

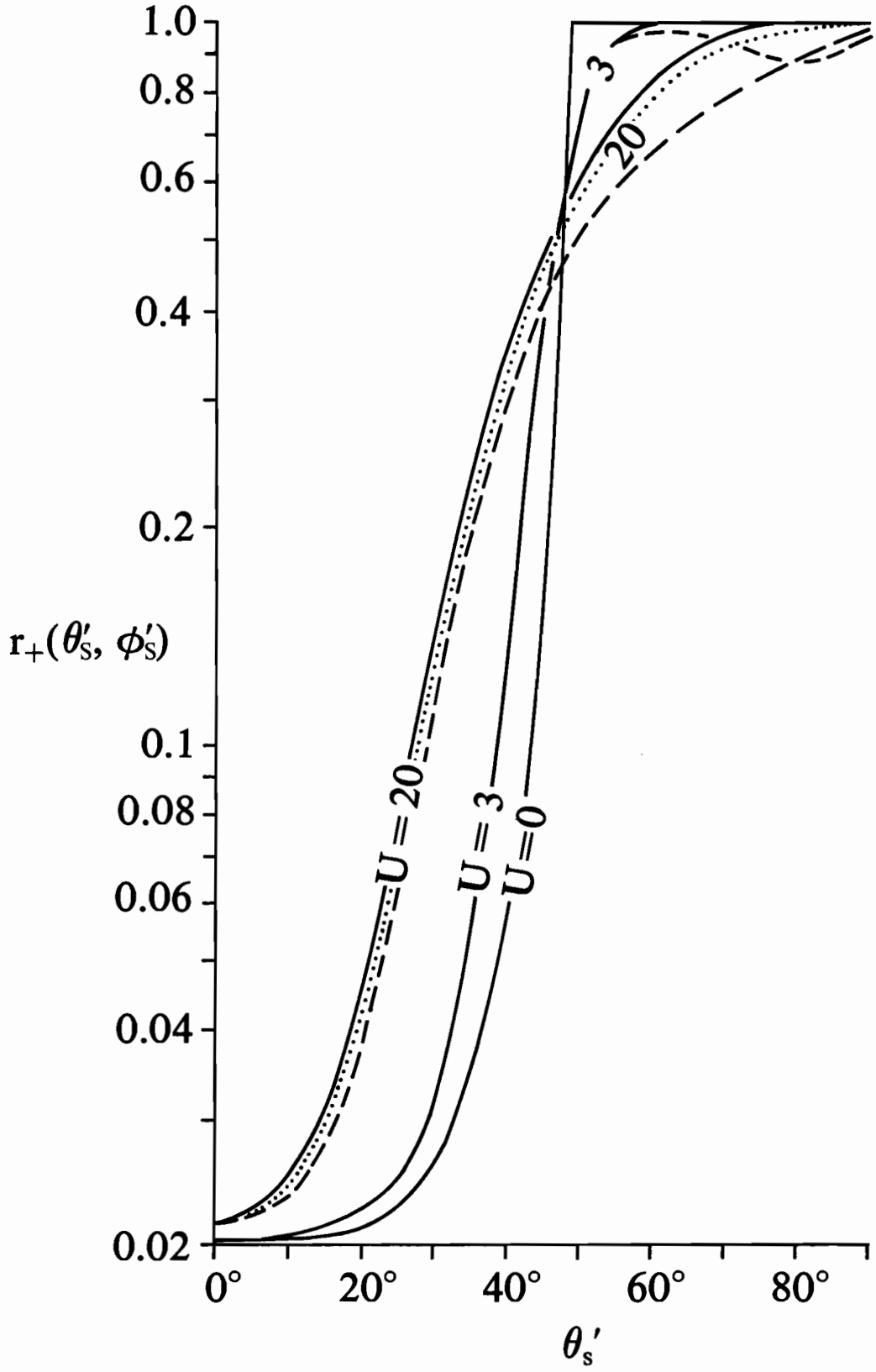

Figure 29.--Selected albedos $r_+(\theta'_s,\phi'_s)$ replotted from Fig. 28. The solid curves are for the alongwind total scattering cases for the wind speeds shown.

computed with the Monte Carlo ray tracing model by simply allowing the incoming ray directions to be distributed according to the desired radiance distribution. For example, an albedo for a uniform sky could have $\underset{\sim}{\xi}'$ values chosen at random such that each point in the dome of the sky is equally likely to be the source direction of the ray. We can expect that at least several tens of thousands of rays would need to be traced in order to get accurate albedos for diffuse sources. Rather than expending the considerable computational effort required for computing diffuse source albedos by direct ray tracing, we now describe a method which makes use of the point source albedos already computed.

A convenient parameterization for diffuse lighting in nature is the *cardioidal radiance distribution* (cf. *H.O.* vol. VI, p. 21):

$$N(\underset{\sim}{\xi}') \equiv N(\theta',\phi') \equiv N_0(1 + c\cos\theta') \tag{8.1}$$

where N_0 is the radiance of the horizon ($\theta' = 90°$), and c is a real parameter. For the case of a heavy overcast, observations indicate that $c = 2$, which summarizes the fact that on such a day the sky at the zenith ($\theta' = 0$) is three times as bright as the sky at the horizon. A sky over which N is uniform is given by $c = 0$. For water-incident rays, values of c in the range $-0.9 \leq c \leq -0.8$ are representative of the range of upwelling radiance distributions observed in natural waters, where θ' in (8.1) is now measured from the nadir. Thus a submerged skin diver looking toward his horizon may see five to ten times the brightness (radiance) that he sees looking straight down into the depths. That the subsurface horizon is much brighter than the nadir is a consequence, among other things, of the total internal reflection of rays which are incident on the bottom side of the water surface from nearly

horizontal directions. (Another reason may be based on the large ratio of forward to backward scattering values of the volume scattering function of lakes and seas.)

The albedo for a continuous radiance distribution is (*H.O.* VI, p. 17)

$$r_{\pm} = \frac{\int_0^{2\pi} \left[\int_0^{\pi/2} N(\theta',\phi')\, r_{\pm}(\theta',\phi') \cos\theta' \sin\theta' \, d\theta' \right] d\phi'}{\int_0^{2\pi} \left[\int_0^{\pi/2} N(\theta',\phi') \cos\theta' \sin\theta' \, d\theta' \right] d\phi'} .$$

Here $r_{\pm}(\theta',\phi')$ is the Monte Carlo produced point source albedo, and $r_{\pm}$ is the corresponding albedo for a continuous radiance distribution over the appropriate hemisphere. Substituting (8.1) for $N(\theta',\phi')$ and integrating gives

$$r_{\pm} = \frac{12}{(2c+3)\pi} \int_0^{\pi/2} \left[\int_0^{1} (1 + c\mu')\mu' \, r_{\pm}(\mu',\phi') \, d\mu' \right] d\phi' \qquad (8.2)$$

after letting $\mu' \equiv \cos\theta'$. The integral (8.2) can be numerically evaluated using the Monte Carlo-generated point source values $r_{\pm}(\theta',\phi')$ ($\equiv r_{\pm}(\mu',\phi')$) which were used to draw Figs. 25-29. Figure 30 shows the non-uniform grids of μ'-ϕ' values (a for air-incident, b for water-incident rays) for which these albedos are available from the previous Monte Carlo simulations. By azimuthal symmetry of $r_{\pm}(\mu',\phi')$, the integration in (8.2) need only be over a quarter hemisphere. A bicubic spline was used to fit a continuous function to the available $r_{\pm}(\mu',\phi')$ values (IMSL routine IQHSCV). This continuous function was then used to define $r_{\pm}(\mu',\phi')$ values on a regular grid of 21μ' by 21ϕ' values (i.e. $\mu' = 0.0, 0.05, \ldots, 1.0$ and $\phi' = 0, \pi/40, \ldots, \pi/2$). Using these values, the integrand of (8.2) was evaluated on the uniform 21 × 21 grid, and

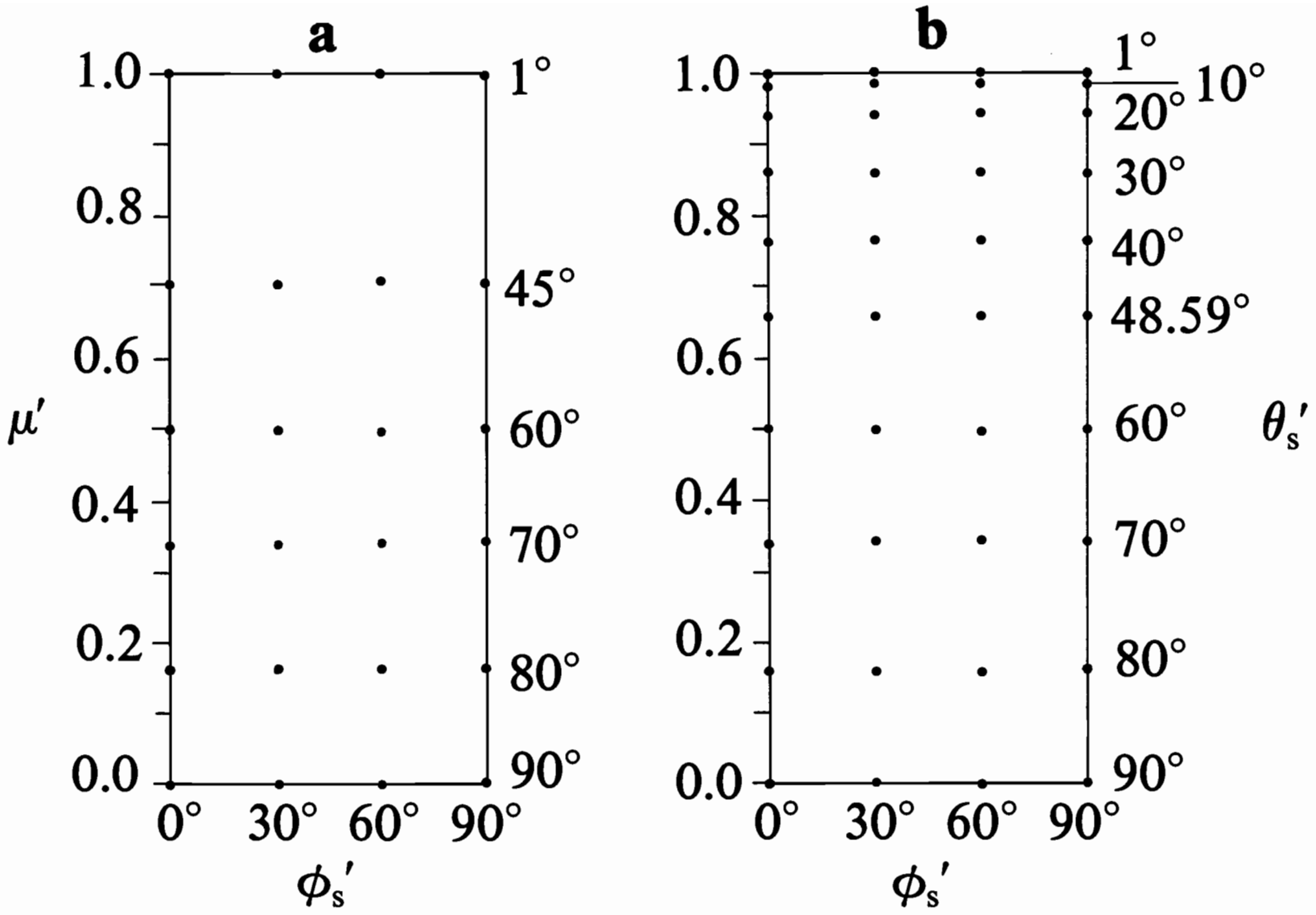

Figure 30.--The μ'-φ' grids for which the albedos were computed. The albedo $r_-(\mu',\phi')$ is known at the 24 designated points of (a), and $r_+(\mu',\phi')$ is known at the 40 points of (b). In (a) source location angles are measured from the zenith; in (b) the angles are measured from the nadir.

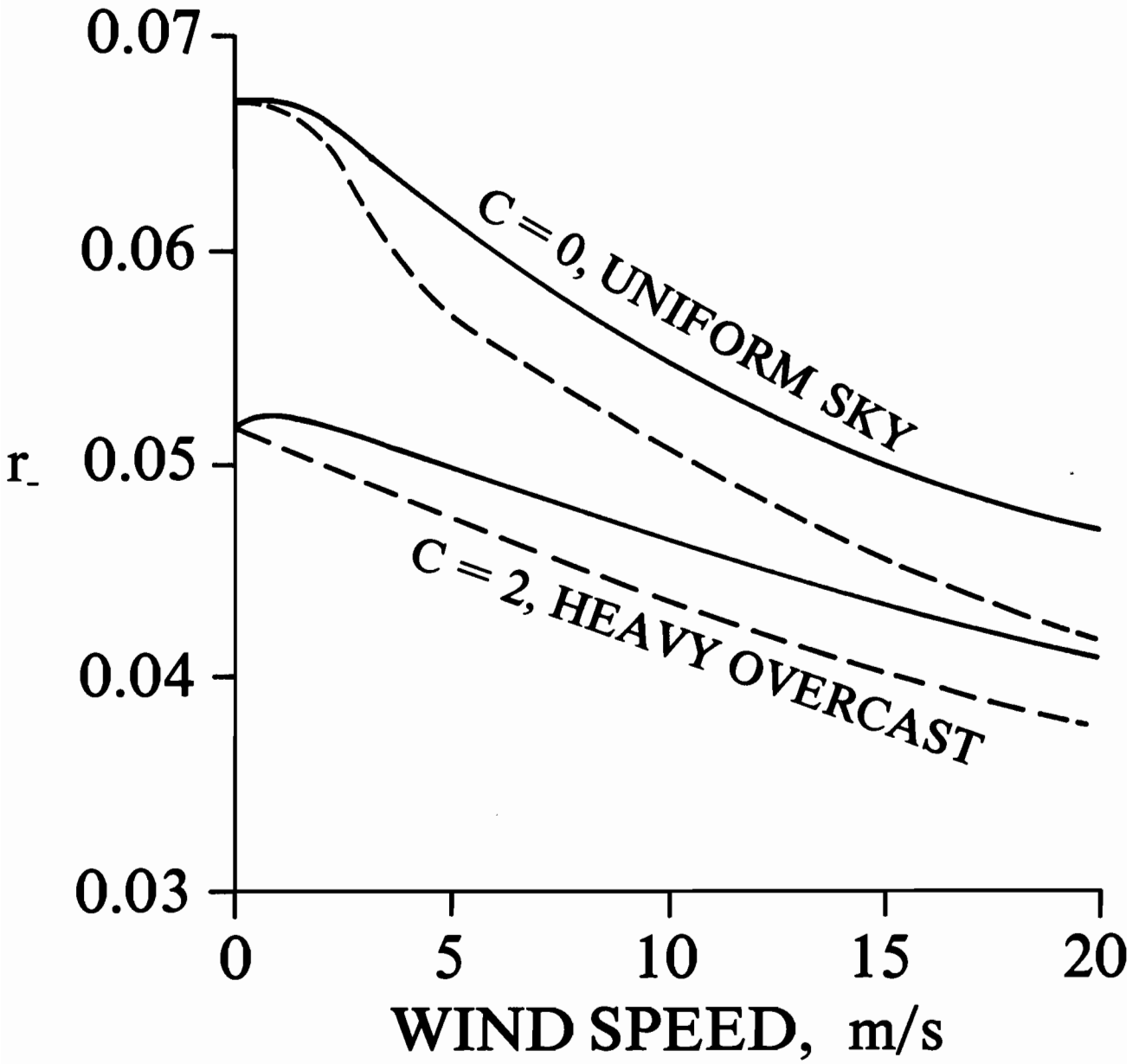

Figure 31.--Albedos r_ for continuous radiance distributions over the sky hemisphere. Solid lines are for total scattering and dashed lines are for single scattering only.

numerically integrated after fitting another set of bicubic splines to the integrand values (IMSL routine DBCQDU).

Figure 31 shows the albedo r_- (an irradiance reflectance) for uniform sky and heavy overcast conditions. The results for total (solid curve) and single scattering (dashed curve) were computed by using the corresponding values of $r_-(\underset{\sim}{\xi}')$ in (8.2). For the case of no wind, $r_-(\underset{\sim}{\xi}')$ is the Fresnel reflectance function and (8.2) can be integrated analytically (cf. *H.O.*, vol. VI, p. 26) to give $r_-(c=0) = 0.0665$ and $r_-(c=2) = 0.0513$ for the index of refraction $m = 4/3$. The values computed by the bicubic spline integrations are respectively $r_-(c=0) = 0.0669$ and $r_-(c=2) = 0.0519$ at $U = 0$. These comparisons indicate that the bicubic spline integration of (8.2) using the available point source albedos does not introduce any significant errors into the r_- values. We see that in general that the albedos decrease with increasing wind speed and that the contribution by multiply scattered rays is significant at 5 m/s and above.

The diffuse light albedos for water-incident rays are shown in Fig. 32 for a variety of upwelling subsurface radiance distributions. Solid curves are for total scattering, dashed curves are for single scattering. Dotted curves are for grey-convexification, with $\alpha = 0.5\ m^{-1}$. For $U = 0$ and a uniform distribution ($c=0$), Judd (*H.O.* vol. VI, p. 19) numerically estimated the value $r_+(c=0) = 0.472$ for $m = 4/3$. Our integration of (8.2) for $U = 0$ yields $r_+(c=0) = 0.486$, a difference of about 3%. We see that both for uniform ($c=0$) and natural lighting conditions ($c = -0.7, -0.8, -0.9$), the total r_+ is only weakly dependent on wind speed in the white convexification (total scattering, solid curve) case, but is about an order of magnitude greater than r_-. The observed dip in r_+ at low wind speeds reflects the net effects of the relative importance for different θ_s' of the rapidly changing

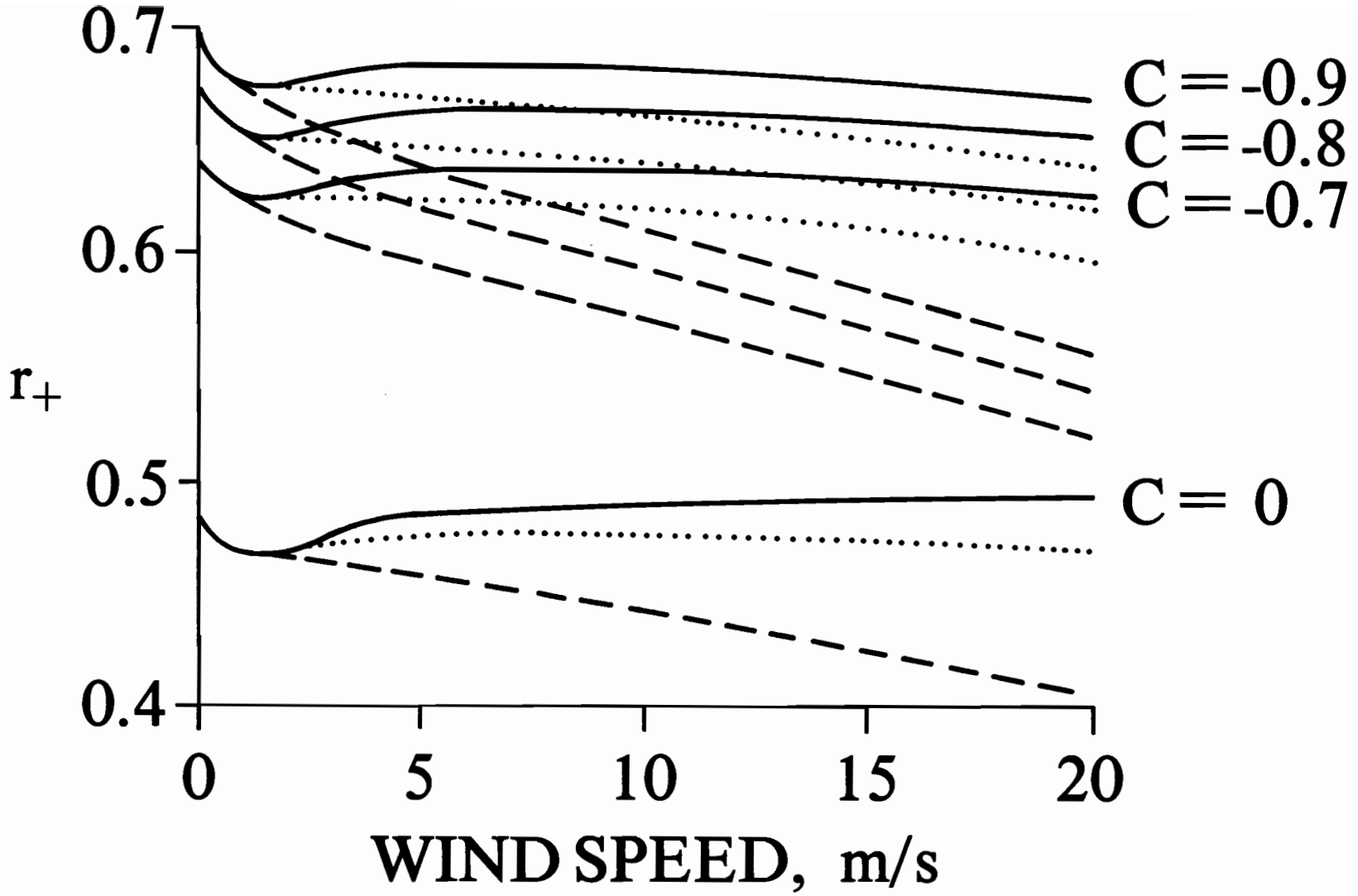

Figure 32.--Albedos r_+ for continuous radiance distributions over the sea hemisphere. Solid lines are for total scattering and white convexification (see text); dotted lines are for total scattering and grey convexification with $\alpha = 0.5\ m^{-1}$; dashed lines are for single scattering only, the equivalent of black convexification.

values of $r_+(\theta_s', \phi_s')$ seen in Fig. 28. For the single scattering (or black convexification) case, there is a significant decrease of r_+ with wind speed.

B. Albedos for fully developed seas

We now examine some possible extensions of the present approach to albedos of fully developed seas.

The optical description of the sea state by the capillary wave statistics is a good approximation to nature particularly for seas freshly activated by winds. However it is to be expected that the optical properties of a fully developed sea, over which for long times and extensive fetches the wind has been active, may be affected by the presence of the resultant gravity waves. In particular, at low solar altitudes the effects of wave shielding may become important, since the incoming rays will tend to strike the "frontsides" of the large gravity waves while their "backsides" remain in shadow.

A simple hybrid or mixed wave model is possible that will combine capillary and gravity waves. We first construct the gravity wave swells over a rectangular gridwork using the air-water surface representations in Appendix A. This defines a set of *gravity wave facets*. The capillary hexagonal grid of section 2 is then fitted to each gravity wave facet. Shielding by the gravity waves can then be thought of as a change in the incoming ray direction relative to the capillary waves riding on the gravity wave facet. Thus when a ray strikes a gravity wave facet which is tilted toward the sun, the capillary waves on that facet see the sun as being "higher in the sky" relative to the plane of their gravity wave facet. It was this observation which suggested the simple technique for combining gravity and capillary waves which is discussed in Appendix B. We now briefly review the results of this approach.

Let $\underset{\sim}{n}$ be the surface normal of the gravity wave facet which has intercepted an incoming ray $\underset{\sim}{\xi}'$, and let $\theta_c' \equiv \arccos(\underset{\sim}{\xi}' \cdot \underset{\sim}{n})$ be the equivalent zenith angle for capillary waves on the gravity wave facet. That is, a tiny observer of the gravity wave facet would see $\underset{\sim}{\xi}'$ come in at the angle θ_c' from local zenith. For a flat horizontal surface, $\underset{\sim}{n} = \underset{\sim}{k}$ and $\theta_c' = \arccos(\underset{\sim}{\xi}' \cdot \underset{\sim}{k}) = \theta'$, the zenith angle of the incoming rays. Figure 33 shows the average (over thousands of incident rays $\underset{\sim}{\xi}'$) of θ_c' as a function of wind speed. This figure gives us an idea of when shielding is important. For incident angles of $\theta_s' \leq 60°$, there is little shielding over the indicated wind speed range from 0 to 20 m/s, and so the incoming rays are rarely intercepted in their way to the target facet; the average θ_c' is therefore equal to θ_s'. For rays incident from nearer the horizon, shielding becomes noticeable at the higher wind speeds. Thus at sunset ($\theta_s' = 90°$) the capillary waves on the gravity waves see a solar position which on average is around 10° above their horizon (i.e. $\theta_c' \approx 80°$) at a wind speed of 20 m/s.

The results in Fig. 33 are based on the ideas outlined in Appendixes A and B where we visualize the capillary waves riding "piggy-back" on the gravity wave facets. In some preliminary numerical studies of this approach to the optical properties of mixed capillary-gravity waves we found that the curves in Fig. 33 depend on the scale of resolution of the gravity wave facets: finer resolution of the facets causes the curves to drop a bit faster with wind speed. Curves of the kind in Fig. 25 were also produced and appeared to depend on resolution scales as well as wind speed. This means that the finer choppiness of the water surface is being reproduced in the finer-scaled surface representation. The result is to generate more facet tilt, on average, toward the incoming ray $\underset{\sim}{\xi}'$, and hence smaller reflectances for near horizontal incident rays. However, increased resolution requires

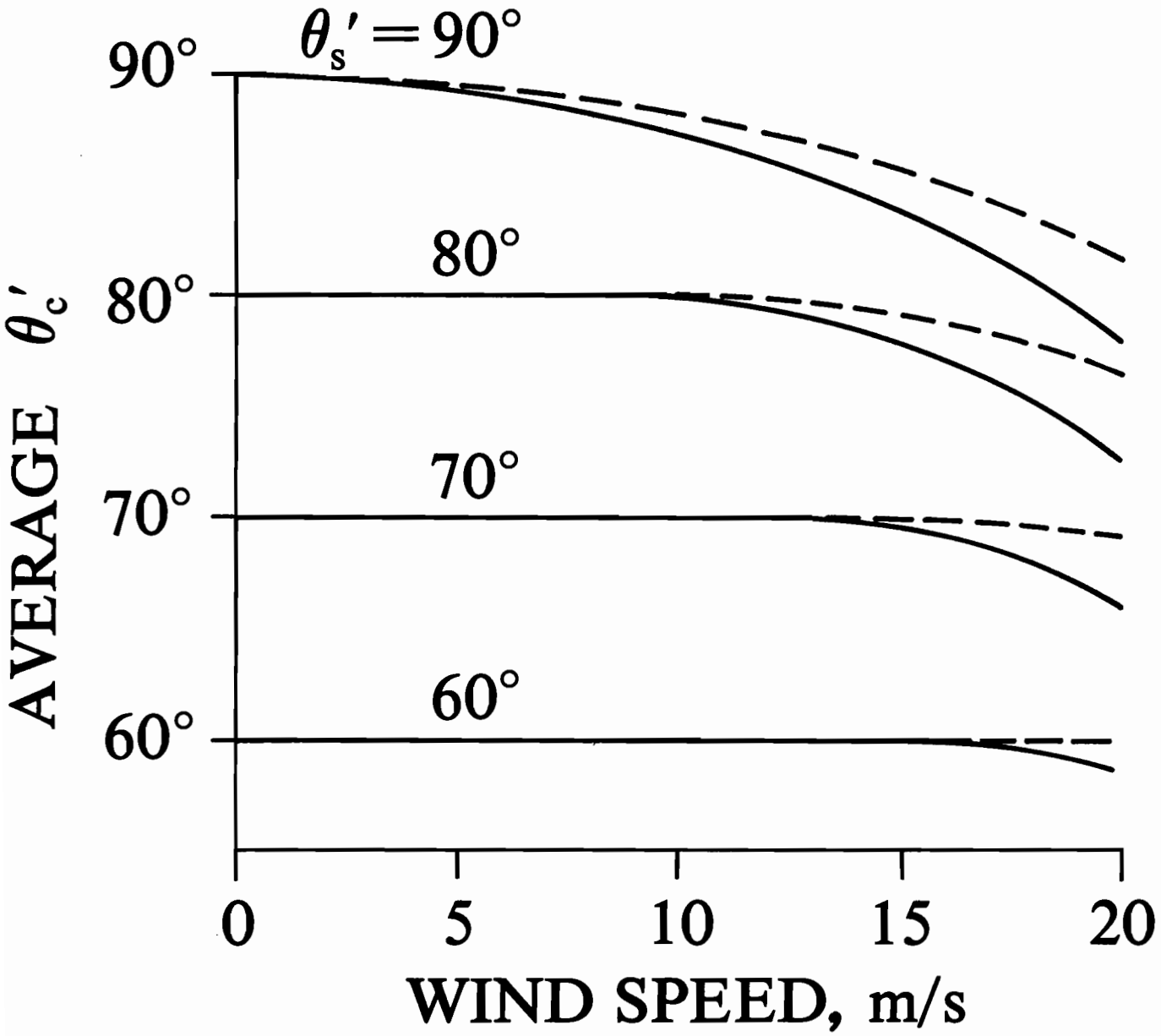

Figure 33.--The average equivalent polar angle θ_c' as function of wind speed and actual polar angle θ_s'. Solid lines are for $\phi_s' = 0$, and dashed lines are for $\phi_s' = 90°$.

increased computer costs, and to explore this mixed wave problem further would have been prohibitively expensive. Further, the "piggy-back" approach is at best a temporary expedient. The conceptually correct approach, the one which would be worth extensive exploration on the computer, is set up in Appendix C for future reference. In this approach one starts with a complete power spectrum of the surface which contains capillary as well as gravity spatial frequencies. From the spectrum a differentiable sea surface realization may be constructed. A simple modification of the flow diagram of Fig. 2 to this new kind of representation provides the basis for a computer program that would extend the results in Figs. 19-33 above to a fully arisen, random, wind-roughened sea.

9. *Appendixes*

A. Constructing Gravity Wave Surfaces

In order to extend the Monte Carlo procedure of this study from capillary to gravity waves, we now consider the problem of constructing realizations of random gravity wave surfaces.

As in the capillary wave case, the random gravity wave surface will be spatially stationary. We can use the well-known Neumann spectrum or its modern counterparts to construct the random surface.

A rectangular wind-based coordinate system for gravity waves on the sea surface is shown in Fig. 34. The horizontal plane of the system rests at mean sea level. The region covered is 2X by 2Y meters and the x-axis lies alongwind. The distances 2X and 2Y are divided respectively into 2ℓ and 2m equal parts, forming a gridwork of alongwind and crosswind coordinate lines, of spacings $\Delta x = X/\ell$ and $\Delta y = Y/m$. A point (or node) on the gridwork is located by the pair of integers (x,y), $-\ell \le x \le \ell$, $-m \le y \le m$. The ωth realization $S(\omega)$ of a spatially stationary, zero-mean random surface $S = \{S(\omega): \ \omega = 1,\ldots,r\}$ over this gridwork is defined by a function z whose value at node (x,y) is

$$z(x,y;\omega) = \sum_{(u,v)\in W} [b_{uv}(\omega) \cos 2\pi(\frac{ux}{p} + \frac{vy}{q}) + c_{uv}(\omega) \sin 2\pi(\frac{ux}{p} + \frac{vy}{q})]$$

$$-\ell \le x \le \ell, \quad -m \le y \le m, \quad \omega = 1,\ldots,r \qquad (A.1)$$

$$W = \{(u,v): \ (u=0 \text{ and } v\in[1,m]) \text{ or } (u\in[1,\ell] \text{ and } v\in[-m,m])\}$$

$$p = 2\ell+1, \quad q = 2m+1 \ .$$

Here b_{uv} and c_{uv} are independent normal random variables of zero mean and variances

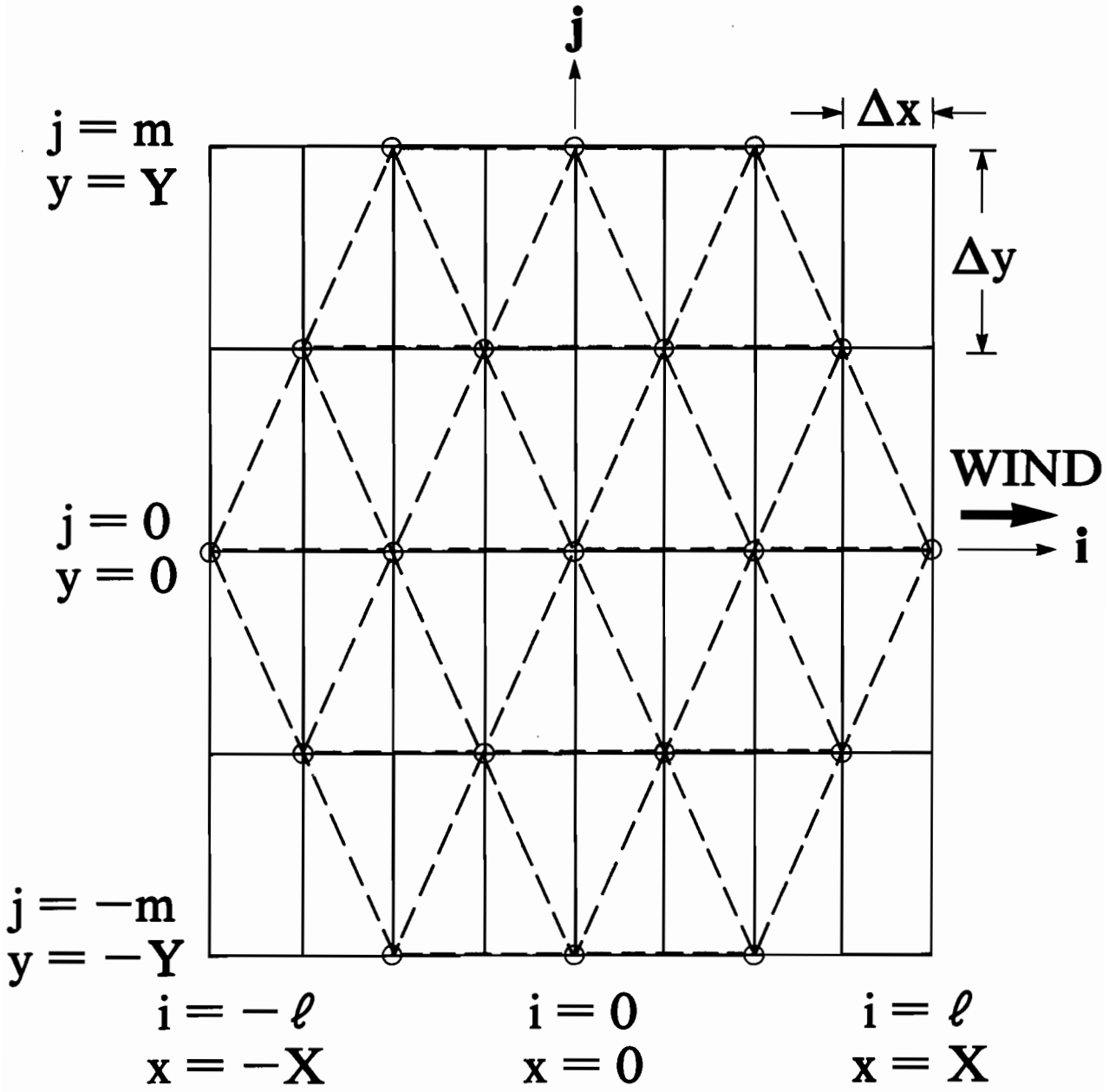

Figure 34.--The coordinate system for constructing a discrete random air-water surface. [Spatial domain for Fig. 35.]

$$E\{b_{uv}^2\} = E\{c_{uv}^2\} = E(k_u,k_v)\Delta u\Delta v \ . \qquad (A.2)$$
$$(u,v)\varepsilon W$$

Here $\Delta u = 2\pi/p\Delta x$, $\Delta v = 2\pi/q\Delta y$, and $E(k_u,k_v)$ is, for example, Neumann's gravity sea wave spectrum in rectangular coordinate form, with the symmetry $E(-k_u,-k_v) = E(k_u,k_v)$, and where $k_u = u\Delta u$, $k_v = v\Delta v$. The spectral domain containing W is shown in Fig. 35, and describes all wave trains moving generally downwind. By the symmetry of $E(k_u,k_v)$ shown above, W covers all useable wave trains.

The requirement (A.2) comes about as follows. We want the set of random variable values $z(x,y;\omega)$, $\omega = 1,\ldots,r$, to be spatially stationary over the gridwork and with variance at each (x,y) in the gridwork given by

$$E\{z^2(x,y)\} = \sum_{u=-\ell}^{\ell} \sum_{v=-m}^{m} E[k_u,k_v]\Delta u\Delta v \ . \qquad (A.3)$$

This is the requirement that the variance of the random sea surface (at each point (x,y)) be given by the sum of the spectral components over all spatial frequencies (cf. *H.O.* vol. VI, p. 120, Eq. (82)). Returning to (A.1), squaring each side and applying the ensemble average operator E, we find, by the independence of b_{uv} and c_{uv}, that

$$E\{z^2(x,y)\} = \sum_{(u,v)\varepsilon W} (E\{b_{uv}^2\} + E\{c_{uv}^2\}) \ . \qquad (A.4)$$

By construction, the variances of b_{uv} and c_{uv} for each (u,v) pair over W are to be equal, and since W covers the downwind half the (u,v) domain (cf. Fig. 35) the requirement (A.2) follows.

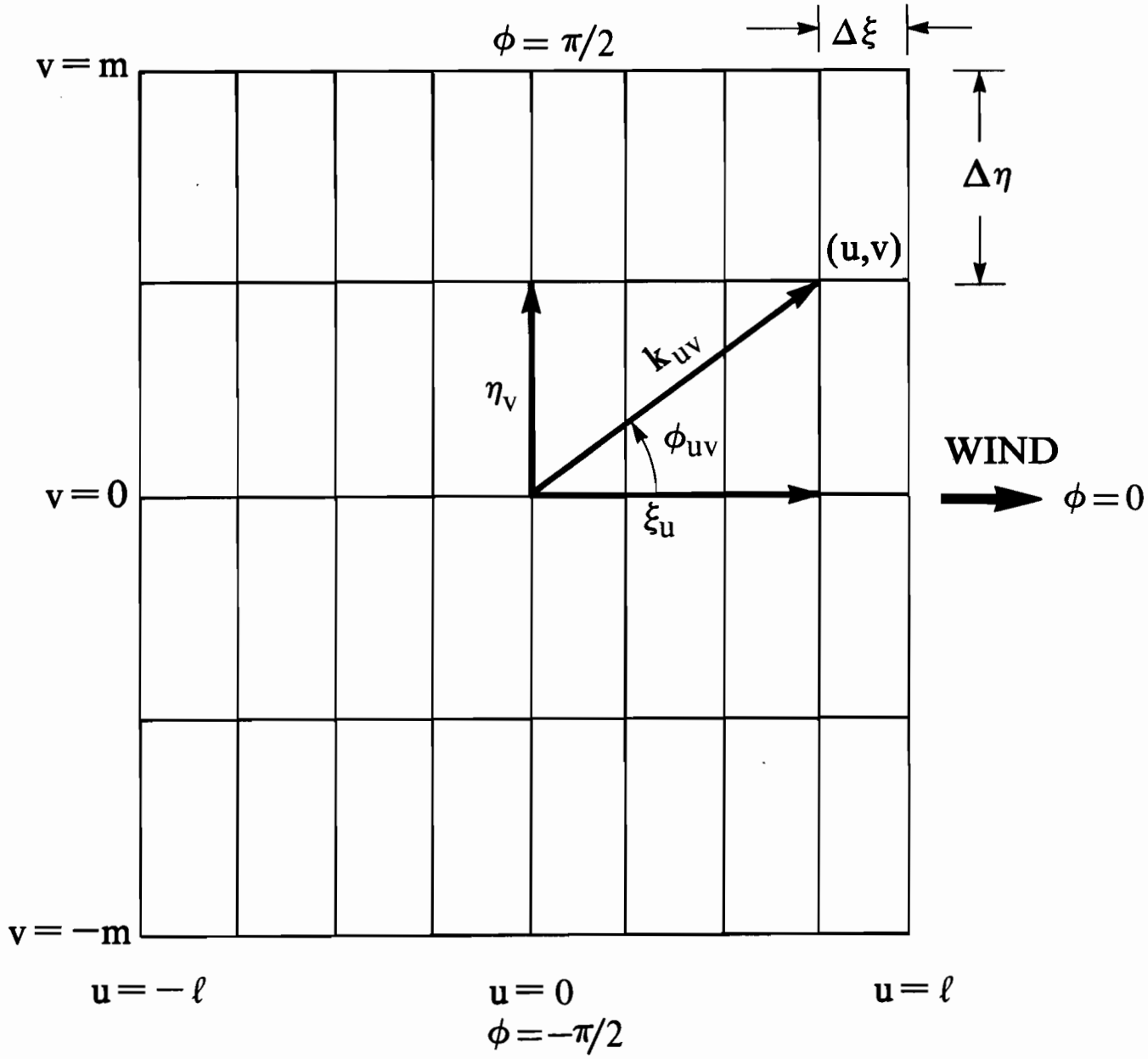

Figure 35.--The coordinate system for constructing a discrete random air-water surface. [Spectral domain for Fig. 34.]

The spectrum $E(k_u,k_v)$ has been studied in the SWOP by Pierson and colleagues, particularly in polar form $F(\sigma,\phi)$, where (*H.O.* vol. VI, p. 128, 171)*

$$E(u,v) = F(\sigma,\phi)\,\frac{g^2}{2\sigma^3} \quad , \quad \sigma^2 = gk \tag{A.5}$$

and

$$F(\sigma,\phi) = \tfrac{1}{4}\pi c_1 \sigma^{-6} \exp[-2(g/\sigma U)^2]\, f(\sigma,\phi)$$

$$f(\sigma,\phi) = \pi^{-1}\{1 + (0.50 + 0.82\xi)\cos 2\phi + (0.32\xi)\cos 4\phi\}$$

$$\xi = \exp[-\tfrac{1}{2}(\sigma U/g)^4] \quad , \quad c_1 = 3.05\ m^2\ sec^{-5}\ . \tag{A.6}$$

Here σ is temporal wave frequency, k is spatial wave number of the deep water gravity waves, and g is gravity's acceleration.

One uses (A.1) as follows. Choose the wind speed U. This fixes the frequency $\sigma_{max} = (2/3)^{\frac{1}{2}} g/U$ of highest spectral density of the wave system generated on an infinite fetch of ocean (cf. *H.O.* vol. VI, p. 187). By $\sigma^2 = gk$ and $\lambda = 2\pi/k$ this also determines the associated maximum spectral density wavelength $\lambda_{max} = 3\pi U^2/g$. We then set $X = Y = \lambda_{max}$, and resolve these waves in sufficiently fine detail by letting $\ell = m = 12$, so that $\Delta x = \Delta y = \lambda_{max}/12$. We may next determine $E(k_u,k_v)$ using (A.5) with discretely varying arguments defined by our adopted gridwork. Thus for $(u,v)\varepsilon W$, set

$$k_{uv} \equiv (k_u^2 + k_v^2)^{\frac{1}{2}} \quad , \tag{A.7}$$

where

$$k_u \equiv 2\pi \ell u/pX \quad , \quad k_v \equiv 2\pi m v/qY$$

---

* In H.O. vol. VI, p. 116, $E(k_u,k_v)$ was written as "E(u,v)" with u,v as continuous variables. Here k_u,k_v take the place of those u,v. "SWOP" stands for "Stereo Wave Observation Project."

Further, set

$$\sigma_{uv} \equiv (gk_{uv})^{\frac{1}{2}} , \tag{A.8}$$

and find

$$\phi_{uv} \equiv \arctan(k_v/k_u) .$$

Then by (A.5), for $(u,v)\varepsilon W$,

$$E(k_u,k_v) = F(\sigma_{uv},\phi_{uv}) \frac{g^2}{2\sigma_{uv}^3} , \tag{A.9}$$

in which we use the equations of (A.6) to find the numerical values of $F(\sigma_{uv},\phi_{uv})$ for each integer pair (u,v) in W. Finally, to construct the ωth realization of the random surface, for each $(u,v)\varepsilon W$ we randomly draw (for the ωth time, $\omega = 1,\ldots,r$) independent samples $b_{uv}(\omega)$ and $c_{uv}(\omega)$ from $N(0,\sigma_0^2(u,v))$ where, by (A.2)

$$\sigma_0^2(u,v) = E(k_u,k_v)\Delta u\Delta v . \tag{A.10}$$

The value of $z(x,y;\omega)$ at point (x,y) of the gridwork, for each $\omega = 1,\ldots,r$, may then be found from (A.1) by using the ωth realizations $b_{uv}(\omega)$ and $c_{uv}(\omega)$ of the random variables b_{uv} and c_{uv}. The result is $S(\omega)$, the ωth realization of the random surface $S = \{S(\omega): \omega = 1,\ldots,r\}$. In our work, we use only the circled nodes (x,y) on the hexagonal sub gridwork shown in Fig. 34. This allows a triangulation of the gravity water wave surface exactly as in the capillary case, so that we can work with plane facets of the gravity wave surface above each triad (cf. Fig. 1 and section 2B).

Initial experiments with (A.1) show that it reproduces the requirements (A.3) (the wave-elevation wind-speed law) to within a few percent over the

wind speed range $0 \leq U \leq 20$ m/sec. The theoretical value of the right side of (A.3), as a function of U, is given in *H.O.* vol. VI, pp. 187, Eq. (10). The wave-slope wind-speed law for the Neumann spectrum was also satisfied by (A.1) in preliminary trials. The theoretical form of this latter law is given in *H.O.* vol. VI, p. 188, Eq. (11).*

The form (A.1) is that of a general two-dimensional, normally distributed, spatially stationary random process; as such it is slightly more general than the form used by Pierson (1955). However, for practical purposes, Pierson's early form, by virtue of the central limit theorem, should also produce a normally distributed random surface. The present form (A.1) is not restricted to normally distributed random processes. We are free to choose the populations from which b_{uv} and c_{uv} are drawn, provided that b_{uv} and c_{uv} are independent variates and that the spectral requirements (A.2) are satisfied. This still leaves many types of random surfaces to be explored. In (A.2), $E(k_u,k_v)$ may also take other forms of spectra than the Neumann spectrum. For more recent versions of these spectra, see, e.g., Bjerkass and Riedel (1979), Pierson (1976), Pierson and Stacey (1973), Hasselmann *et al.* (1973), and Barnett and Kenyon (1976). An overview of these spectra and their various interrelations with hydrologic optics, is given in *H.O.* VI, section 12.8.

B. Capillary on Gravity Waves

Calculations of the optical properties of a fully developed sea can proceed with a minimum change of the flow diagram in Fig. 2 by simply constructing a realization of a random gravity wave surface as described in

* Change "4" in this Eq. (1) to "2". Also, change "0.8" in Eq. (12), p. 188 of this reference to "1.64".

Appendix A and then overlaying a capillary hexagonal grid on *each triangular facet* of the gravity wave surface. Thus in Fig. 34 we have a wave ordinate above each circled node of the *gravity wave* hexagonal grid. Therefore the gravity wave surface, as its capillary wave counterpart described in section 2 above, is a collection of triangular facets. Each gravity wave facet acts as the foundation for a capillary wave hexagonal grid of the kind shown in Fig. 5. Then, as described in section 7C, the capillary wave algorithm of Fig. 2 can be applied directly.

C. A Capillary-Gravity Wave Ray Tracing Model

The method to be described here for producing reflectances and transmittances of a random air water surface may be understood by referring to Fig. 36. A wind-based $\underset{\sim}{i}$-$\underset{\sim}{j}$-$\underset{\sim}{k}$ coordinate frame based at mean sea level is shown and a portion of a realized random air-water surface is drawn above the x-y plane (mean sea level). A ray proceeds from point $\underset{\sim}{p}'$ along direction $\underset{\sim}{\xi}'$. The path of the ray will intersect the air-water surface at $\underset{\sim}{p}_i$. To find this point of intersection we would compare, at various places, the relative heights of the surface and the ray path above track ABCD of the ray. The comparisons are made at intervals of λ_{min} (to be defined below). Just before $\underset{\sim}{p}_i$, at point B, the ray is above the water surface and just after, at point C, it is below. A simple linear interpolation over the segment BC of length λ_{min} would reasonably well fix the coordinates (x_i,y_i) of $\underset{\sim}{p}_i$ provided λ_{min} is sufficiently small. The height of $\underset{\sim}{p}_i$ above the plane is $z(x_i,y_i)$. At the intersection point $\underset{\sim}{p}_i$, knowledge of the surface outward normal $\underset{\sim}{n}$ allows the construction of two daughter rays along directions $\underset{\sim}{\xi}_r$ and $\underset{\sim}{\xi}_t$ for reflected and refracted flux (cf. (3.18) and (3.19)). The flux content of the two daughter rays may then be computed (as

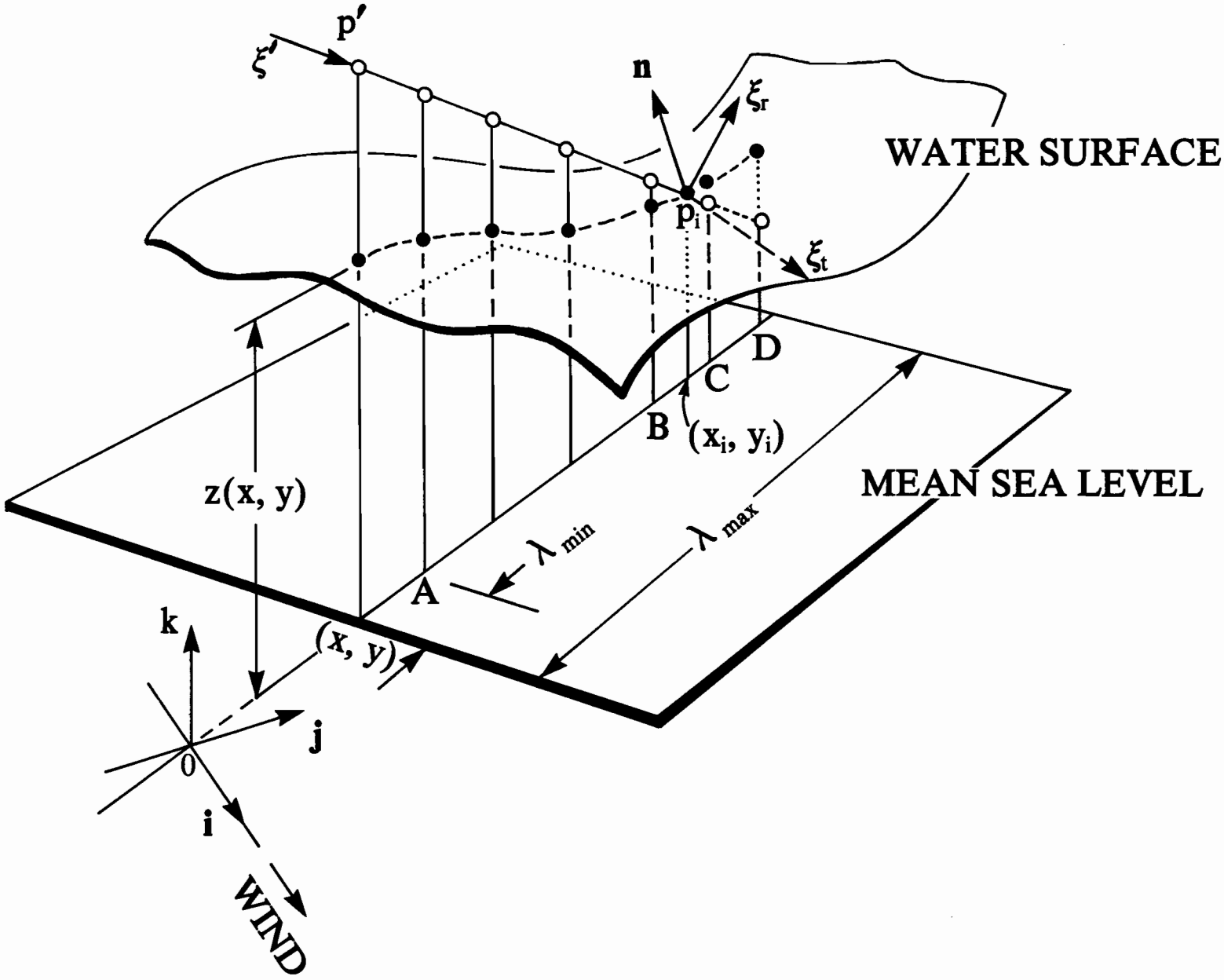

Figure 36.--Geometry for a ray $\underset{\sim}{\xi}'$ emanating from $\underset{\sim}{p}'$ intercepting a smooth (continuously differentiable) realization of a random air-water surface at point $\underset{\sim}{p}_i$ with outward unit normal $\underset{\sim}{n}$. At this point two daughter rays are formed along reflected and refracted directions $\underset{\sim}{\xi}_r$ and $\underset{\sim}{\xi}_t$.

in steps 6, 7 of Fig. 2 and using (4.4) and (4.5)). A review of the flow diagram in Fig. 2 shows that the main change needed there to handle the present model would occur in steps 2 and 5. We have just indicated how the new procedure answers the question in step 5. We next outline how the new step 2 is executed.

The continuous version of (A.1) may be used for the present purpose. However, to emphasize the wide variety of representations of $z(x,y;\omega)$ possible in the present method, we switch to the classical form of $z(x,y;\omega)$ as developed by Pierson (1955):

$$z(x,y;\omega) = 2 \sum_{(j,k)\varepsilon J} \sum A_{jk} \cos[k_j(x \cos\phi_k + y \sin\phi_k) + \varepsilon_{jk}(\omega)] \tag{C.1}$$

$$-\infty < x,y < \infty \quad , \quad \omega = 1,\ldots,r$$

Here x and y may vary continuously over the mean sea level plane; k_j and ϕ_k are polar coordinates of vector wave numbers, and

$$A_{jk} = [F(\sigma_j,\phi_k)\Delta\sigma_j\Delta\phi_k]^{\frac{1}{2}} , \tag{C.2}$$

where $\Delta\sigma_j$ and $\Delta\phi_k$ are suitable partitions of the (σ,ϕ) domain, with $0 < \sigma < \infty$ and $-\frac{1}{2}\pi \leq \phi < \frac{1}{2}\pi$. The wave spectrum $F(\sigma,\phi)$ is for example given in (A.6). The set J in (C.1) is the truncated and discrete counterpart of the (σ,ϕ) domain. The dispersion relation covering both capillary and gravity waves is

$$\sigma^2 = gk + Tk^3 \tag{C.3}$$

where

$$g = 9.8 \text{ m/s}^2 \ , \ T = 0.0728 \text{ newton/m}$$

Hence each k_j in (C.1) corresponds to a unique σ_j via (C.3). In the pure gravity wave case, the Tk^3 term may be dropped and so σ^2/g may replace k in (C.1) to obtain Pierson's form. Finally, for each $(j,k)\varepsilon J$, $e_{jk}(\omega)$ is the ωth realization of a uniformly distributed random variable ε_{jk} in $[0,2\pi]$.

The unit outward normal $\underset{\sim}{n}$ to the ωth surface realization $z(x,y;\omega)$ is given by

$$\underset{\sim}{n} = (1 + z_x^2 + z_y^2)^{-\frac{1}{2}} [-z_x \underset{\sim}{i} - z_y \underset{\sim}{j} + \underset{\sim}{k}] \tag{C.4}$$

where $z_x = z_x(x,y;\omega)$ and $z_y = z_y(x,y;\omega)$ are in turn given by

$$z_x(x,y;\omega) = -2 \sum_{(j,k)\varepsilon J} A_{jk}(k_j \cos\phi_k) \sin[k_j(x \cos\phi_k + y \sin\phi_k) + \varepsilon_{jk}(\omega)] \tag{C.5}$$

$$z_y(x,y;\omega) = -2 \sum_{(j,k)\varepsilon J} A_{jk}(k_j \sin\phi_k) \sin[k_j(x \cos\phi_k + y \sin\phi_k) + \varepsilon_{jk}(\omega)] \, . \tag{C.6}$$

The directions $\underset{\sim}{\xi}_r$ and $\underset{\sim}{\xi}_t$ of the daughter rays (in steps 6, 7 of Fig. 2) are then determined from $\underset{\sim}{\xi}'$ and $\underset{\sim}{n}$ via (3.18) or (3.19), as the case may be. The definitions for new triples in (4.4) and (4.5) apply as well here.

It remains to define λ_{min} and λ_{max} in Fig. 36. These are simply the range limits of desired geometrical detail in representing the air-water surface. A good candidate for λ_{max} is still that suggested below (A.6) in Appendix A. λ_{min} should be on the order of a few centimeters to a meter depending on the detail needed--and computer power available. Observe that each comparison of ray path height and surface height on Fig. 36 requires computation of $z(x,y;\omega)$ in (C.1). If J is a large set of indexes, one may wish to keep λ_{min} from being too small. One uses λ_{max} in a way analogous to

that suggested in Appendix A, above. Now, after proceeding a distance λ_{max} without producing an intersection, we answer the question in step 5 of Fig. 2 as "no." Observe that, aside from this distance limitation for points $\underset{\sim}{p}$ and $\underset{\sim}{p}_i$ in Fig. 36, a daughter ray (or *its* daughters) can in principle now wander arbitrarily far from the first encounter of a parent ray with the surface before the daughter ray's flux is funnelled down step 8 in Fig. 2.

10. *References*

Austin, R.W., G. Halikas, 1976. *The index of refraction of sea water.* Final Report. University of California, San Diego, Calif. SIO Ref. 76-1. Defense Adv. Res. Proj. Agency Contract No. N66857-73-C-0146, Jan. 1976.

Barnett, T.P., K.E. Kenyon, 1976. Recent advances in the study of wind waves. *Rep. Prog. Phys., 38*, 667-729.

Bjerkaas, A.W., F.W. Riedel, 1979. *Proposed Model for the Elevation Spectrum of a Wind-Roughened Sea Surface.* Report STD-R-041, Applied Physics Laboratory, Johns Hopkins Laboratory, Laurel, MD.

Cox, C., W. Munk, 1954a. The measurement of the roughness of the sea surface from photographs of the sun's glitter. *J. Opt. Soc. Am., 44*, 838-850.

Cox, C., W. Munk, 1954b. Statistics of the sea surface derived from sun glitter. *J. Mar. Res., 13*, 198-227.

Cox, C., W. Munk, 1955. Some problems in optical oceanography. *J. Mar. Res., 14*, 63-78.

Duntley, S.Q., 1950. *The Visibility of Submerged Objects*, Part 1. Optical effects of water waves. Mass. Inst. Tech. 15 Dec. 1950. Office of Naval Research contract N5ori-07831 and Bureau of Ships contract NObs-50378.

Duntley, S.Q. and R.W. Preisendorfer, 1952. *The Visibility of Submerged Objects.* Final Report. Mass. Inst. of Tech. 31 Aug. 1952. Office of Naval Research contracts N5ori-07831, N5ori-07864 and Bureau of Ships contract NObs-50378.

Duntley, S.Q., 1954. Measurements of the distribution of water wave slopes. *J. Opt. Soc. Am., 44*, 574-575.

Duntley, S.Q., 1963. Light in the sea. *J. Opt. Soc. Am., 53*, 214-233.

Eckart, C., 1946. *The sea surface and its effect on the reflection of sound and light*. File Report No. 01.75, UCDWR No. M407, Univ. of Calif. Div. of War Research at the U.S. Navy Electronics Lab., San Diego, Calif. Under Contract NO6s-2079. 20 Mar. 1946.

Guinn, J.A., G.N. Plass, G.W. Kattawar, 1979. Sunlight glitter on a wind-ruffled sea: further studies. *Appl. Optics, 18*, 842-849.

Hasselmann, K., *et al.*, 1973. *Measurements of Wind-Wave Growth and Swell Decay during the Joint North Sea Wave Project* (JONSWAP). Deutsches Hydrographisches Institut, Hamburg.

H.O. (see Preisendorfer (1976)).

Hulburt, E.O., 1934. The polarization of light at sea. *J. Opt. Soc. Am., 24*, 35-42.

Neumann, G., 1952. *On Ocean Wave Spectra and a New Method of Forecasting Wind-Generated Sea*. Beach Erosion Board, Corps of Engineers, Tech Memo 43, December 1952.

Pierson, W.J. and W. Marks, 1952. The power spectrum analysis of ocean-wave records. *Trans. Am. Geophys. Union, 33*, 834-844.

Pierson, W.J., 1955. Wind generated gravity waves, in *Advances in Geophysics, Vol. 2*, 93-178.

Pierson, W.J., and R.A. Stacey, 1973. The elevation, slope, and curvature spectra of a wind roughened sea surface. Final Report. School of Engineering and Science. N.Y. University. Univ. Heights, Bronx, N.Y. 10453.

Pierson, W.J., 1976. *The Theory and Applications of Ocean Wave Measuring Systems At and Below the Sea Surface, on the Land, from Aircraft, and Space Craft*. Report NASA, CR-2646, University Institute of Oceanography, City University of New York, New York, N.Y. National Aeronautics and Space Administration Contract NAS 5-20041. January 1976, 400 pp.

Preisendorfer, R.W., 1965. *Radiative Transfer on Discrete Spaces*. Pergamon Press, N.Y.

Preisendorfer, R.W., 1971. General theory of radiative transfer across the random atmosphere-ocean interface. *J. Quant. Spectrosc. Radiat. Transfer, 11*, 723-737.

Preisendorfer, R.W., 1976. *Hydrologic Optics*. Pacific Marine Environmental Laboratory, ERL/NOAA, Seattle, WA 98115 [A six volume set: Vol. I, Introduction, PB-259793/8ST; Vol. II, Foundations, PB-259794/6ST; Vol. III, Solutions, PB-259795/3ST; Vol. IV, Imbeddings, PB-259796/1ST; Vol. V, Properties, PB-259797/9ST; Vol. VI, Surfaces, PB-268704/4ST. Available from National Technical Information Service, U.S. Dept. of Commerce, 5285 Port Royal Road, Springfield, VA 22161].

Preisendorfer, R.W. and C.D. Mobley, 1984. Direct and inverse irradiance models in hydrologic optics. *Limnol. Oceanogr., 29*, 903-929.

Schooley, A.H., 1954. A simple optical method of measuring the statistical distribution of water surface slopes. *J. Opt. Soc. Am., 44*, 37-40.

Shuleikin, V.V., 1968. Fizika Moria (Physics of the Sea). Izd. Akad. Nauk S.S.S.R., Moscow. (4th Ed. Revised and Expanded).

Stratton, J.A., 1941. *Electromagnetic Theory*. McGraw-Hill, N.Y.